Doctoral Dissertation

Studies on Optical Signal Multiplexing using Fractional Fourier Transform and All-Optical Analog-to-Digital Conversion

Tomotaka NAGASHIMA

January 2017

Graduate School of Engineering,
Osaka University, JAPAN

Studies on Optical Signal Multiplexing using Fractional Fourier Transform and All-Optical Analog-to-Digital Conversion

（フラクショナルフーリエ変換と全光アナログデジタル変換を用いた光信号多重化に関する研究）

Tomotaka NAGASHIMA

Dedicated to my family

Contents

General introduction

Optical signal multiplexing plays an important role in many systems for communication. For example, in optical communication, large capacity information transmission is realized by multiplexing different wavelength lights to overcome the limitation due to processing speed of electrical circuits and optical modulators. Furthermore, measurement systems such as spectroscopy are also regarded as a kind of communication system because physical and chemical properties of objects are obtained by demultiplexing contained informations in the measured spectrum. In such a communication system, multiplexing and demultiplexing certainly affect a system transfer function.

To get the best performance of the system, it is important to optimize its transfer function how the signals are transmitted and received through a system. Among such a communication system, an optical communication system is useful as a representative model for optimization because it would be the most feasible and reliable one in a real world. In recent years, to satisfy the requirement of an enormous increase of a transmission capacity among limited optical spectral resources,[1] advanced signal processing such as orthogonal frequency division multiplexing (OFDM) based on Fourier transform and multilevel modulation with high speed digital-to-analog conversion / analog-to-digital conversion (ADC) is enthusiastically introduced.[2–21] However, a high launch power to an optical fiber with an increase in transmission capacity leads to nonlinear effect which degrades a signal quality, thus the further capacity increase requires an optimization of the transmission system to avoid a signal degradation.[22–39]

To optimize a system transfer function, multiplexing techniques should be flexibly selected in accordance with the system. Recently, it is predicted that optical OFDM based on fractional Fourier transform (FrFT) in place of Fourier transform increases the system flexibility.[40] Although the optical fractional OFDM is expected to suppress signal impairments in the propagation, the behavior of a transmission signal in actual optical fiber links still hasn't been verified. If the signal degradation is miti-

gated, a multilevel modulation with high multiplicity is available. To treat the high multiplicity of multilevel modulation, the high resolution ADC is required.[41] However, performance of conventional electrical ADCs are limited by the jitter of the sampling aperture and the power consumption.[42] To overcome this limitation, optical approaches have recently attracted much attention because a mode locked laser, which provides an ultra-stable optical pulse stream, can offer a sampling aperture with ultra-low jitter, as low as a few femtoseconds.[43–49] Although optical sampling using optical pulse streams with electrical quantization and coding processes realizes high-performance ADCs, multiple electrical ADCs are required to support a high sampling rate, and therefore, increased energy consumption is unavoidable.[50–53] Using optical technology for the entire process, including the subsequent quantization and coding, should reduce energy consumption.[54–66]

To get the best performance of a transmission system by optimizing its transfer function, it is important to clarify the behavior of a transmission signal in actual optical fiber links. Additionally, a feasibility demonstration of devices and subsystems such as implementation of FrFT and ADC in various environments is of considerable practical significance.

In this thesis, to realize the optimized signal processing for the limiting factor of large capacity communications, optical signal multiplexing using FrFT and all-optical ADC is presented. This thesis consists of general introduction, six chapters, and summary. Contents of chapters in the thesis are listed with brief summaries in the followings.

In Chapter 1, introduction of optical signal multiplexing in optical communication is presented as an essential procedure. At the beginning, overviews of current situation in optical signal multiplexing for large capacity optical communications is described. To understand the necessity of optimization of a transfer function in optical transmission system, various phenomena induced in optical fibers during transmission are explained.

The frequency domain is not always optimum for all of applications, although it is used for powerful signal processing based on the Fourier transform. FrFT is expected to generalize the Fourier transform, and define a new domain which could provide more flexible signal processing. In Chapter 2, an innovative optical OFDM based on FrFT in place of the conventional Fourier transform is presented. The theoretical backgrounds of FrFT and the method of all-optical implementation of an optical signal are described.

The behavior of optical fractional OFDM signal in a dispersive fiber focusing on the reduction of peak to average power ratio is clarified. Moreover, the fiber nonlinearity mitigation technique is proposed and demonstrated by evaluating the transmission performance of the fractional OFDM signal in the dispersion compensated fiber link in simulation.

In Chapter 3, to confirm that the FrFT can generalize the Fourier transform with keeping original useful functions in the Fourier transform, a verification of cyclic prefix insertion for all-optical fractional OFDM is presented. Since cyclic prefix exploits a periodicity of the discrete Fourier transform to reduce linear impairments such as chromatic dispersion in conventional OFDM, it is expected that a cyclic prefix is also effective for a fractional OFDM signal. The cyclic prefix insertion for all-optical fractional OFDM is experimentally demonstrated. The relationship between a fractional parameter and an effect of cyclic prefix insertion is investigated in simulation.

In Chapter 2 and 3, a performance maximization of a transmission system by optimizing an optical signal multiplexing by FrFT was describes. In order to apply optimized transmission system in an actual system, it is indispensable to demonstrate the feasibility of devices and subsystems of the system. In Chapter 4, experimental demonstrations of feasibilities of implementation of all-optical fractional OFDM for practical use are presented. Firstly, to guarantee the operation in an actual network, the field trial in JGN-X which is an optical network testbed laid between NICT (at Koganei) and KDDI (at Ohtemachi) is demonstrated. Secondly, to reduce the cost of introducing the system, the feasibility of a cost effective all-optical fractional OFDM receiver using a planar lightwave circuit is demonstrated. Thirdly, to extend a flexibility of the signal handling method, a demultiplexing of an optical fractional OFDM signal by a time-lens effect is demonstrated.

In Chapter 5, the necessity and issue on all-optical ADC are experimentally examined to cope with an optical fractional OFDM. Firstly, the motivation of an optical approach for ADC and principle of all-optical ADC are stated. To demonstrate the feasibility of all-optical ADC for a received optical fractional OFDM signal, the experimental demonstration of a demodulation of 4-amplitude-shift keying optical fractional OFDM signal using 2 bit all-optical ADC is presented.

Lastly, in Chapter 6, resolution improvement techniques of all-optical ADC are proposed to treat the received signal with higher performance in practical limitations.

Firstly, to cope with a imperfection of components in the all-optical ADC, a quantization error improvement technique is presented and experimentally demonstrated. Secondly, to overcome a limitation of a trade off between sampling rate and resolution, the sampling rate independent resolution upgrade is presented. Finally, the demonstration of 40 GS/s 4 bit all-optical ADC is presented.

Chapter 1

Introduction of optical signal multiplexing

In this chapter, introduction of optical signal multiplexing in optical communication is presented as an essential procedure. At the beginning, overviews of current situation in optical signal multiplexing for large capacity optical communications is described. To understand the necessity of optimization of a transfer function in optical transmission system, various phenomena induced in optical fibers during transmission are explained.

1.1 Signal multiplexing in optical fiber communication

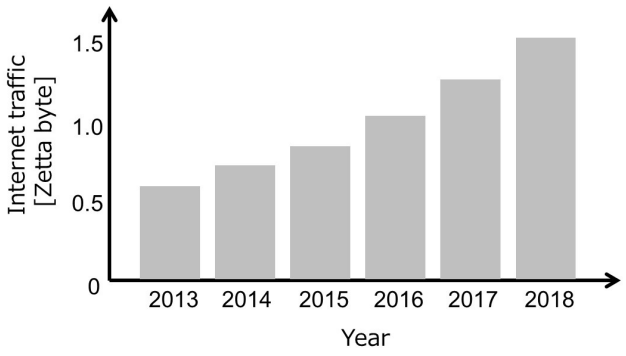

Figure 1.1: Global Internet traffic.

The popularization of network environments such as the Internet spurred the rapid growth and spread of social networking service, video streaming contents, videoconferencing, cloud computing, and on-line shopping and greatly transformed the lives of citizens and the shape of industries. In 2016, global Internet traffic is expected

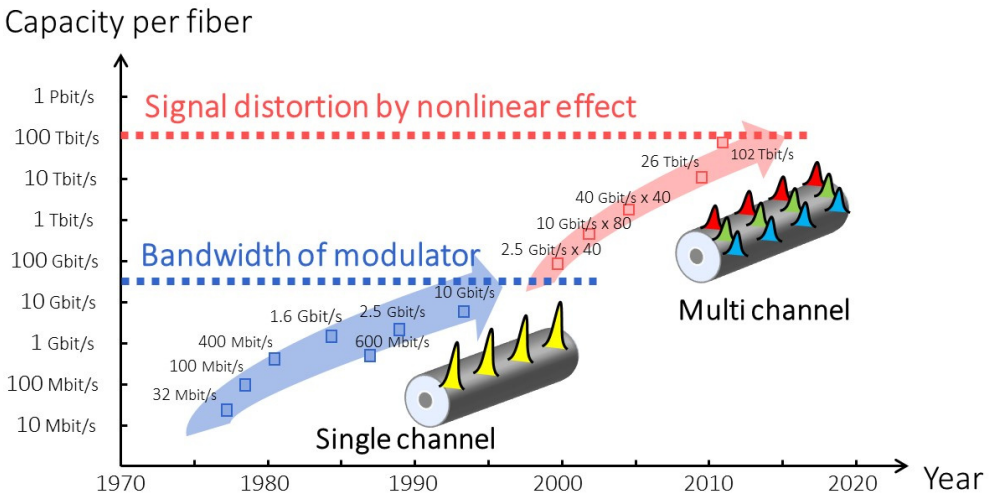

Figure 1.2: Capacity of fiber.

to exceed 1 zetta-byte (zetta = 10^{21}), as shown in Fig. 1.1. The compound annual growth rate of Internet traffic is 21 percent in the period 2013-2018.[1] The Internet traffic in 2040 is expected to grow by 100 times because of the spread of smart phone and tablet devises, ultra high definition (4K or 8K) video contents, and Internet of things technologies. Optical fiber communication is a fascinating technology to satisfy the tremendous demand of the transmission capacity. One of the advantages of optical fiber is the low-loss characteristic. Although the glass made by the ancient Egyptian in 1 BC was transparent in the region of visible wavelength, general glasses used of windows have typically a loss of a few dB/mm. Thus, waveguides using free space optical beam and lenses were considered at an early stage of the development of the optical communication. However, it has a weak point that components of free space optics are weak against vibration and environmental fluctuation. Since Kao and Hockham (1966) predicted that the fiber loss could be reduced to as low as 20 dB/km by lowering the impurity concentration of glass,[67] the development of low loss optical fiber was immediately accelerated. Today's commercially available optical fiber has a loss of about 0.2 dB/km at the low-loss window around 1550 nm. Another advantage of the optical fiber is the wide band property. The coaxial cable which is used for traditional telecommunications attenuates the high frequency components of the transmission signal and limits the transmission speed. On the other hand, the available bandwidth of the optical fiber is very broad than the coaxial cable. Figure 1.2 shows the evolution of the transmission capacity of the optical fiber. Optical signal multiplexing, which allows

a number of channels to be established in an optical fiber is a key technology. Optical amplifier such as Erbium doped fiber amplifier (EDFA) realized wavelength division multiplexing (WDM), which bundles wavelength different subcarriers. A record capacity of 100 Tbit/s for single core transmission[68,69] used digital coherent technique and multilevel multiplexing which transmits several data in one symbol for high spectral efficiency coding. In order to further the capacity expansion, countermeasures for nonlinear signal distortion is required. Recently, to overcome this issue of nonlinear signal distortion, spatial division multiplexing based on multi core and multi mode fiber is developing. For the maximization of the capacity of whole fiber, the capacity expansion per core is important. Additionally, there is strong motivation from a business perspective to reduce implementation costs by exploiting the capacity of the existing installed optical fibers without the costly deployment of new fibers.

1.2 Conventional optical signal multiplexing technique

1.2.1 Wavelength division multiplexing

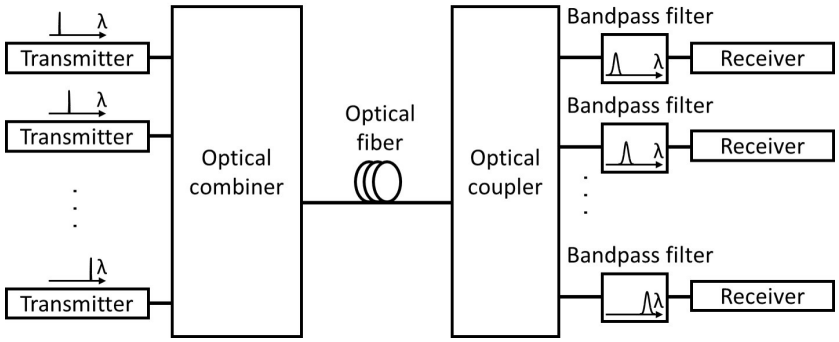

Figure 1.3: Wavelength division multiplexing.

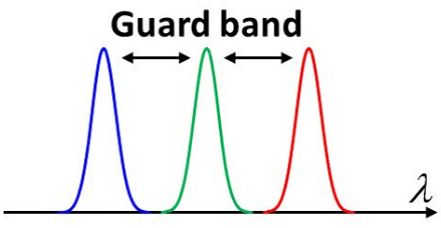

Figure 1.4: Spectrum of WDM signal.

The symbol rate per channel is limited to several ten Gbaud/s due to processing speed of electrical circuit and optical modulator. In WDM, data of each channel is converted to different wavelength subcarrier and multiplexed using a optical combiner at the transmitter, as shown in Fig. 1.3. At the receiver side, the transmitted signal is demultiplexed using a optical coupler and a bandpass filter into separate subcarriers and converted into electrical signals. The transmission capacity could be increased depending on the number of channels. However, longhaul transmissions required a demultiplexing, a large number of signal regenerations, and a multiplexing in every repeater before the development of optical amplifiers. The optical amplifier covers a wide range of optical band and simultaneously amplifies a lot of subcarriers. EDFA is a typical optical amplifier and amplifies several ten nm of wavelength range. The number of available subcarriers is depending on the cover range of optical amplifier. Thus, wideband optical amplifiers is effective for the capacity expansion. Recent ultra-wadeband amplification can cover the wavelength range over 100 nm.[70] For effective utilization of optical spectral resources, the wavelength interval of each subcarrier should be narrow as soon as possible. However, spectral guard bands are required to avoid crosstalk from adjacent channels, as shown in Fig. 1.4.

1.2.2 Orthogonal frequency division multiplexing

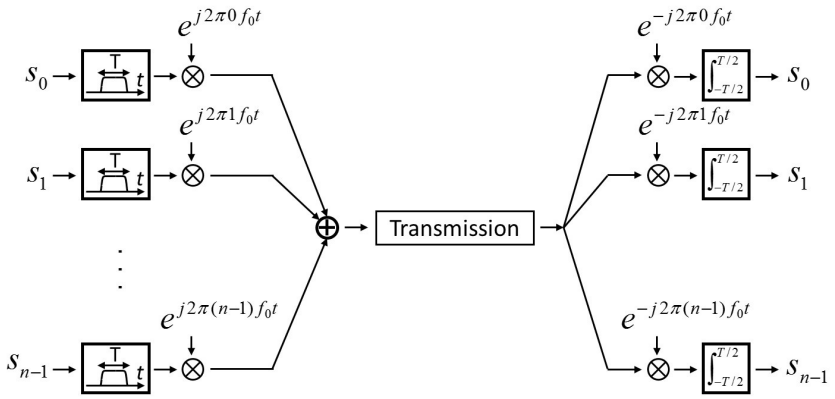

Figure 1.5: Conceptual diagram of OFDM.

Orthogonal frequency division multiplexing (OFDM) is a more recent approach in optical communication.[2] OFDM is well known in wireless telecommunication. In contrast to WDM, OFDM subcarriers overlap each other significantly. Nevertheless, each OFDM subcarrier could be demultiplexed without the interference from other

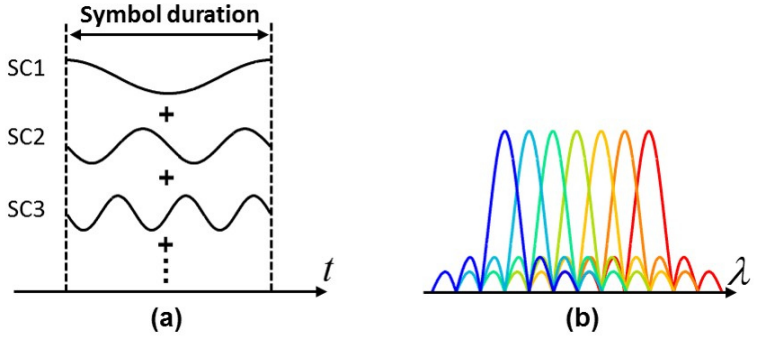

Figure 1.6: (a) Waveform of OFDM signal. (b) Spectrum of OFDM signal.

channels by exploiting the orthogonality between the individual subcarriers. Figure 1.5 shows the conceptual diagram of OFDM. The OFDM subcarrier is described by

$$\phi_n^1(t) = rect\left(\frac{t}{T}\right) \cdot e^{j2\pi n f_0 t}, \tag{1.1}$$

where n is an integer, $T = 1/f_0$ is symbol duration, and f_0 is interval of each subcarrier frequency. Here, eq. (1.1) is represented one symbol. Exactly n cycles of sin wave are included in the symbol duration T, as shown in Fig. 1.6(a). The amplitude and phase are changed depending on the value of the data symbol s_n. The multiplexed signal of N subcarriers is described

$$x(t) = \sum_{n=0}^{N-1} s_n \phi_n^1(t), \tag{1.2}$$

where s_n is a data symbol. The spectrum of each subcarrier is sinc shape, as shown in Fig. 1.6(b). The optimum detector for each subcarrier could use a correlator that matches the subcarrier waveform. Thus, the detected information symbol d_m at the output of the correlator is given by

$$d_m = \frac{1}{T}\int_{-T/2}^{T/2} x(t)\phi_n^{1*}(t)dt = \frac{1}{T}\int_{-T/2}^{T/2} x(t)e^{-j2\pi m f_0 t}dt. \tag{1.3}$$

Here, the two subcarriers are orthogonal to each other as following equation

$$\int_{-T/2}^{T/2} e^{j2\pi n f_0 t} e^{-j2\pi m f_0 t}dt = \begin{cases} T & (m = n) \\ 0 & (m \neq n). \end{cases} \tag{1.4}$$

Therefore,

$$d_m = \begin{cases} s_n & (m = n) \\ 0 & (m \neq n). \end{cases} \tag{1.5}$$

These orthogonal subcarrier sets, with their frequencies spaced at a multiple of the inverse of the symbol duration can be recovered with the matched filters without inter carrier interference (ICI), in spite of strong signal spectral overlapping.

If the OFDM signal is sampled with a sample duration of $1/Nf_0$, and add a normalization factor 1/N

$$\begin{aligned} x(\frac{k}{Nf_0}) &= \frac{1}{N}\sum_{n=0}^{N-1} s_n e^{j2\pi n f_0 \frac{k}{Nf_0}} \\ &= \sum_{n=0}^{N-1} s_n e^{j\frac{2\pi kn}{N}} (k = 0, 1, 2, ..., N-1). \end{aligned} \tag{1.6}$$

This is exactly the expression of inverse discrete Fourier transform (IDFT). It means that the OFDM baseband signal can be implemented by IDFT. The pre-coded signals are in the frequency domain, and output of the IDFT is in the time domain. Similarly, at the receiver side, the data is recovered by discrete Fourier transform (DFT),

$$s_n = \sum_{k=0}^{N-1} x(\frac{k}{Nf_0}) e^{-j\frac{2\pi kn}{N}} (k = 0, 1, 2, ..., N-1). \tag{1.7}$$

A large number of orthogonal subcarriers can be modulated and demodulated without resorting to a very complex array of oscillators and filters. Since IDFT/DFT could be implemented by fast Fourier transform (FFT) algorithm, OFDM system is realized by a relatively simple architecture. In optical communication, optical OFDM technique has been widely investigated for high spectral efficiency transmission with high speed electronic processing devices.[3–9] However, the maximum transmission capacity is limited by the speed and the power consumption of the electronic processing devices. Recently, all-optical implementations of IDFT/DFT operation for all-optical OFDM have been proposed using passive optical components such as optical delay lines and phase shifters, Mach Zehnder delay interferometers, fiber Bragg grating, an arrayed waveguide grating, and planar lightwave circuit.[10–16] All-optical OFDM can avoid electrical speed limitation and reduce energy consumption and system costs because passive optical components are transparent for modulation format and speed and don't require additional energy consumption.

Fig. 1.7(a) shows the principle of all-optical IDFT operation with optical delay lines and phase shifters for an N subcarrier conventional OFDM. The nth subcarrier

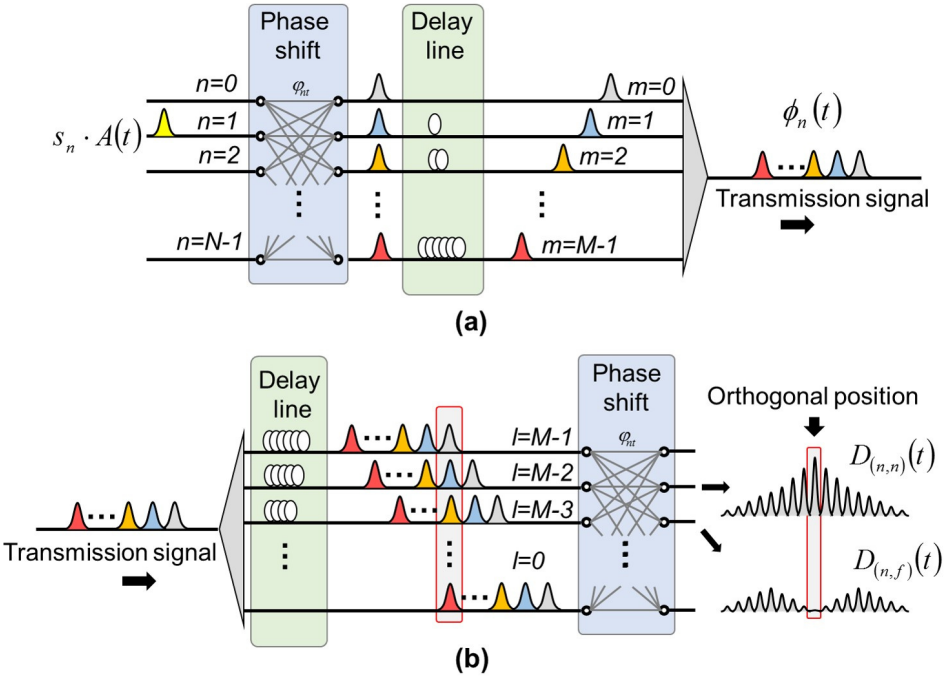

Figure 1.7: All-optical implementation of IDFT/DFT.

is expressed by

$$\phi_n^1(t) = \sum_{m=0}^{M-1} s_n \cdot A(t + m \cdot \tau) exp\left(j2\pi n \frac{m}{M}\right), \tag{1.8}$$

where s_n is the complex data with high-order modulation, $A(t)$ is the shape of an optical pulse, M is the number of IDFT samples within the symbol duration T, and $\tau = T/M$ is the delay time between each sample.

The all-optical DFT operation for demultiplexing is similar to the IDFT operation, as shown in Fig. 1.7(b). The output signal of the corresponding nth DFT operation is expressed by

$$\begin{aligned} D_{(n,n)}^1(t) &= \sum_{l=0}^{M-1} \phi_n^1(t) exp\left(j2\pi n \frac{l}{M}\right) \\ &= \sum_{l=0}^{M-1} \sum_{m=0}^{M-1} s_n \cdot A(t + (m+l) \cdot \tau) exp\left(j2\pi n \frac{m+l}{M}\right). \end{aligned} \tag{1.9}$$

The number of samples of the output signal is $2M - 1$. Because all-optical DFT is operated by linear convolution, the orthogonal condition can be satisfied for only one sample in the symbol duration. At the position $m + l = M - 1$, which is equal to

$t_s = (M-1)\tau$, the signal is expressed by

$$D^1_{(n,n,t_n)}(t) = M \cdot s_n \cdot A(t) \cdot exp\left(j2\pi n \frac{M-1}{M}\right). \tag{1.10}$$

On the other hand, the output signal of the non-corresponding fth DFT operation is expressed by

$$\begin{aligned} D^1_{(n,f)}(t) &= \sum_{l=0}^{M-1} \phi^1_n(t) exp\left(j2\pi f \frac{l}{M}\right) \\ &= \sum_{l=0}^{M-1}\sum_{m=0}^{M-1} s_n \cdot A(t+(m+l)\cdot\tau) exp\left(j2\pi n \frac{nm+fl}{M}\right). \end{aligned} \tag{1.11}$$

At $t_s = (M-1)\tau$, the signal is expressed by

$$\begin{aligned} D^1_{(n,f,t_s)}(t) &= s_n \cdot A(t) \cdot \sum_{m=0}^{M-1} exp\left(\frac{j2\pi}{M}(m(n-f)+(M-1)f)\right) \\ &= s_n \cdot A(t) \cdot exp\left(\frac{j2\pi}{M}(M-1)f\right) \sum_{m=0}^{M-1} exp\left(\frac{j2\pi}{M}m(n-f)\right) \\ &= s_n \cdot A(t) \cdot exp\left(\frac{j2\pi}{M}(M-1)f\right) \frac{1-exp\left(\frac{j2\pi}{M}M(n-f)\right)}{1-exp\left(\frac{j2\pi}{M}(n-f)\right)} \\ &= 0. \end{aligned} \tag{1.12}$$

The energy of different subcarriers can disappear, at which point the energy of the target subcarrier becomes maximum. Because the subcarriers are extracted from the transmission signal without the ICI at only the orthogonal position, the time gate is used to reduce the interference of the non-orthogonal position.

All-optical IDFT/DFT could be also implemented by time-space conversion based optical spectral shaping technique such as wavelength selective switch (WSS)[17,18] because all-optical IDFT/DFT circuit is a special optical filter. Figure 1.8 shows a schematic diagram of time-space conversion based spectral shaping. An input signal $h(t)$ is input on the diffraction grating 1 at an angle. The temporal waveform of the input signal is spatially projected onto the plane of grating 1. The spatial distribution of the input signal along the horizontal axis x_0 is represented by $h(t; x_0)$. The input signal is divided into decomposed spectral waves by the diffraction grating 1. Those decomposed spectral waves are collimated by the cylindrical lens 1, and respectively distributed at different positions of the horizontal axis x_1. The spatial distribution of

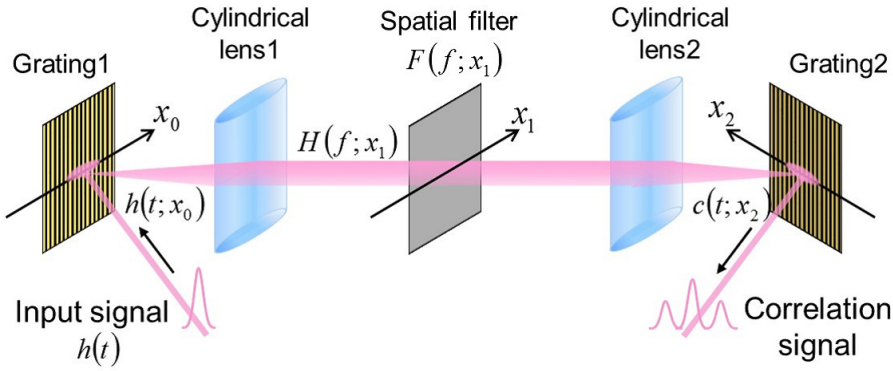

Figure 1.8: Schematic diagram of time-space conversion based spectral shaping.

the spectrum is adopted as a spatial signal. This spatial signal $H(f;x_1)$ is given by the Fourier transform of the input signal $h(t;x_0)$, which is described as

$$H(f;x_1) = \int_{-\infty}^{+\infty} h(t;x_0) exp(-j2\pi ft)dt. \tag{1.13}$$

Thus, the spatial signal $H(f;x_1)$ corresponding to the input signal $h(t)$ can be obtained. By setting a spatial filter, optical spectral shaping is accomplished in the spatial domain. If a spatial filter $F(f;x_1)$ is applied to the spatial signal $H(f;x_1)$, the product of $H(f;x_1)$ and $F(f;x_1)$ can be implemented in the spatial domain. And then, the product is converted into the output signal $c(t;x_2)$ by the inverse time-space conversion with cylindrical lens 2 and the diffraction grating 2. The output signal $c(t;x_2)$ is given by

$$c(t;x_2) = \frac{1}{2\pi}\int_{-\infty}^{+\infty} H(f;x_1)\cdot F(f;x_1) exp(j2\pi ft)df, \tag{1.14}$$

where the filter function $F(f)$ is the inverse Fourier transform of $f(t)$,

$$F(f) = \int_{-\infty}^{+\infty} f(t) exp(-j2\pi ft)df. \tag{1.15}$$

The spatial filter is reconfigurable by using spatial light modulators such as liquid crystal on silicon. The filter function of OFDM subcarrier is obtained by Fourier transform of eq. (1.1),

$$\begin{aligned} F_n(f) &= \int_{-\infty}^{+\infty} \phi_n^1(t) exp(-j2\pi ft)df \\ &= \int_{-\infty}^{+\infty} rect\left(\frac{t}{T}\right) e^{j2\pi nf_0 t} exp(-j2\pi ft)df \\ &= \frac{1}{f_0} sinc\left(\frac{f}{f_0}\right) \otimes \delta(f - nf_0). \end{aligned} \tag{1.16}$$

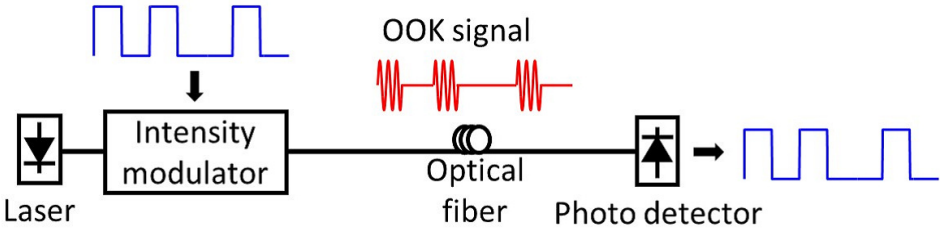

Figure 1.9: Schematic diagram of OOK transmission.

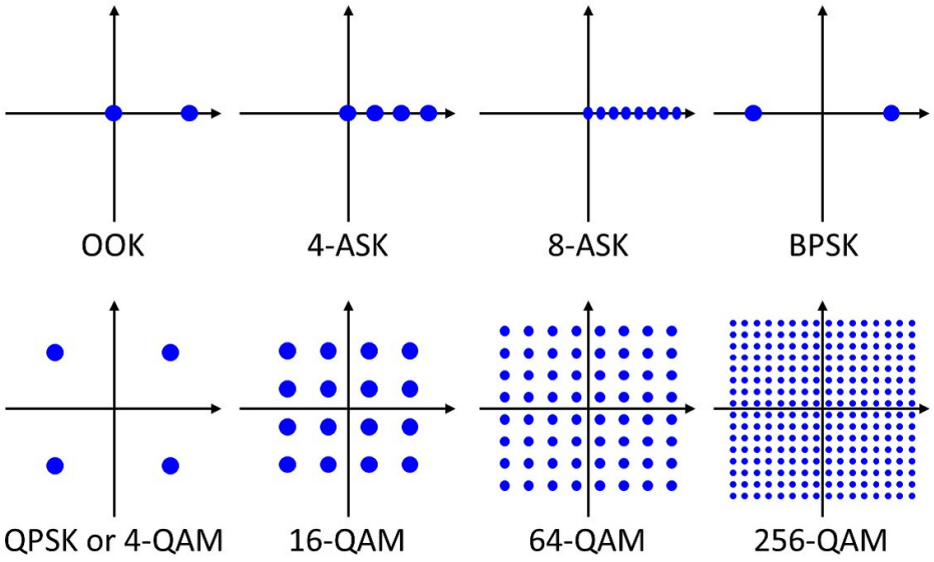

Figure 1.10: Constellation of OOK, ASK, PSK, and QAM.

1.3 Multilevel modulation

The optical carrier is modulated to map the information data onto its amplitude, phase, or a combination of amplitude and phase.[19–21] Figure 1.9 shows the diagram of on-off-keying (OOK) transmission. In OOK, a pulse represents data '1', and no pulse is transmitted for data '0'. The modulation format most commonly used in optical fiber communication has been OOK because the OOK signal could be detected only a simple photo detector. Although OFDM minimizes the subcarrier interval in frequency domain and realizes the high-density multiplexing, when the one symbol carries one binary data using OOK, the spectral efficiency is limited to 1 bit/s/Hz. Note that this discussion considers only single polarization. The signal multiplexing by multilevel modulation formats is a solution to increasing the spectral efficiency. Figure 1.10 shows the signal constellation of OOK, amplitude-shift-keying (ASK), phase-shift-keying (PSK), and quadrature-amplitude modulation (QAM) signal. Although the optical carrier has

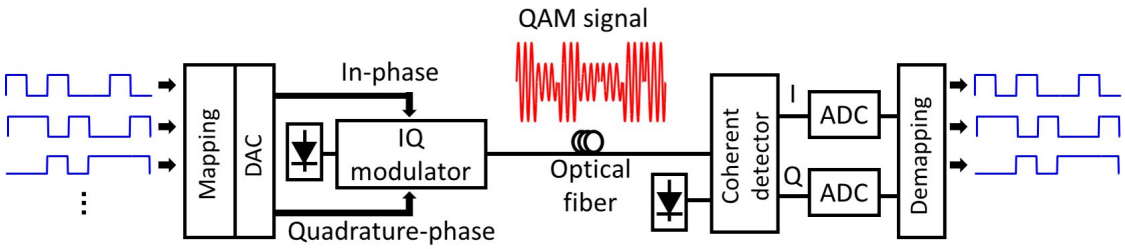

Figure 1.11: Schematic diagram of QAM transmission.

both in- and quadrature-phase that was represented as a two-dimensional constellation, OOK and ASK uses only the positive axis of a signal dimension to carry information. QAM scheme uses positive and negative sides of both dimensions. The modulation formats with M level can achieve up to the spectral efficiency of $log_2 M$ bit/s/Hz. Figure 1.11 shows the diagram of QAM transmission. The multilevel signal, whose number of level is $M = 2^N$, is generated by multiplexing N binary signals. After mapping in the constellation, the multilevel signal modulates the optical carrier through digital-to-analog conversion. At the receiver, the coherent detection is used to obtain the electrical field of the optical signal including amplitude and phase. The received multilevel signal is demapped to N binary signals after analog-to-digital conversion (ADC).

While higher order multilevel modulations realize high spectral efficiency, Euclidean distances between the adjacent level in the constellation diagram are shorter. When the noise is large, the possibility of an erroneous signal decision is enhanced. In transmission link, the noises occur due to various factors such as amplified spontaneous emission (ASE) in optical amplifiers, chromatic dispersion, and nonlinear effect in optical fibers. Therefore the improvement of the spectral efficiency is depending on the distance and characteristic of the transmission link.

1.4 Propagation in optical fiber

1.4.1 Loss

An optical fiber has a power loss during transmission of optical signals due to material absorption and Rayleigh scattering. If P_0 is the power launched at the input of a fiber of length L, the transmitted power P_T is given by

$$P_T = P_0 exp(-\alpha L), \tag{1.17}$$

where the attenuation constant α is the measure of the fiber loss. Modern fibers exhibit a loss of 0.2 dB/km near 1550 nm.[71] In a long-haul transmission, the optical amplifier such as EDFA is used to compensate the fiber loss. Typically, the optical signal is amplified every 80-100 km in long-haul transmission systems. Each time the signal passes through the optical amplifier, the amplifier noise is accumulated, resulting in signal to noise ratio (SNR) degradation.

1.4.2 Chromatic dispersion

When an electromagnetic wave interacts with the bound electrons of a dielectric, the induced dielectric polarization $P(t)$ is related to an electric field $E(t)$.

$$P(t) = \varepsilon_0 \chi^{(1)} E(t), \tag{1.18}$$

where ε_0 and $\chi^{(1)}$ are the electric permittivity of free space and the electric susceptibility, respectively. If the intensity of electrical field is not strong, the relationship is linear. The frequency of the vibration of P is the same as the E. While a new electro magnetic wave is emitted by the vibration of P, the phase of the new wave is delayed. As a result, the propagation velocity in the medium is slower than in vacuum.

$$v(\omega) = \frac{c}{n(\omega)}. \tag{1.19}$$

The refractive index $n(\omega)$ is related to the electric susceptibility $\chi^{(1)}$ by a relation

$$n(\omega)^2 = 1 + \tilde{\chi}^{(1)}(\omega), \tag{1.20}$$

where $\tilde{\chi}^{(1)}(\omega)$ is the Fourier transform of $\chi^{(1)}(t)$. the electric susceptibility depends on the optical frequency ω due to the characteristic resonance frequencies of the medium. Therefore the frequency dependence of the refractive index induces chromatic dispersion. Fiber dispersion plays a critical role in propagation of the optical signal because different spectral components of the optical signal travel at different speeds and the waveform of the optical signal is changed. The effects of chromatic dispersion are accounted for by expanding the mode propagation constant β in a Taylor series about the center frequency ω_0

$$\begin{aligned} \beta(\omega) &= n(\omega)\frac{\omega}{c}, \\ &= \beta_0 + \beta_1(\omega - \omega_0) + \beta_2(\omega - \omega_0)^2 + \beta_3(\omega - \omega_0)^3, \qquad (1.21) \\ \beta_{[}m] &= [\frac{d^m \beta}{d\omega^m}]_{\omega=\omega_o}. \qquad (1.22) \end{aligned}$$

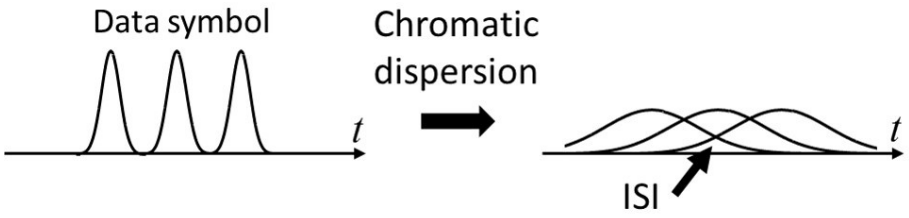

Figure 1.12: ISI induced by chromatic dispersion.

The parameters β_1 and β_2 are related to the refractive index $n(\omega)$ and its derivatives through the relations

$$\beta_1 = \frac{1}{c}[n + \omega\frac{dn}{d\omega}] = \frac{n_g}{c} = \frac{1}{\nu_g}, \tag{1.23}$$

$$\beta_2 = \frac{1}{c}[2\omega\frac{d^2n}{d\omega^2} + \omega\frac{d^2n}{d\omega^2}] \simeq \frac{\omega}{c}\frac{d^2n}{d\omega^2} \simeq \frac{\lambda^3}{2\pi c^2}\frac{d^2n}{d\lambda^2}, \tag{1.24}$$

where n_g and v_g are the group index and the group velocity. The envelope of an optical signal moves at the group velocity, while the parameter β_2 represents dispersion of the group velocity and is responsible for the change of the waveform. When the spectrum of the input optical signal is broad, the inclusion of higher order dispersion effects is necessary. For wavelengths such that $\beta_2 > 0$, the fiber is said to exhibit normal dispersion. In the normal dispersion regime, high frequency components of the optical signal travel slower than low frequency components. On the other hand, the opposite occurs in the anomalous dispersion regime in which $\beta_2 < 0$. The dispersion parameter D is also used in practice. In is related to β_2 and λ

$$D = -\frac{2\pi c}{\lambda^2}\beta_2. \tag{1.25}$$

For example, the chromatic dispersion of the standard single mode fiber (SMF) at 1550 nm is $D = 17$ ps/nm/km.[35,72,73] The waveform change of the transmission signal by the chromatic dispersion induces inter symbol interference (ISI) and degraded the signal quality, as shown in Fig. 1.12.

1.4.3 Nonlinear effect

When the intensity of electrical field is strong, the relationship between the induced dielectric polarization $P(t)$ and an electric field $E(t)$ becomes nonlinear.[71,74] Since the frequency of the vibration of P is different to the E, the different frequency lights are

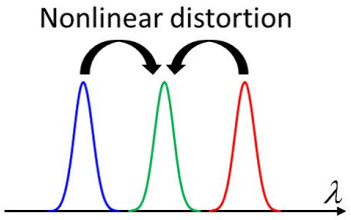

Figure 1.13: ICI induced by nonlinear effect.

emitted.

$$P(t) = \varepsilon_0(\chi^{(1)}E(t) + \chi^{(2)}E^2(t) + \chi^{(3)}E^3(t) + \cdots), \tag{1.26}$$

where $\chi^{(j)}$ is jth order susceptibility. The susceptibility varies depending on the medium. As SiO_2 is a symmetric molecule, the second order susceptibility $\chi^{(2)}$ vanishes for silica glasses. Thus the lowest order nonlinear effects in optical fibers originate from the third order susceptibility $\chi^{(3)}$. Most of the nonlinear effects are induced by nonlinear refraction. Nonlinear refraction, referred to as Kerr effect, changes the refraction in proportion to the intensity of the electrical field. The refractive index $\tilde{n}$ can be written as

$$\tilde{n} = n + n_2 \left|E\right|^2, \tag{1.27}$$

where n_2 is the nonlinear index coefficient related to $\chi^{(3)}$. The propagation of the optical signal in optical fibers including loss, chromatic dispersion, and nonlinear effect is described by the nonlinear Schrodinger equation (NLSE)

$$\frac{\partial A}{\partial z} = -\frac{\alpha}{2}A - \frac{j\beta_2}{2}\frac{\partial^2 A}{\partial T^2} + \frac{\beta_3}{6}\frac{\partial^3 A}{\partial T^3} + \gamma \mid A \mid^2 A, \tag{1.28}$$

where a frame of reference moving with the signal at the group velocity v_g is used by making the transformation

$$T = t - \frac{z}{v_g} \equiv t - \beta_1 z, \tag{1.29}$$

where A is the slowly varying amplitude of the signal envelope. The nonlinearity γ is defined as

$$\gamma = \frac{n_2\omega_0}{cA_{eff}}, \tag{1.30}$$

where A_{eff} is the effective mode area. The nonlinear phase shift depending on the intensity of the electrical field leads to a large number of interesting nonlinear effects. In transmission, self phase modulation (SPM) distorts the optical signal together with chromatic disperison. Additionally, the nonlinear phase noise is added because the

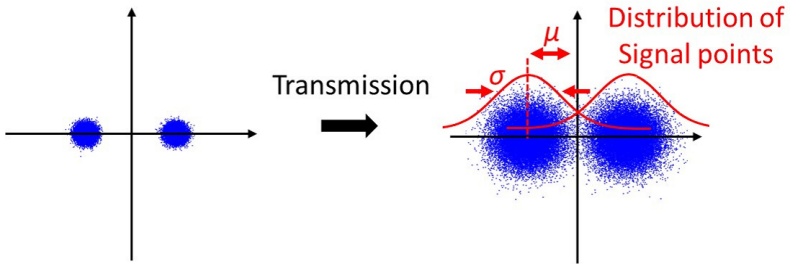

Figure 1.14: Signal degradation.

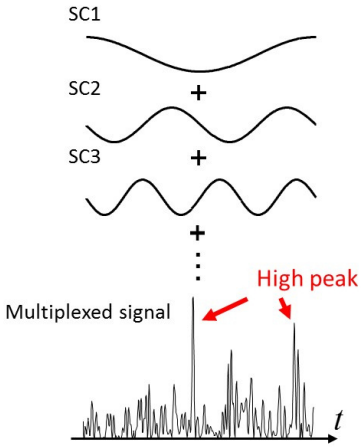

Figure 1.15: Waveform of OFDM signal.

WDM signal of each channel is modulated by other channels through cross phase modulaiton (XPM), and the cross talk occurs because the signals generate new spectral components outside the channel band by four wave mixing (FWM). These ICI by nonlinear distortion significantly degrades the signal quality, as shown in Fig. 1.13.

1.4.4 Signal quality of transmission signal

The signal quality of transmission signal is degraded by the ASE of optical amplifier, ISI, and ICI. Figure 1.14 shows the constellation before and after transmission. As a result of signal distortion, the distribution of the signal points is spread. The more the distribution is spread, the more the bit error occurs. Assuming that the distribution of the signal points follows a normal distribution, the signal quality Q is defined by,

$$\begin{aligned} Q &= 20log_{10}(q), \\ q &= \mu/\sigma, \end{aligned} \tag{1.31}$$

where μ is Euclidean distance between the adjacent level and σ is variance.

Signal quality is improved by increasing the signal power at the transmitter because the ASE noise of optical amplifier is large when the input power of the optical amplifier is small. However, the high signal power induces nonlinear distortion. The larger the phase shift, the larger the influence of nonlinear effect. The acute change of the intensity waveform of the signal significantly degrades the signal quality. Figure 1.15 shows the waveforms of each OFDM subcarrier and the multiplexed signal. Very high peaks locally forms due to the coherent superposition of many subcarriers in time domain. Although OFDM realizes a high density subcarrier multiplexing, OFDM signal has a disadvantage of very high peak-to-average power ratio (PAPR) and is distorted by nonlinear effect.

Compensation techniques of signal distortion by digital signal processing are proposed.[22–29] Since the propagation of the optical signal could be calculated by NLSE, the signal before the transmission is restored by solving NLSE toward a direction opposite to the propagation. This technique is called as digital back-propagation (DBP). Considering only chromatic dispersion, NLSE could be solved one step. The real-time operation is experimentally demonstrated.[30] For nonlinear compensation, NLSE is solved by the split-step Fourier method (SSFM). However, the computational cost of SSFM is estimated to be over 100 times greater than for dispersion compensation, thus it is difficult to implement in real-time.[31] Additionally, an experimental demonstration[32] suggests that DBP of a single carrier produces only a very small benefit in the presence of a large number of subcarriers. To calculate the all of subcarriers, the complete electrical field of all of subcarriers and the enormous computational cost are required.[33] Therefore, realization in a real-time system would be very difficult.

Another approach is the optical compensation using a phase conjunction wave.[34–37] Although the experimental demonstrations of simultaneous compensation of many subcarriers were reported,[38,39] phase conjunction wave generators must be installed at the exact center of the fiber. Therefore, this technique can not be used in established fiber links.

Recently, it is predicted that optical OFDM based on fractional Fourier transform (FrFT) in place of Fourier transform increases the system flexibility and suppresses signal impairments in the propagation.[40] If the signal degradation is mitigated, a multilevel modulation with high multiplicity is available. To treat the high multiplicity of multilevel modulation, the high resolution ADC is required.[41] However, performance

of conventional electrical ADCs are limited by the jitter of the sampling aperture and the power consumption. To overcome this limitation, optical approaches have recently attracted much attention because a mode locked laser, which provides an ultra-stable optical pulse stream, can offer a sampling aperture with ultra-low jitter, as low as a few femtoseconds. Although optical sampling using optical pulse streams with electrical quantization and coding processes realizes high-performance ADCs, multiple electrical ADCs are required to support a high sampling rate, and therefore, increased energy consumption is unavoidable. Using optical technology for the entire process, including the subsequent quantization and coding, should reduce energy consumption.

To get the best performance of a transmission system by optimizing its transfer function, it is important to clarify the behavior of a transmission signal in actual optical fiber links. Additionally, a feasibility demonstration of devices and subsystems such as implementation of signal processing and ADC in various environments is of considerable practical significance.

1.5 Conclusion

In this chapter, introduction of optical signal multiplexing in optical communication was presented as an essential procedure. Overviews of current situation in optical signal multiplexing for large capacity optical communications and various phenomena induced in optical fibers during transmission were described. To get the best performance of a transmission system for further large capacity optical communications, an optimization of a transfer function including an optical signal multiplexing is required.

Chapter 2

All-optical fractional orthogonal frequency division multiplexing

The frequency domain is not always optimum for all of applications, although it is used for powerful signal processing based on the Fourier transform. Fractional Fourier transform is expected to generalize the Fourier transform, and define a new domain which could provide more flexible signal processing. In this chapter, an innovative optical OFDM based on fractional Fourier transform in place of the conventional Fourier transform is presented. The theoretical backgrounds of fractional Fourier transform and the method of all-optical implementation of an optical signal are described. The behavior of optical fractional OFDM signal in a dispersive fiber focusing on the reduction of peak to average power ratio is clarified. Moreover, the fiber nonlinearity mitigation technique is proposed and demonstrated by evaluating the transmission performance of the fractional OFDM signal in the dispersion compensated fiber link in simulation.

2.1 Introduction

The Fourier transform plays an important role in almost all the science and technology fields[75] and is applied to widely applications such as infrared spectroscopy, X ray crystal structural analysis, and OFDM. In communication, OFDM exploits the orthogonal basis of the Fourier transform for high spectral efficiency. OFDM is a more recent approach in optical communication, and all-optical implementation of the Fourier transform has been attracted to reduce the energy consumption. Although OFDM realizes high spectral efficiency, OFDM has a disadvantage of very high PAPR

due to the coherent superposition of many subcarriers in a time domain. Since the high PAPR signal may induce serious nonlinear effects in fiber links, the signal quality could be degraded and the launchable power is limited. Since the Fourier transform decomposes a signal into the frequency components, a time domain relates to a frequency domain. However, the frequency domain is not always optimum for all of applications. The fractional Fourier transform (FrFT) is a generalization of the conventional Fourier transform.[76–86] The Fourier transform cannot obtain the local time-frequency character that is essential for processing nonstationary signals because it is a kind of holistic transform. Since the FrFT can handle time-varying signals in the FrFT domain, it is applied to flexible applications such as quantum mechanics, filtering in a FrFT domain, phase retrieval, and Neural networks. In wireless communication, the FrFT is introduced for compensations of Doppler shift and multipath fading.[87] Additionally, the PAPR reduction effect of FrFT based OFDM signal is reported.[88] Recently, it is predicted that optical OFDM based on FrFT in place of Fourier transform suppresses the PAPR and the chromatic dispersion impairment. To get the best performance of a transmission system by optimizing its transfer function, it is important to clarify the behavior of a transmission signal in actual optical fiber links. The major difference between optical communication and wireless communication is the presence of chromatic dispersion. Although there is no time-varying characteristic in optical transmission links, the waveform of the signal is largely distorted due to the delay depending on the frequency. Since, therefore, the PAPR is changed according to the propagation, the PAPR has been handled stochastically so far. However, if we can control the change of the PAPR with propagation, it is expected that the transmission performance is optimized according to the transmission link. In this chapter, we clarify the behavior of optical fractional OFDM signal in a dispersive fiber focusing on the reduction of PAPR. From obtained result, the fiber nonlinearity mitigation technique is proposed and demonstrated by evaluating the transmission performance of the fractional OFDM signal in the dispersion compensated fiber link in simulation.

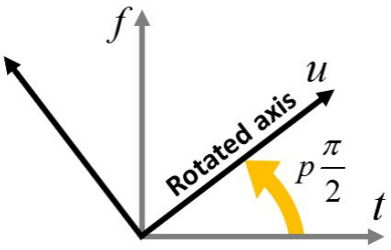

Figure 2.1: Fractional Fourier transform.

2.2 Principle of all-optical fractional OFDM

2.2.1 OFDM based on fractional Fourier transform

The conventional Fourier transform is defined as

$$X(f) = \mathcal{F}\{x(t)\}(f) = \int_{-\infty}^{\infty} x(t)e^{-j2\pi tf}dt, \tag{2.1}$$

where $x(t)$ is a function in time domain and $X(f)$ is a function in frequency domain. The Fourier transform is a projection of a signal on the frequency axis. In time-frequency plane, the signal is rotated $\pi/2$ with respect to the time axis. The FrFT is a generalization of the Fourier transform. The FrFT is defined as

$$\tilde{x}(u) = \mathcal{F}^p\{x(t)\}(u) = \int_{-\infty}^{\infty} x(t)K_p(t,u)dt, \tag{2.2}$$

where the transformation kernel $K_p(t,u)$ is described by

$$\begin{aligned} K_p(t,u) &= \begin{cases} \frac{e^{j\frac{\pi}{4}\{p-sign[sin(p\frac{\pi}{2})]\}}}{\sqrt{|sin(p\frac{\pi}{2})|}} e^{j\pi\left[(t^2+u^2)cot\left(p\frac{\pi}{2}\right)-2tucsc\left(p\frac{\pi}{2}\right)\right]} & (p \neq l) \\ \delta(t-u) & (p = 2l) \\ \delta(t+u) & (p = 2l+1) \end{cases} \\ l &\in \mathbb{Z}, \end{aligned} \tag{2.3}$$

where p is fractional parameter. The FrFT can be interpreted as the projection of the signal on an intermediate axis u that forms an angle $p\pi/2$, as shown in Fig. 2.1. The signal is rotated $p\pi/2$ with respect to the time axis. Setting $p = 1$, the FrFT is equal to the conventional Fourier transform. In OFDM, a subcarrier eq.(1.1) is an impulse output of Fourier transform. The time domain representation of an impulse function $\delta(u - nu_0)$ in the intermediate domain is given by

$$\begin{aligned} \tilde{\phi}_n^p(t) &= \mathcal{F}^{-p}\{\delta(u-nu_0)\}(t) \\ &= \frac{e^{j\frac{\pi}{4}\left\{-p-sign\left[sin\left(-p\frac{\pi}{2}\right)\right]\right\}}}{\sqrt{\left|sin\left(-p\frac{\pi}{2}\right)\right|}} e^{-j\pi\left[(t^2+(nu_0)^2)cot\left(p\frac{\pi}{2}\right)-2t(nu_0)csc\left(p\frac{\pi}{2}\right)\right]}. \end{aligned} \tag{2.4}$$

The integration for any two subcarriers along the whole symbol duration T is computed as

$$\begin{aligned}
&\int_{-T/2}^{T/2} \tilde{\phi}_n^p(t)\tilde{\phi}_m^{p*}(t)dt \\
&= \frac{1}{sin\left(p\frac{\pi}{2}\right)} e^{-j\pi(n^2-m^2)u_0^2 cot\left(p\frac{\pi}{2}\right)} \int_{-T/2}^{T/2} e^{-j\pi 2t(n-m)u_0 csc\left(p\frac{\pi}{2}\right)} dt \\
&= \begin{cases} \frac{T}{sin^2\left(p\frac{\pi}{2}\right)} & (m=n) \\ \frac{1}{-j(n-m)u_0 sin\left(p\frac{\pi}{2}\right)} e^{-j\pi(n^2-m^2)u_0^2 cot\left(p\frac{\pi}{2}\right)} e^{j(n-m)u_0(T/2)csc\left(p\frac{\pi}{2}\right)} & \\ \times\left\{e^{-j(n-m)u_0 T csc\left(p\frac{\pi}{2}\right)} - 1\right\} & (m\neq n) \end{cases} \\
&n, m \in \mathbb{Z}. \qquad (2.5)
\end{aligned}$$

If $\tilde{\phi}_n^p(t)$ satisfies the orthogonal condition, eq.(2.5) should equal zero in the case ($m \neq n$). This condition can be satisfied only when $u_0 = 2\pi(sin(p\pi/2)/T)$. By neglecting unessential constant terms, the subcarrier $\phi_n^p(t)$ and the multiplexed signal $x^p(t)$ of optical fractional OFDM is expressed as

$$x^p(t) = \sum_{n=0}^{N-1} s_n \phi_n^p(t), \qquad (2.6)$$

$$\phi_n^p(t) = rect\left(\frac{t}{T}\right) e^{-j\pi\left\{\left[n^2 sin^2\left(p\frac{\pi}{2}\right)+\frac{t^2}{T^2}\right]\cot\left(p\frac{\pi}{2}\right)-2\frac{n}{T}t\right\}}, \qquad (2.7)$$

where s_n is a data symbol. Fractional OFDM symbol could be demultiplexed by appling a complementary FrFT such as $-p$ at the reciever. Figure 2.2–2.7 show waveforms of optical fractional OFDM subcarriers in the case of $p = 1, 0.5, 0.1, -0.1, -0.5, -1$. The number of subcarriers is 8 and the symbol duration is 100 ps. Since each subcarrier has a quadratic chirp depending on p, the instant frequency is changed along to time. The fractional OFDM symbol is rotated an angle $(1-p)\pi/2$ from OFDM symbol in time-frequency plane, as shown in Fig. 2.8. Fractional OFDM symbol could be demultiplexed by appling a complementary FrFT such as $-p$ at the reciever.

2.2.2 Implementation of all-optical fractional Fourier transform

The FrFT could be implemented by passive optical components as with the case of all-optical IDFT/DFT.[89–91] Figure 2.9 shows the principle of all-optical FrFT with optical

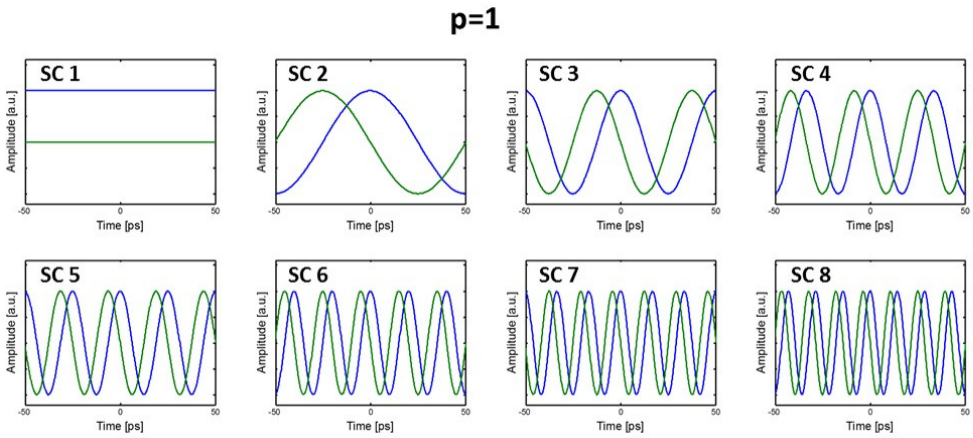

Figure 2.2: Waveforms of optical fractional OFDM subcarriers in the case of $p = 1$.

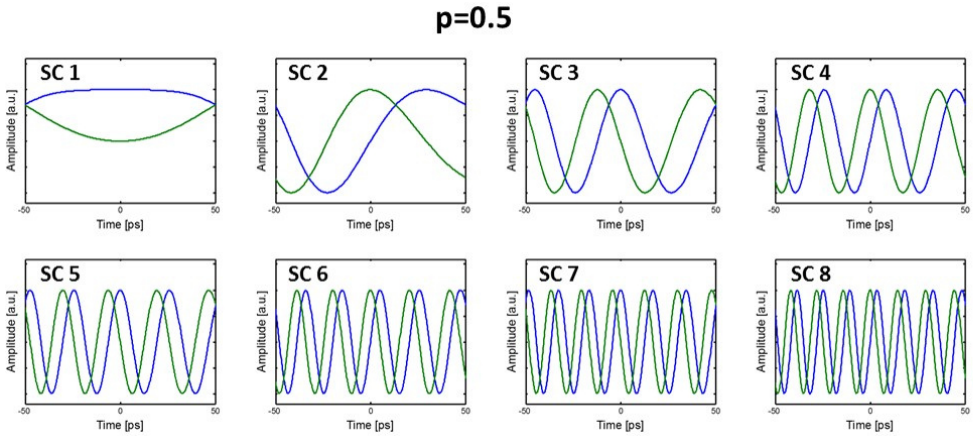

Figure 2.3: Waveforms of optical fractional OFDM subcarriers in the case of $p = 0.5$.

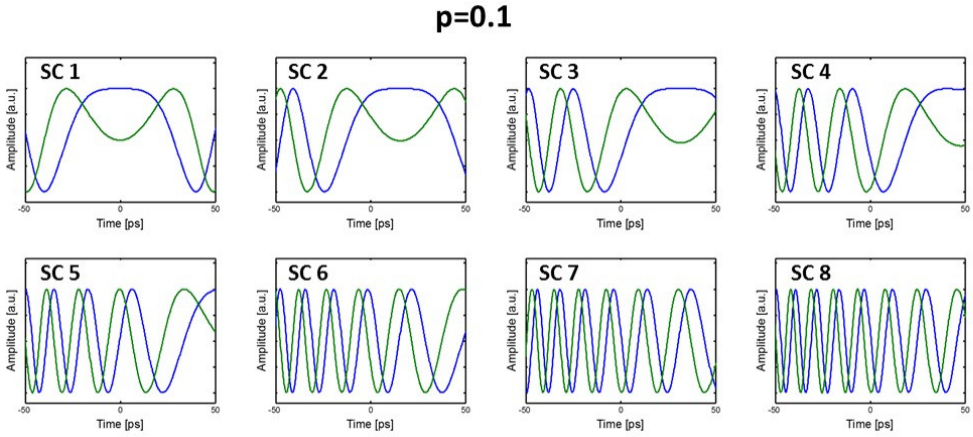

Figure 2.4: Waveforms of optical fractional OFDM subcarriers in the case of $p = 0.1$.

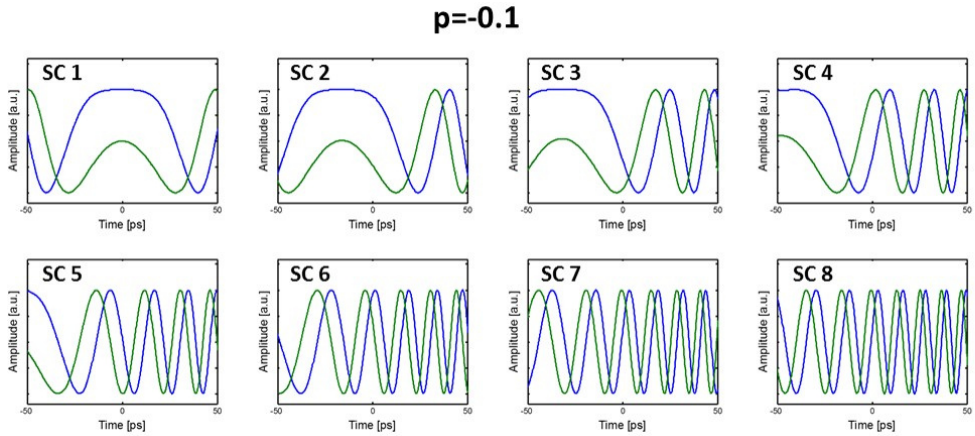

Figure 2.5: Waveforms of optical fractional OFDM subcarriers in the case of $p = -0.1$.

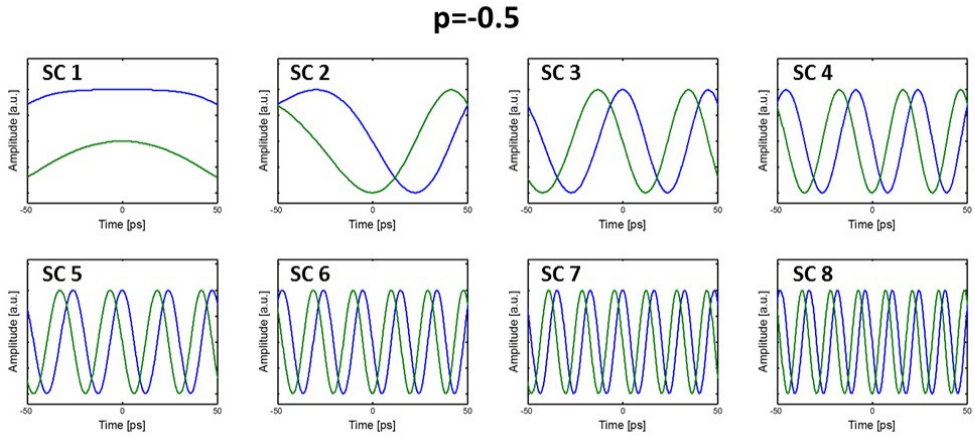

Figure 2.6: Waveforms of optical fractional OFDM subcarriers in the case of $p = -0.5$.

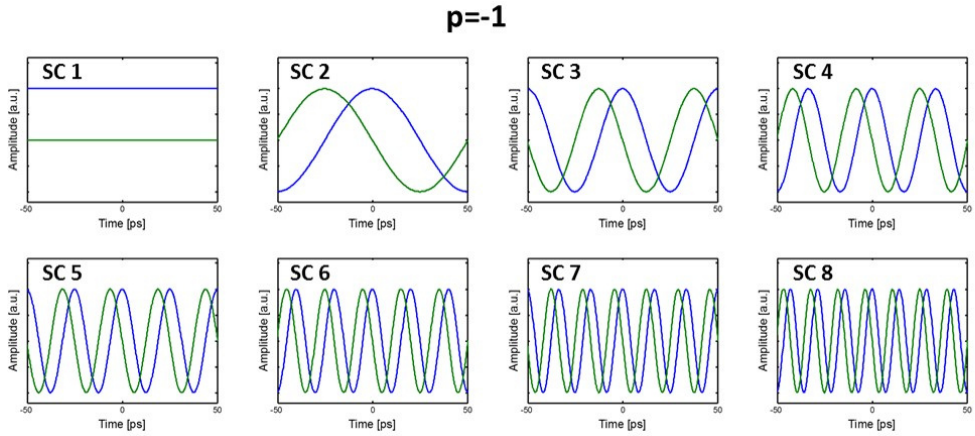

Figure 2.7: Waveforms of optical fractional OFDM subcarriers in the case of $p = -1$.

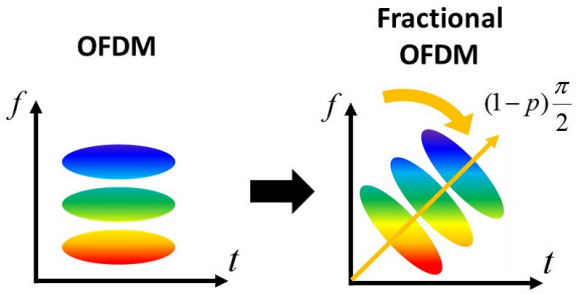

Figure 2.8: Fractional OFDM signal in time-frequency plane.

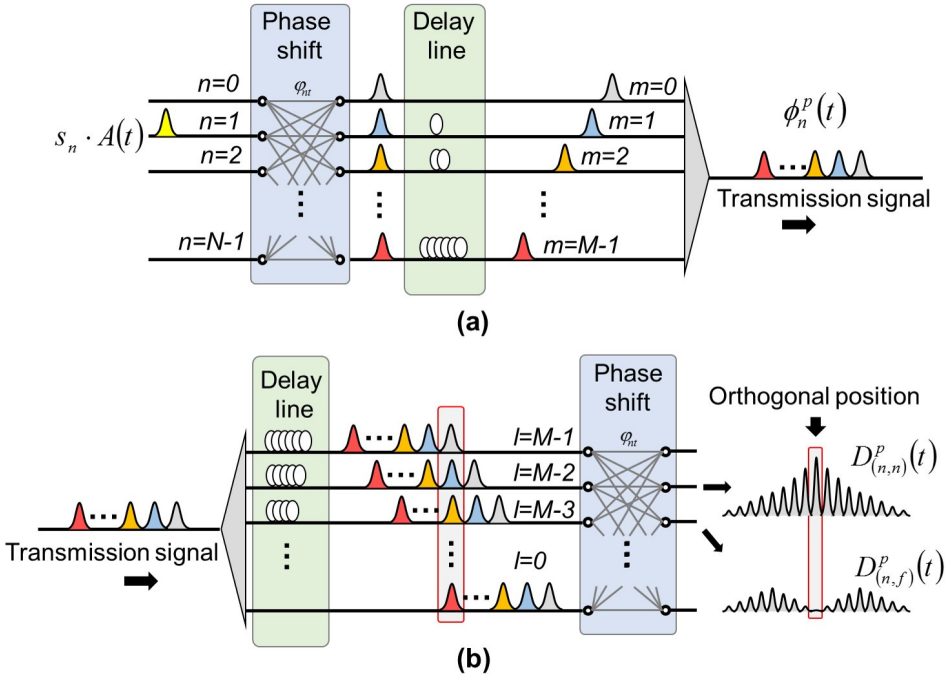

Figure 2.9: All-optical implementation of fractional Fourier transform.

delay lines and phase shifters. The discretized nth subcarrier of the fractional OFDM is expressed by

$$\begin{aligned}\phi_n^p(t) &= \sum_{m=0}^{M-1} s_n \cdot A(t + m \cdot \tau) \\ &\quad \times e^{-j\pi\left\{\left[n^2 sin^2(p\frac{\pi}{2}) + \frac{(m-(M-1)/2)^2}{M^2}\right] cot\left(p\frac{\pi}{2}\right) - 2n\frac{m-(M-1)/2}{M}\right\}},\end{aligned} \tag{2.8}$$

where the parameter p is the fractional order, $A(t)$ is the shape of an optical pulse, and M is the number of sample within the symbol duration T. In order to set the center position of the chirp to the center of the symbol, the index m starts from $-(M-1)/2$. The all-optical FrFT can be implemented in the same manner as the

all-optical IDFT/DFT with modifying phase shifters. The fractional OFDM symbol can be demultiplexed by applying a complementary FrFT such as $-p$. The output signals of the corresponding nth and non-corresponding fth FrFT $(-p)$ are expressed by

$$\begin{aligned} D^p_{(n,n)}(t) &= \sum_{l=0}^{M-1} \phi^p_n(t) \\ &\quad \times e^{-j\pi\left\{\left[n^2 sin^2(-p\frac{\pi}{2})+\frac{(l-(M-1)/2)^2}{M^2}\right]cot\left(-p\frac{\pi}{2}\right)-2n\frac{l-(M-1)/2}{M}\right\}} \\ &= \sum_{l=0}^{M-1}\sum_{m=0}^{M-1} s_n \cdot A(t+(m+l)\cdot\tau) \\ &\quad \times e^{-j\pi\left\{\left[\left(m-\frac{M-1}{2}\right)^2-\left(l-\frac{M-1}{2}\right)^2\right]\frac{cot(-p\pi/2)}{M^2}-2n\frac{m+l-(M-1)}{M}\right\}}, \end{aligned} \tag{2.9}$$

$$\begin{aligned} D^p_{(n,f)}(t) &= \sum_{l=0}^{M-1} \phi^p_n(t) \\ &\quad \times e^{-j\pi\left\{\left[f^2 sin^2(-p\frac{\pi}{2})+\frac{(l-(M-1)/2)^2}{M^2}\right]cot\left(-p\frac{\pi}{2}\right)-2f\frac{l-(M-1)/2}{M}\right\}} \\ &= \sum_{l=0}^{M-1}\sum_{m=0}^{M-1} s_n \cdot A(t+(m+l)\cdot\tau) \\ &\quad \times e^{-j\pi\left\{(n^2-f^2)sin^2(p\frac{\pi}{2})\frac{cot(p\pi/2)}{M^2}\right\}} \\ &\quad \times e^{-j\pi\left\{\left[\left(m-\frac{M-1}{2}\right)^2-\left(l-\frac{M-1}{2}\right)^2\right]\frac{cot(-p\pi/2)}{M^2}-\frac{2}{M}\left(nm+fl-\frac{(M-1)(n+f)}{2}\right)\right\}}. \end{aligned} \tag{2.10}$$

At the position $m+l=M-1$, which is equal to $t_s=(M-1)\tau$ the signals are expressed by

$$D^p_{(n,n,t_s)}(t) = M \cdot s_n \cdot A(t), \tag{2.11}$$

$$\begin{aligned} D^p_{(n,f,t_s)}(t) &= s_n \cdot A(t) \cdot \beta \cdot \sum_{m=0}^{M-1} e^{\frac{j2\pi}{M}\left(m(n-f)+(M-1)f-\frac{(M-1)(n+f)}{2}\right)} \\ &= s_n \cdot A(t) \cdot \beta \cdot e^{\frac{j2\pi}{M}(M-1)(n+f)} \sum_{m=0}^{M-1} e^{\frac{j2\pi}{M}m(n-f)} \\ &= s_n \cdot A(t) \cdot \beta \cdot e^{\frac{j2\pi}{M}(M-1)(n+f)} \sum_{m=0}^{M-1} e^{\frac{j2\pi}{M}m(n-f)} \frac{1-e^{\frac{j2\pi}{M}M(n-f)}}{1-e^{\frac{j2\pi}{M}(n-f)}} \\ &= 0, \end{aligned} \tag{2.12}$$

where β is the term unrelated to the summation. Thus, the fractional OFDM subcarriers also have orthogonality at the same sample as OFDM. The all-optical FrFT

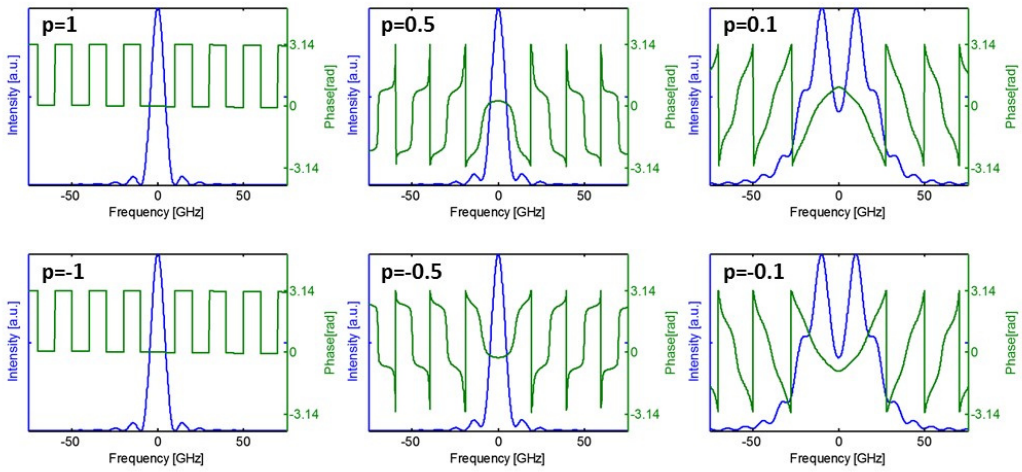

Figure 2.10: Spectra of optical fractional OFDM subcarriers in the case of $p = 1, 0.5, 0.1, -0.1, -0.5, -1$.

circuit serves as the special optical filter. Thus a time-space conversion based optical spectral shaper could also implement the all-optical FrFT. The filter functions of fractional OFDM subcarriers are obtained by Fourier transform of eq. (2.7). Figure 2.10 shows the spectra of optical fractional OFDM subcarriers in the case of $p = 1, 0.5, 0.1, -0.1, -0.5, -1$. The spectrum is broadened compared with conventional OFDM signal ($p = 1$). The subcarrier correcponding to $-p$ has inverse phase in frequency domain. All subcarriers have the same spectrum, shifted of $1/T$.

2.3 Peak to average power ratio reduction using all-optical fractional OFDM

2.3.1 Generation of Nyquist pulse train using time-lens effect

Eq.(2.7) of fractional OFDM subcarrier could be written by,

$$\phi_n^p(t) = e^{-j\pi n^2 sin^2\left(p\frac{\pi}{2}\right)cot\left(p\frac{\pi}{2}\right)}\phi_n^1(t)e^{-j\pi\frac{cot\left(p\frac{\pi}{2}\right)}{T^2}t^2}. \tag{2.13}$$

This means that OFDM subcarrier is multiplied a quadratic phase in time domain. The time-lens effect could be induced by a convolution processing of a quadratic phase which is realized by a propagation of a fiber with total dispersion D that satisfies the condition

$$D = -cT^2 tan\left(p\pi/2\right)/\lambda^2, \tag{2.14}$$

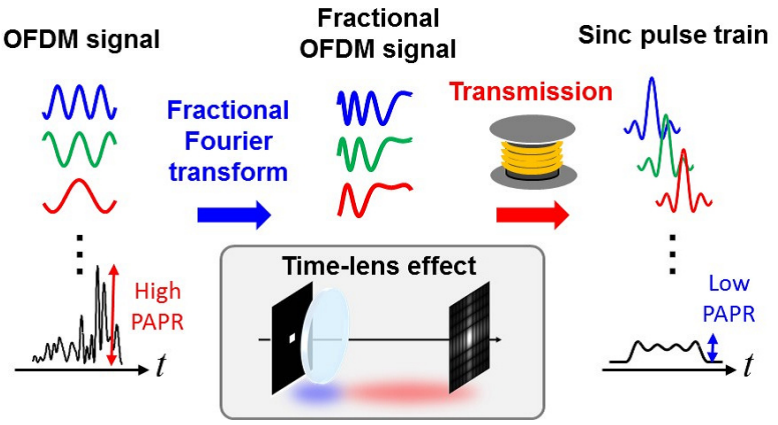

Figure 2.11: Generation of Nyquist pulse train using time-lens effect.

where c is the speed of light and λ is the central wavelength.[92]

$$\begin{aligned}
\phi_n^p(t) \otimes e^{-j\frac{\pi c}{\lambda^2 D}t^2} &= e^{-j\pi n^2 sin^2\left(p\frac{\pi}{2}\right)cot\left(p\frac{\pi}{2}\right)} \int \phi_n^1(\tau) e^{-j\pi\frac{cot\left(p\frac{\pi}{2}\right)}{T^2}\tau^2} e^{-j\frac{\pi c}{\lambda^2 D}(\tau-t)^2} d\tau \\
&= e^{-j\pi n^2 sin^2\left(p\frac{\pi}{2}\right)cot\left(p\frac{\pi}{2}\right)} e^{j\pi\frac{cot\left(p\frac{\pi}{2}\right)}{T^2}t^2} \int \phi_n^1(\tau) e^{-2j\pi\frac{cot\left(p\frac{\pi}{2}\right)}{T^2}\tau t} d\tau \\
&= e^{-j\pi n^2 sin^2\left(p\frac{\pi}{2}\right)cot\left(p\frac{\pi}{2}\right)} e^{j\pi\frac{cot\left(p\frac{\pi}{2}\right)}{T^2}t^2} \mathcal{F}\left\{\phi_n^1(\tau)\right\}\left(\frac{cot\left(p\frac{\pi}{2}\right)}{T^2}t\right) \\
&= T e^{j\pi\frac{cot\left(p\frac{\pi}{2}\right)}{T^2}t^2} e^{-j\pi n^2 sin^2\left(p\frac{\pi}{2}\right)cot\left(p\frac{\pi}{2}\right)} s_n sinc\left(\frac{t}{\Delta t'} - n\Delta t'\right), \quad (2.15)
\end{aligned}$$

$$\begin{aligned}
x^p(t) \otimes e^{-j\frac{\pi c}{\lambda^2 D}t^2} &= T e^{j\pi\frac{cot\left(p\frac{\pi}{2}\right)}{T^2}t^2} \sum_{n=0}^{N-1} e^{-j\pi n^2 sin^2\left(p\frac{\pi}{2}\right)cot\left(p\frac{\pi}{2}\right)} s_n sinc\left(\frac{t}{\Delta t'}\right) \otimes \delta(t - n\Delta t'), \quad (2.16)
\end{aligned}$$

where $\Delta t' = Ttan(p\pi/2)$ is the interval of each subcarrier. Fracitonal OFDM subcarriers are converted to sinc pulses, referred to as Nyquist pulse, and have different time shift, as shown in Fig. 2.11. Since the overlapping of subcarriers in time domain is smaller than the OFDM signal, the Nyquist pulse train has the low PAPR characteristic. Thus it is expected that the PAPR of the fractional OFDM signal decreases according to the propagation of a fiber link by forming to a Nyquist pulse train.

2.3.2 Examination of PAPR reduction

We examined the PAPR reduction effect by formation of a Nyquist pulse train using a fractional OFDM symbol in a simulation. We used 12 × 10 Gbaud/s 16 QAM fractional

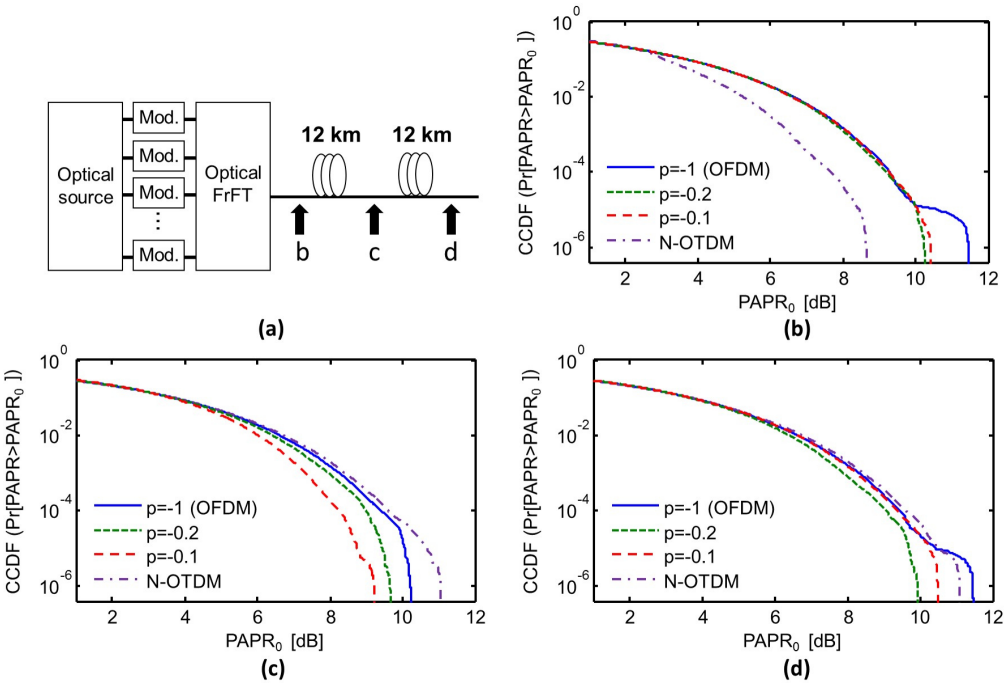

Figure 2.12: (a) Simulation setup. (b) Simulation result of the PAPR before propagation. (c) Simulation result of the PAPR after 12 km propagation. (d) Simulation result of the PAPR after 24 km propagation.

OFDM signals for the simulation. The simulation setup is shown in Fig. 2.12(a). The optical source emitted 1.5 ps pulses at a 10 GHz repetition rate. The center wavelength was 1550 nm. The pulses were split into 12 copies for 12 subcarriers. Each subcarrier was modulated by 16 QAM format at 10 GHz speed and multiplied a spatial filter of FrFT in frequency domain with time-space conversion based optical spectral shaping. The subcarriers were spaced at 10 GHz. We simulated $p = -1$ (conventional OFDM), $p = -0.2$, and $p = -0.1$ fractional OFDM signals. For a comparison, we prepared a same data capacity Nyquist-optical time division multiplexing (N-OTDM)[93–100] signal whose number of subcarrier was 12. The N-OTDM signal is a series of sinc pulses delayed of $\Delta t = T/N$,

$$x^0(t) = \sum_{n=0}^{N-1} s_n \cdot sinc\left(\frac{t}{\Delta t}\right) \otimes \delta\left(t - n\Delta t\right). \tag{2.17}$$

The system had a data capacity of 480 Gbit/s per polarization. We used only a single polarization. The number of symbol was 4000. The symbols were passed to a linear model of a dispersive fiber. The fiber dispersion was 17 ps/nm/km.

Figure 2.12(b-d) show the results of the complementary cumulative distribution

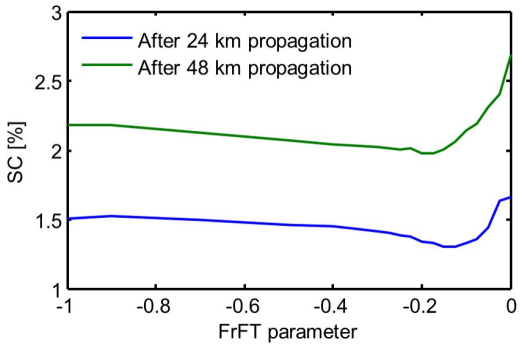

Figure 2.13: Relationship between the FrFT parametar p and the changes of spectra.

function (CCDF) of the PAPR. Figure 2.12(b) is the result before transmission. The N-OTDM signal has the lowest PAPR. On the other hand, Fig. 2.12(c, d) are the results after 12 km propagation and 24 km propagation. The PAPR of N-OTDM was grown by an increase of the subcarrier overlapping because chromatic dispersion significantly broadens the short pulse. The $p = -0.1$ fractional OFDM signal is the best result after 12 km propagation and The $p = -0.2$ fractional OFDM symbol is the best result after 24 km propagation. These results agree with the relationship of eq. (2.14) and confirm that the PAPR becomes lower as approaching the point where the transmission signal forms to a Nyquist pulse train.

2.3.3 Influence of nonlinear distortion

From the above simulation results in subsection 2.3.2, it is expected that the influence of nonlinear distortion is effectively relaxed depending on the FrFT parameter. We investigated the influence of nonlinear distortion using spectral changes before and after the propagation. For simplification, we considered only the effects of dispersion and nonlinearity. The fiber dispersion and nonlinearity were 17 ps/nm/km and 1.3 /W/km, respectively. The launch power was 1 dBm. The propagation was calculated by split step Fourier method. The spectral change SC is defined by

$$SC = \frac{\int_{-\infty}^{\infty} |S_{after}(f) - S_{before}(f)|\, df}{\int_{-\infty}^{\infty} S_{before}(f)\, df} \times 100, \tag{2.12}$$

where S_{before} and S_{after} are the intensity of spectra before and after the propagation. Figure 2.13 shows the relationship between the FrFT parameter p and the spectral change. After transmission of 24 km, the spectral change of $p = -0.1$ signal is the

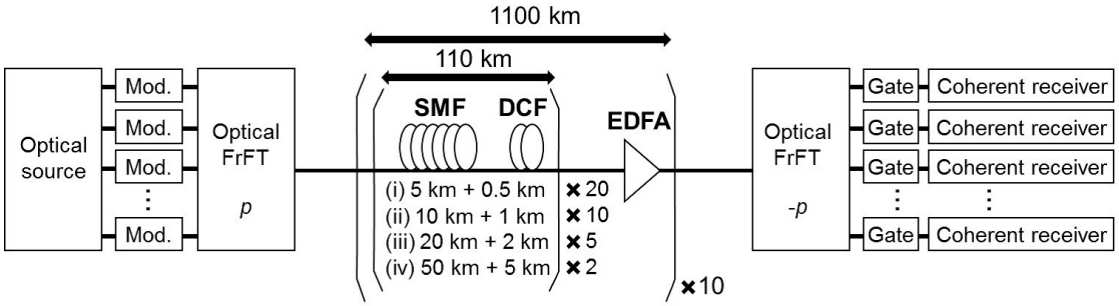

Figure 2.14: Simulation setup of the transmission of an all-optical fractional OFDM signal.

smallest. After transmission of 48 km, the spectral change of $p = -0.2$ signal is the smallest. These lengths are twice as long as the lengths that induce a time-lens effect. These results indicate that setting FrFT parameter p so as to transform the transmission signal into a Nyquist pulse train at the middle of the fiber, the nonlinear distortion in whole fiber could be mitigated.

2.4 Fiber nonlinearity mitigation using all-optical fractional OFDM

To assess the proposed fiber nonlinearity mitigation technique through the all-optical fractional OFDM, we evaluated the performance of the transmission of a fractional OFDM signal in the dispersion compensated fiber link. Figure 2.14 shows a transmission simulation setup. The condition of the transmitter side was same as subsection 2.3.2. Length of transmission link was 1100 km and EDFA was set at 110 km length intervals. We assumed that the dispersion of SMF is compensated by dispersion compensation fibers (DCF) at regular length intervals. We simulated four cases; (i) 5 km SMF (loss: 0.2 dB/km, dispersion: 17 ps/nm/km, nonlinearity: 1.3 /W/km) and 0.5 km DCF (loss: 0.2 dB/km, dispersion: -170 ps/nm/km, nonlinearity: 1.3 /W/km) link, (ii) 10 km SMF and 1 km DCF link, (iii) 20 km SMF and 2 km DCF link, and (iv) 50 km SMF and 5 km DCF link. The noise figure of the EDFA was 4 dB. At the receiver side, fractional OFDM and N-OTDM symbols were demultiplexed by suitable FrFT and time sampling using a WSS and a 1 ps time gate. Demultiplexed symbols were detected by coherent receivers with 50 GHz electrical bandwidth. The performance of the detected signal was evaluated by the Q-factor of electrical signals after

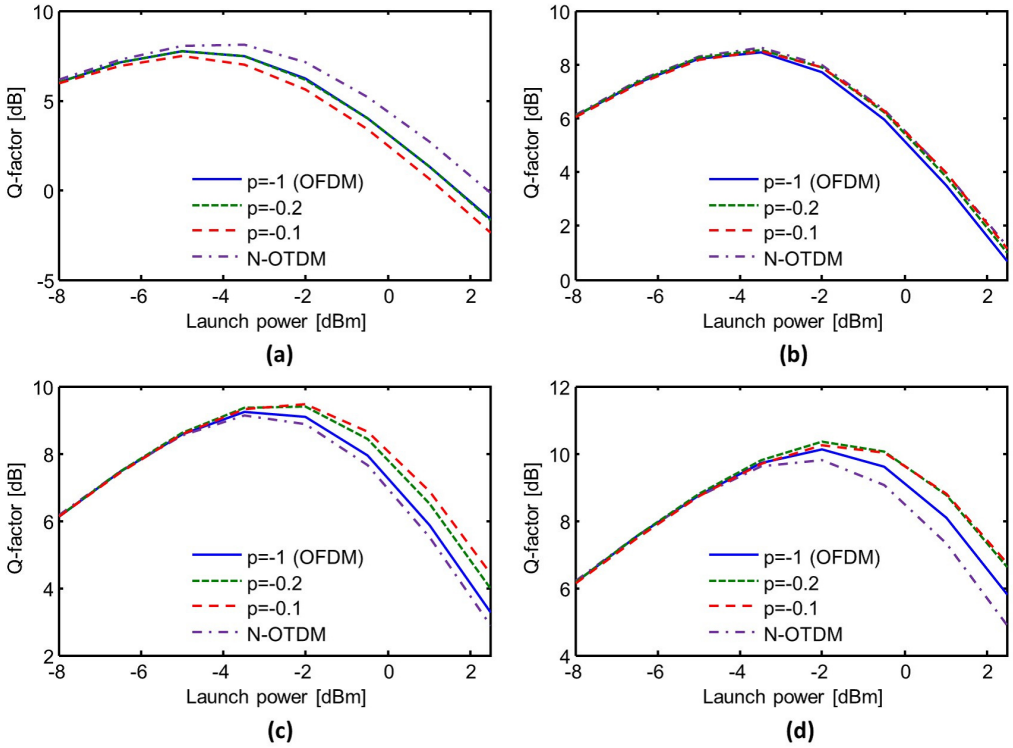

Figure 2.15: Simulation results of launch power versus Q-factor in (a) 5 km SMF and 0.5 km DCF link, (b) 10 km SMF and 1 km DCF link, (c) 20 km SMF and 2 km DCF link, and (d) 50 km SMF and 5 km DCF link.

the coherent receiver. Figure 2.15(a, b) shows the calculated results of the case (i) and (ii). Since the influence of dispersion is small, the N-OTDM symbol is the best signal quality. However, when the dispersion is compensated at long span, fractional OFDM symbols have better signal quality in the high launch power range as shown in Fig. 2.15(c, d). Figure 2.16 shows the constellation map of $p = -1$ and $p = -0.1$ at launch power 1 dBm in 20 km SMF and 2 km DCF link. The received signal of $p = -0.1$ is improved by 1.0 dB as compared with $p = -1$. These results indicate that the fiber nonlinearity could be mitigated by all-optical fractional OFDM with an appropriate FrFT parameter p. In this approach, there is no requirement of additional cost and power consumption because an all-optical fractional OFDM requires only replacement of the filter from conventional all-optical OFDM.

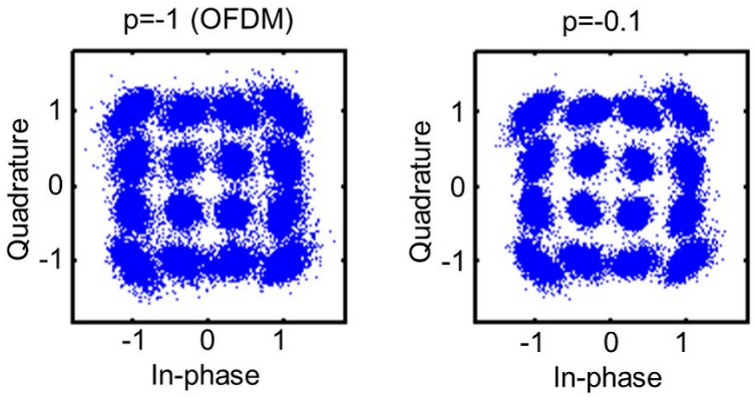

Figure 2.16: Simulation result of the constellation map of p=-1 and p=-0.1 at launch power 1dBm in 20 km SMF and 2 km DCF link.

2.5 Conclusion

In this chapter, an optical OFDM based on FrFT in place of conventional Fourier transform was presented. It is expected that the FrFT can handle signals in a new domain for more frexible applications than the conventinal Fourier transform. The theoretical backgrounds of FrFT and the method of all-optical implementation for an optical signal was described. The behavior of optical fractional OFDM signal in a dispersive fiber focusing on the reduction of peak to average power ratio was examined. The numerical simulation results show that the PAPR of fractional OFDM signal is decreased at a point where the Nyquist pulse train is formed by the time-lens effect. Moreover, the fiber nonlinearity mitigation technique was proposed and demonstrated by evaluating the transmission performance of the optical fractional OFDM signal in the dispersion compensated fiber link in simulation. The signal quality after the 1100 km propagation of a dispersion compensated fiber link was successfully improved by 1.0 dB as compared with the conventional OFDM. Since the PAPR is increased when the number of subcarriers is increased, it is expected that the effect of the proposed approach could be enhanced. This new FrFT based optimization approach for a control of a PAPR of a optical signal is useful to increase usable information.

Chapter 3

Cyclic prefix insertion for all-optical Fractional OFDM

In this chapter, to confirm that the FrFT can generalize the Fourier transform with keeping original useful functions in the Fourier transform, a verification of cyclic prefix insertion for all-optical fractional OFDM is presented. Since cyclic prefix exploits a periodicity of the DFT to reduce linear impairments such as chromatic dispersion in conventional OFDM, it is expected that a cyclic prefix is also effective for a fractional OFDM signal. The cyclic prefix insertion for all-optical fractional OFDM is experimentally demonstrated. The relationship between a fractional parameter and an effect of cyclic prefix insertion is investigated in simulation.

3.1 Introduction

In the previous chapter, it was found that the nonlinear signal distortion could be mitigated by all-optical fractional OFDM. Although it is assumed that the chromatic dispersion of the transmission link is completely compensated by DCF, in the actual link, there are cases where the chromatic dispersion is not completely compensated due to the temperature dependency and wavelength dependency of optical fibers.[101–106] The permissible residual dispersion becomes smaller when the data rate is high because the influence of dispersion is depending on spectral width. In conventional OFDM, a cyclic prefix (CP) is an essential technique for reducing the ISI and ICI in the presence of fiber dispersion because the orthogonality of the subcarriers with CP is maintained even if each subcarrier receives a different delay.[6,8,107] An all-optical implementation of inserting a CP has also been reported, and further tolerance of practical difficulties

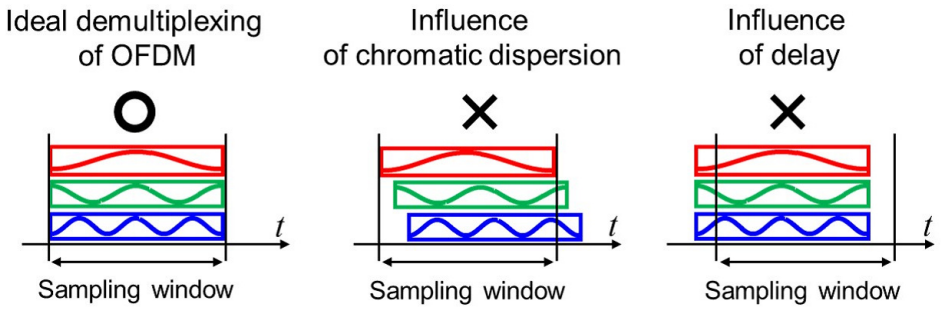

Figure 3.1: Timing error of demultiplexing of OFDM signal.

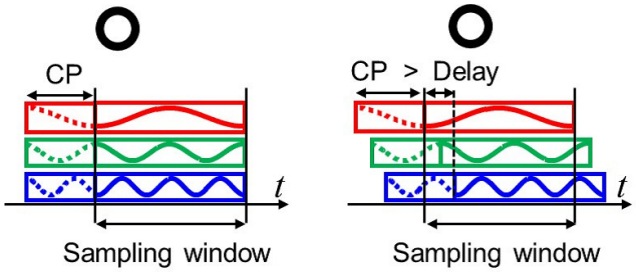

Figure 3.2: Cyclic prefix insertion.

such as timing errors of an actual receiver is expected in addition to the resistance to fiber dispersion.[108–110] The CP of OFDM is based on continuity at the end and the beginning of a waveform. Although the end and the beginning of subcarriers of fractional OFDM are not continuous, the CP of fractional OFDM is partially available unless $p = 0$. In this chapter, the CP insertion for all-optical fractional OFDM is verified and experimentally demonstrated. Moreover, the relationship between the fractional parameter p and the effect of CP insertion is investigated in simulation.

3.2 All-optical fractional OFDM with cyclic prefix

In order to demultiplex the OFDM signal, the signal must be extracted at an appropriate timing over the symbol duration. When there is the chromatic dispersion, it is impossible to extract all the subcarriers at an appropriate timing because each subcarrier has different delay. Since the orthogonality of the subcarriers is destroyed and a sampling window includes a neighboring symbol, the signal quality is degraded by ICI and ISI. In OFDM, a CP is a solution to this ICI and ISI. The beginning of the waveform is copied and added to the end of the waveform. Since exactly n cycles of sin wave are included in the symbol duration T, the sin wave of each subcarrier is

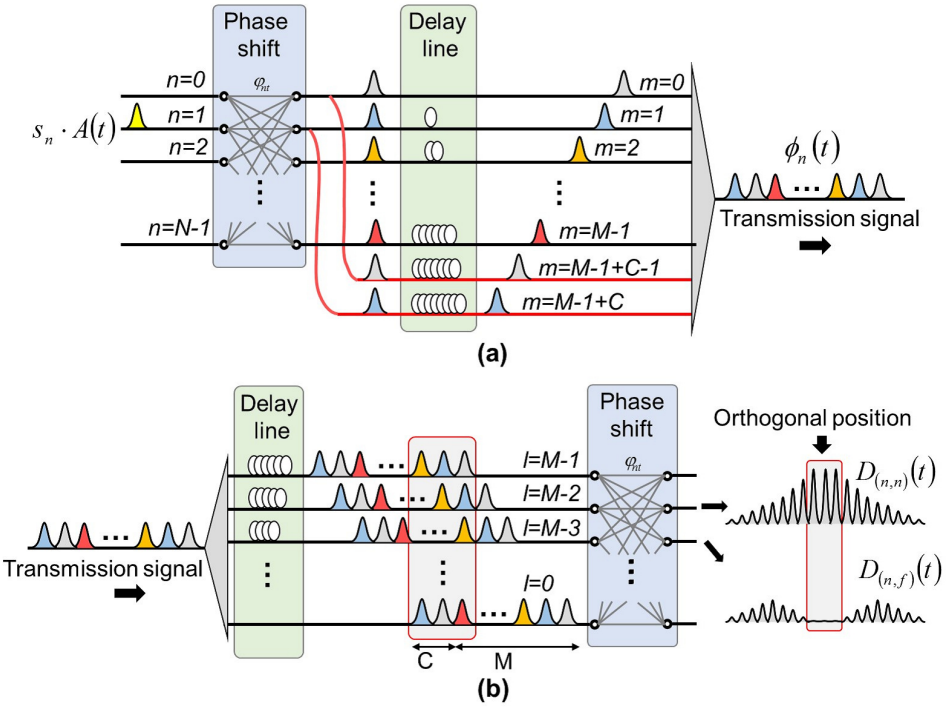

Figure 3.3: All-optical implementation of cyclic prefix.

extended backward. If the sampling window is in the extended symbol duration, the orthogonality is maintained because the orthogonality of eq.(1.4) is not depending on the phase. As long as the length of CP is larger than the delay, the subcarriers could be demultiplexed without ICI and ISI.

Figure 3.3(a) shows the all-optical IDFT with a CP. The beginning of the waveform generated by the IDFT is copied and added to the end of the waveform. The nth subcarrier with the CP is expressed by

$$\begin{aligned}\phi_n^1(t) &= \sum_{m=0}^{M-1} s_n \cdot A(t+m\cdot\tau) exp\left(j2\pi n\frac{m}{M}\right) + \sum_{c=0}^{C-1} s_n \cdot A(t+(M+c)\cdot\tau) exp\left(j2\pi n\frac{c}{M}\right) \\ &= \sum_{m=0}^{M+C-1} s_n \cdot A(t+m\cdot\tau) exp\left(j2\pi n\frac{m}{M}\right), \end{aligned} \tag{3.1}$$

where C is the number of the CP. The delay time between each sample shortens to $\tau = T/(M+C)$. The output signals of the corresponding nth DFT and non-corresponding

fth DFT are expressed by

$$\begin{aligned} D^1_{(n,n)}(t) &= \sum_{l=0}^{M-1} \phi^1_n(t) exp\left(j2\pi n \frac{l}{M}\right) \\ &= \sum_{l=0}^{M+C-1} \sum_{m=0}^{M-1} s_n \cdot A(t+(m+l)\cdot\tau) exp\left(j2\pi n \frac{m+l}{M}\right), \end{aligned} \tag{3.2}$$

$$\begin{aligned} D^1_{(n,f)}(t) &= \sum_{l=0}^{M-1} \phi^1_n(t) exp\left(j2\pi f \frac{l}{M}\right) \\ &= \sum_{l=0}^{M-1} \sum_{m=0}^{M+C-1} s_n \cdot A(t+(m+l)\cdot\tau) exp\left(j2\pi n \frac{nm+fl}{M}\right). \end{aligned} \tag{3.3}$$

At the position from $m+l = M-1$ to $m+l = M+C-1$, the output signal completely includes the components of the subcarrier. According to the same analysis with eq. (1.10) and(1.12), orthogonality is maintained at these positions. Thus, the orthogonal position can be increased to $C+1$ by the CP.

The CP of OFDM is based on continuity at the end and beginning of a waveform. In fractional OFDM, the end and beginning of subcarriers are not continuous. This may decrease the effectiveness of the CP for fractional OFDM. The nth subcarrier with a CP is expressed by

$$\begin{aligned} \phi^p_n(t) &= \sum_{m=0}^{M+C-1} s_n \cdot A(t+m\cdot\tau) \\ &\quad \times e^{-j\pi\left\{\left[n\ 2sin\ 2(p\frac{\pi}{2}) + \frac{(m-(M+C-1)/2)^2}{M^2}\right] cot\left(p\frac{\pi}{2}\right) - 2n\frac{m-(M+C-1)/2}{M}\right\}}. \end{aligned} \tag{3.4}$$

Here, the delay time between each sample is shortened to $\tau = T/(M+C)$. The output signals of the corresponding nth and non-corresponding fth FrFT $(-p)$ are expressed by

$$\begin{aligned} D^p_{(n,n)}(t) &= \sum_{l=0}^{M-1} \sum_{m=0}^{M+C-1} s_n \cdot A(t+(m+l)\cdot\tau) \\ &\quad \times e^{-j\pi\left\{\left[\left(m-\frac{M+C-1}{2}\right)^2 - \left(l-\frac{M-1}{2}\right)^2\right]\frac{cot(-p\pi/2)}{M^2}\right\}} \\ &\quad \times e^{\frac{j2\pi}{M}\left\{m+l-\left(\frac{2M+C}{2}-1\right)\right\}}, \end{aligned} \tag{3.5}$$

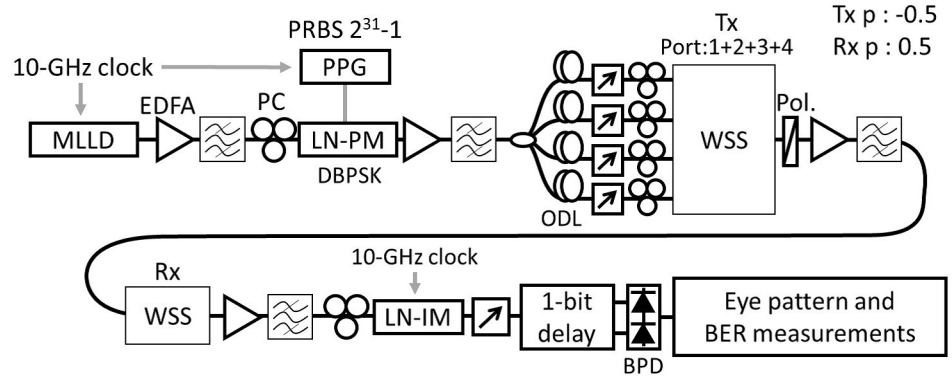

Figure 3.4: Experimental setup for DBPSK modulated fractional OFDM transmitter and receiver with a CP.

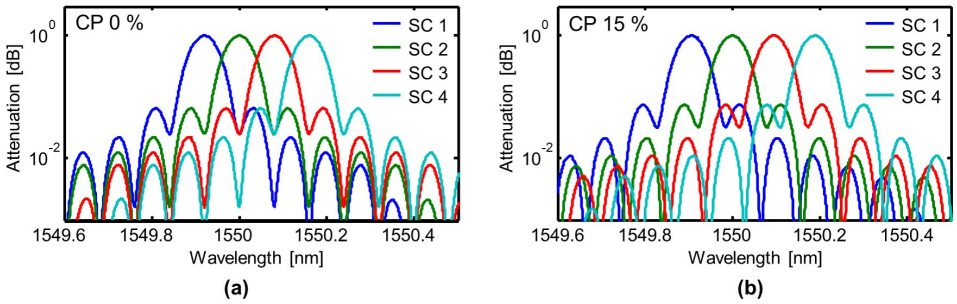

Figure 3.5: Transfer functions installed on the WSS without and with the CP.

$$
\begin{aligned}
D^{p}_{(n,f)}(t) \;=\; & \sum_{l=0}^{M-1}\sum_{m=0}^{M+C-1} s_n \cdot A(t+(m+l)\cdot\tau) \\
& \times e^{-j\pi\left\{(n^2-f^2)sin^2(p\frac{\pi}{2})\frac{cot(-p\pi/2)}{M^2}\right\}} \\
& \times e^{-j\pi\left\{\left[\left(m-\frac{M+C-1}{2}\right)^2-\left(l-\frac{M-1}{2}\right)^2\right]\frac{cot(-p\pi/2)}{M^2}\right\}} \\
& \times e^{\frac{j2\pi}{M}\left\{nm+fl-\frac{(M-1)(n+f)+Cn}{2}\right\}}. \qquad (3.6)
\end{aligned}
$$

At the position $m+l=(2M+C)/2-1$, the signals are the same as in eq. (2.11) and (2.12). However, even if the position is from $m+l=M-1$ to $m+l=M+C-1$, the ICI occurs because of the terms related to the quadratic chirps. The amount of ICI depends on the parameter p.

3.3 Experimental demonstration

Figure 3.4 shows the experimental setup for the fractional OFDM based transmitter and receiver with a CP. We set p = -0.5 at the transmitter and p = 0.5 at the receiver for an 4 subcarriers fractional OFDM and added a CP of 15%. An all-optical FrFT was

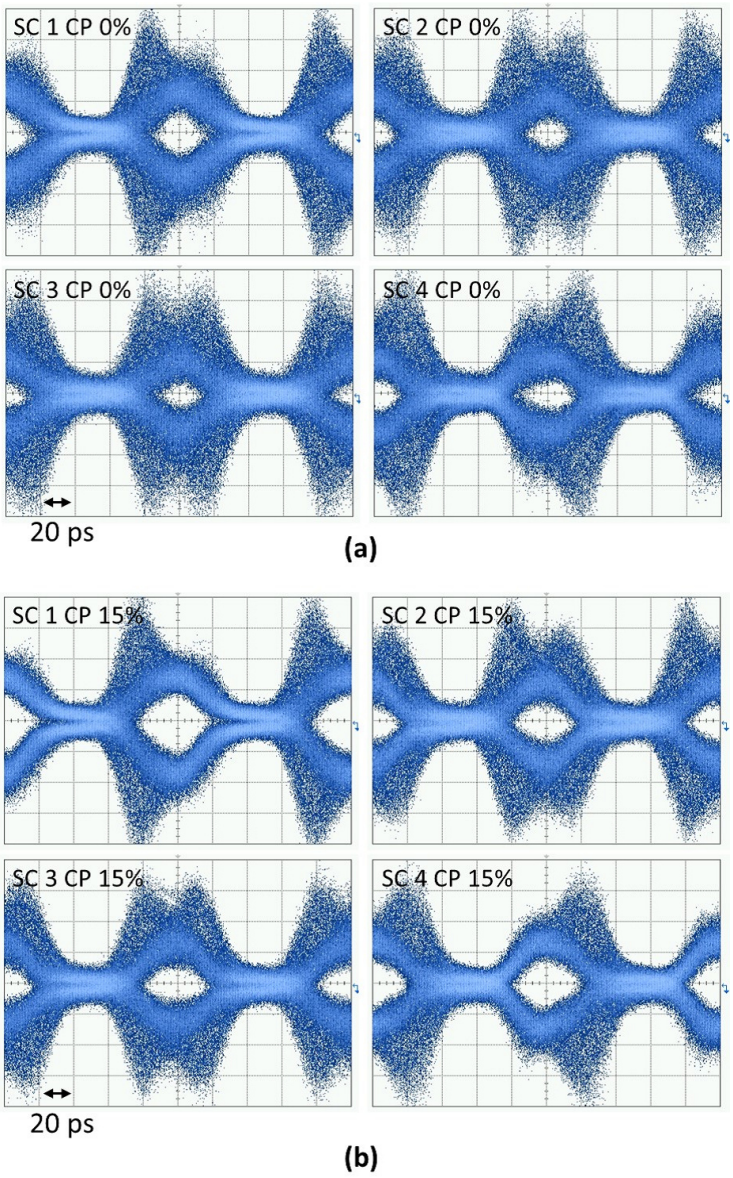

Figure 3.6: Experimental results for the eye diagrams of the four received subcarriers after the time gate and demodulation: (a) without a CP, (b) with a CP of 15%.

implemented by a WSS with spatial filters obtained by the Fourier transform in Eq. (14). Figure 3.5 shows the installed spatial filters with and without the CP. Although the spectra of each channel with and without the CP were the same, the interval of each channel was wider with the CP than without CP. A 10 GHz mode locked laser diode (MLLD) emitted a 1.5 ps pulse at 1550 nm. The pulse train was modulated by a 10 Gbit/s pseudo random bit sequence (PRBS) with differential binary phase shift keying (DBPSK). The modulated signal was split into four signals, and different delays were applied by optical delay lines (ODLs) to synchronize them with pattern decorrelation.

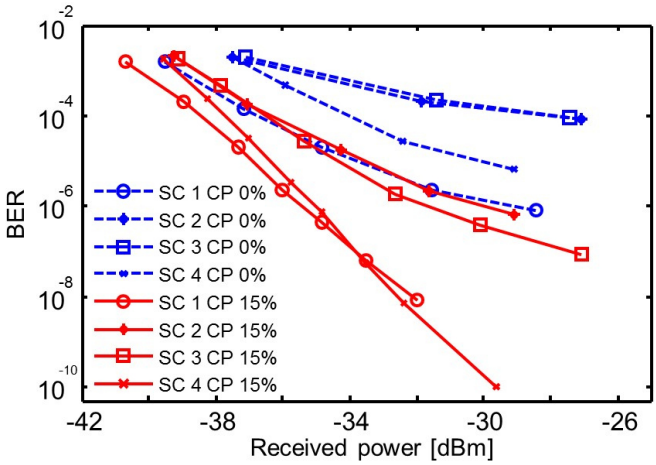

Figure 3.7: Experimental results for the BER performance as a function of the received power without and with a CP.

The four signals were fed to the input ports of the 4×1 WSS (Finisar 4000S) at the transmitter, which generated a 40 Gbit/s fractional OFDM signal. The polarizations of each port were aligned by a polarizer and polarization controllers (PCs). At the receiver, we used another 1×1 WSS (Finisar 1000S) and changed the corresponding installed filter to receive the four subcarriers. To demonstrate the effect of inserting a CP, we used the lithium niobate intensity modulator (LN-IM) time gate. Since the gate width was several tens of picoseconds, the detected signal is a summation of results extracted at various timing, thus ICI and ISI could be induced. A 1-bit delay line and 40 GHz balanced photo detector (BPD) demodulated the time-gated signals. Fig. 3.6 shows the eye diagrams of the four received subcarriers after the time gate and the demodulation with and without the CP. The eye diagrams are clearly larger with the CP than without the CP. Figure 3.7 shows the relationship between the BER and received power. The BER performed better with the CP than without the CP. These results indicate that the CP can reduce the ICI even if the performance of the time gate is insufficient.

3.4 Discussion

In order to quantify the effect of CP insertion, we evaluated the performance of the all-optical fractional OFDM transmitter and receiver in a simulation. For simplicity, we ignored noises such as shot noise and signal spontaneous beat noise and considered

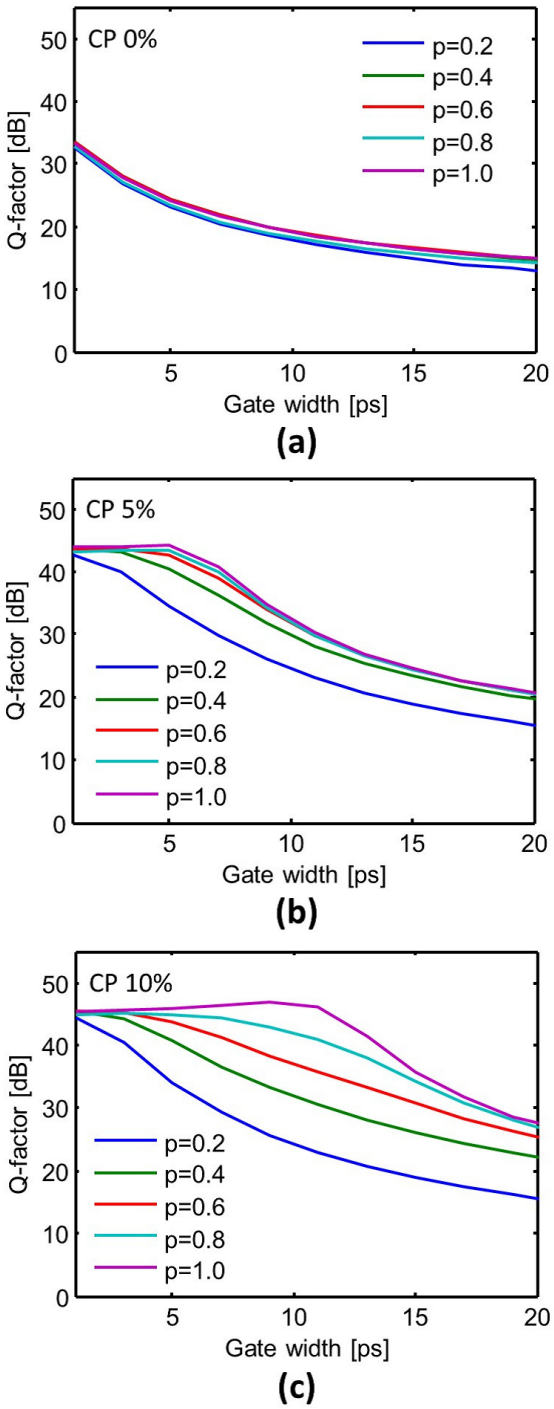

Figure 3.8: Relationship between the Q-factor and gate width of the time gate: (a) without a CP, (b) with a CP of 5%, and (c) with a CP of 10%.

only the ICI. The number of channels was 12. Each subcarrier was modulated in the QPSK format at a speed of 10 GHz. The demultiplexed signal was detected by coherent receivers with a 50 GHz electrical bandwidth. The performance of the detected signal

was evaluated according to the Q-factor of the electrical signals after the coherent receiver. Figure 3.8(a) shows the relationship between the Q-factor and gate width of the time gate without the CP. The Q-factor decreased depending on the gate width, and there was not a great difference according to the parameter p. With the CP, the Q-factor was significantly improved at any p, as shown in Figs. 3.8(b) and (c). When p was close to 1, the high signal quality was kept by using a wide time gate because the orthogonal position was wide. Inserting a large CP allowed the use of a wide time gate. However, further CP insertion may decrease the spectral efficiency. Reducing the parameter p decreased the effect of the CP.

3.5 Conclusion

In this chapter, to confirm that the FrFT can generalize the FT with keeping original useful functions in the Fourier transform, a verification of CP insertion for all-optical fractional OFDM was presented. We experimentally demonstrated the insertion of a CP in a four-channel 40 Gbit/s all-optical fractional OFDM signal. The measured BER showed that the CP improves the signal quality even if the performance of the time gate is insufficient. The relationship between the fractional parameter and the effect of CP insertion was investigated in simulation. In conjunction with nonlinearity mitigation presented in Chapter 2, all-optical fractional OFDM could mitigate the degradation of the signal quality due to nonlinear and linear impairments by optimizing the fractional parameter in accordance with the characteristic of fibers and the performance of system components.

Chapter 4

Experimental demonstration for practical use of all-optical fractional OFDM

In Chapter 2 and 3, a performance maximization of a transmission system by optimizing an optical signal multiplexing by FrFT was describes. In order to apply optimized transmission system in an actual system, it is indispensable to demonstrate the feasibility of devices and subsystems of the system. In this chapter, experimental demonstrations of feasibilities of implementation of all-optical fractional OFDM for practical use are presented. Firstly, to guarantee the operation in an actual network, the field trial in JGN-X which is an optical network testbed laid between NICT (at Koganei) and KDDI (at Ohtemachi) is demonstrated. Secondly, to reduce the cost of introducing the system, the feasibility of a cost effective all-optical fractional OFDM receiver using a planar lightwave circuit is demonstrated. Thirdly, to extend a flexibility of the signal handling method, a demultiplexing of an optical fractional OFDM signal by a time-lens effect is demonstrated.

4.1 Field trial in JGN-X

4.1.1 Introduction

In many cases, transmission experiments are demonstrated in laboratories. Because a fluctuation of temperature and vibration in a laboratory is small, the influence to optical signals in transmission fiber is supposed to be static. On the other hand, a transmission fiber in an actual network is exposed to a fluctuation of temperature and vibration. The optical signal is influenced by those factors. Therefore, it is desirable

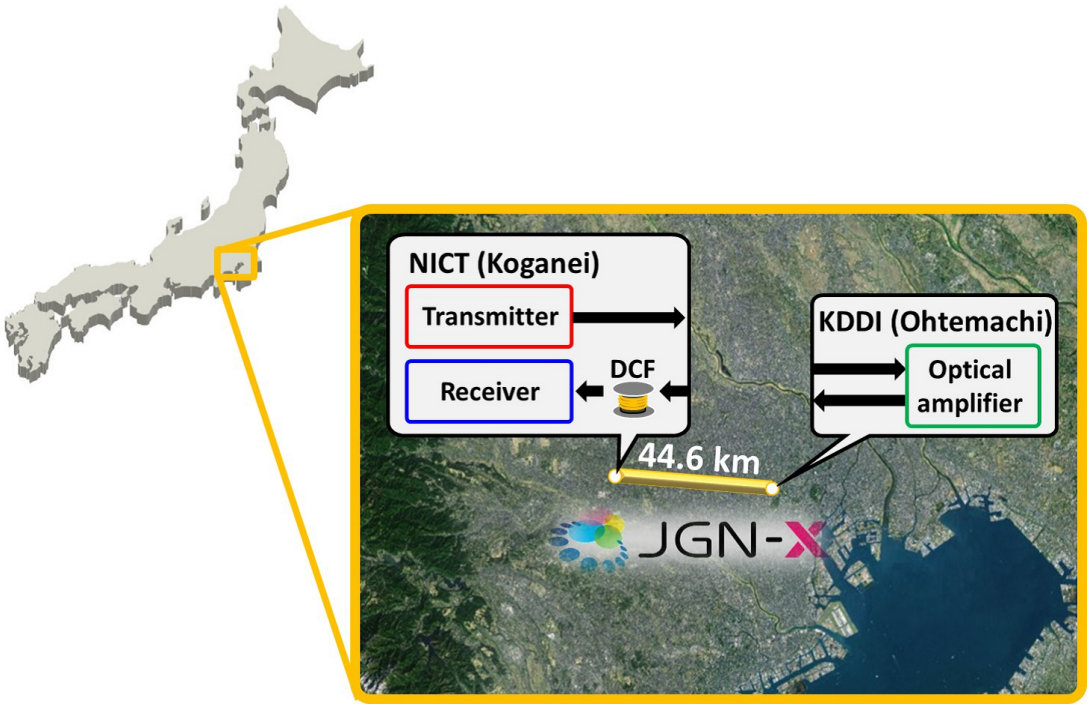

Figure 4.1: JGN-X.

that the transmission experiment should be performed in an actual environment. In this section, the field trial is demonstrated in an optical testbed of the Japan Gigabit Network eXtreme (JGN-X). JGN-X is operated by the National Institute of Communication and Information Technology (NICT) as an ultrahigh-speed testbed network for R&D collaboration between industry, academia, and government.[111] The optical fiber is installed between the NICT (at Koganei) and KDDI (at Ohtemachi) as shown in Fig. 4.1. The fiber length is 44.6 km (round trip is 89.2 km). Because the fiber specification is comply with ITU-T G.652 requirements, it provides an experiment environment close to an actual use environment for the feasibility experiments of an optical communication.

4.1.2 Experimental demonstration in JGN-X

The experimental setup is shown in Fig. 4.2. The transmitter and the receiver was set in NICT at Koganei. We set $p = -0.5$ at the transmitter and $p = 0.5$ at the receiver. A WSS implemented the filters of all-optical FrFT and multiplexed four channels which were modulated by 10 Gbit/s DBPSK. The 40 Gbit/s fractional OFDM signal trasmited though JGN-X. An EDFA in KDDI building at Ohtemachi amplified

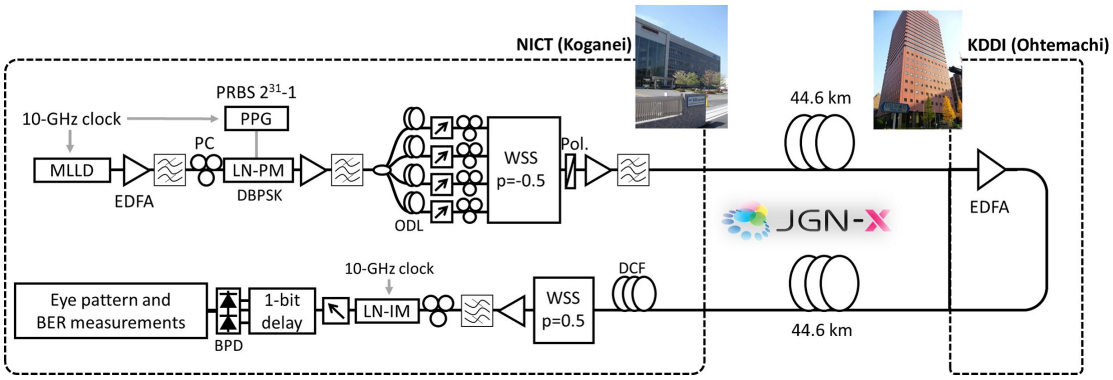

Figure 4.2: Experimental setup of the field trial in JGN-X.

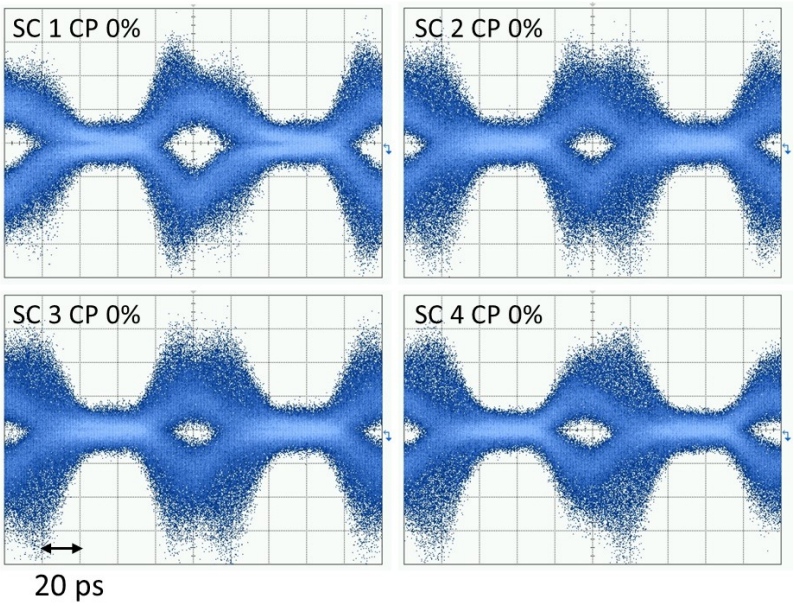

Figure 4.3: Experimental results for the eye diagrams of the four received subcarriers.

the transmitted signal and the signal returned to Koganei. A DCF compensated the chromatic dispersion before the receiver. Another WSS and LN-IM time gate demultiplexed the received signal to four subcarriers. Figure 4.3 shows the eye diagrams of the four received subcarriers, and a clear eye opening is observed. Figure 4.4 shows the relationship between the BER and received power, which is below the forward error correction (FEC) limit (2×10^{-3}). Under this error rate, the transmission could be regarded as error free.

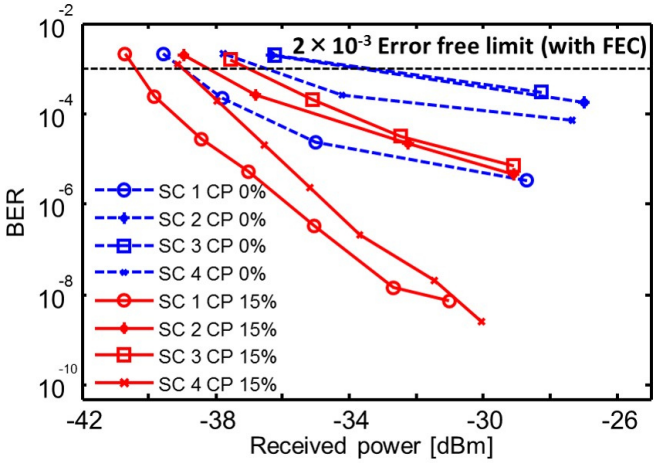

Figure 4.4: Experimental results for the BER performance as a function of the received power.

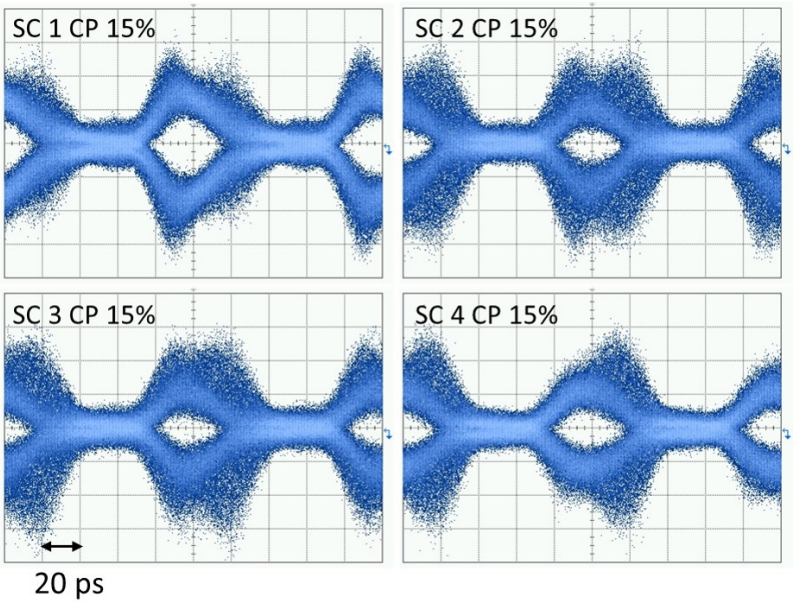

Figure 4.5: Experimental results for the eye diagrams of the four received subcarriers with cyclic prefix.

4.1.3 Performance improvement by cyclic prefix insertion

The eye opening and BER is worse than the back-to-back results demonstrated in Chapter 3 due to the residual dispersion. We tried to improve the received signal quality by cyclic prefix insertion. The insertion ratio was 15%. Figure 4.5 shows the eye diagrams which has a more clear eye opening. The BER is largely improved compared with the no insertion result. Therefore, the effectiveness of cyclic prefix insertion in an actual environment was also demonstrated.

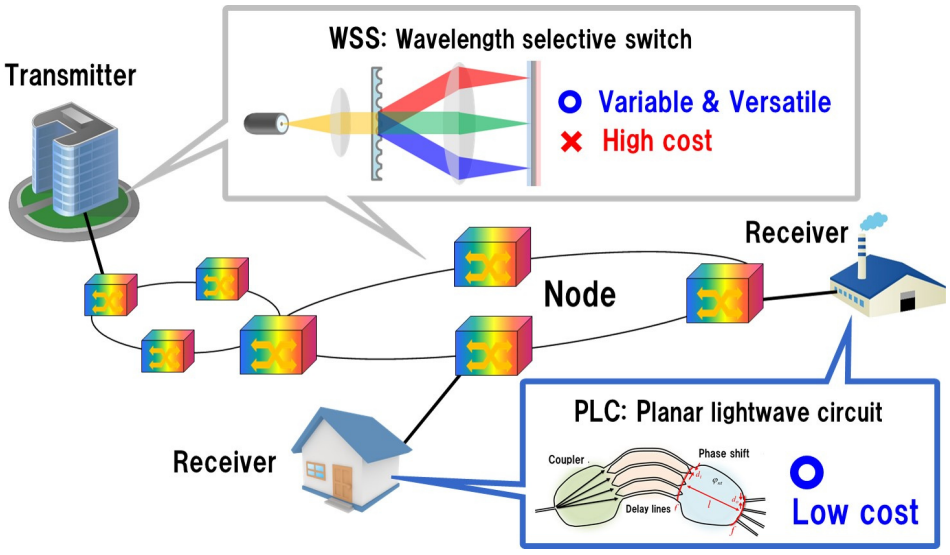

Figure 4.6: All-optical fractional OFDM system using WSS and PLC.

4.2 Cost effective all-optical fractional OFDM receiver using planar lightwave circuit

4.2.1 Introduction

The above experimental demonstrations used the WSS for the implementation of all-optical FrFT. Given that the software-defined networks presently being considered transmit different signals in various directions, the transmission conditions should be flexibly adjustable at all times.[112] Therefore, WSSs—which could implement reconfigurable filter functions in the frequency domain—should be used in the optical line terminals and nodes in optical networks as shown in Fig. 4.6. However, WSSs require large installation spaces and high manufacturing costs. On the other hand, planar lightwave circuits (PLC) could be mass-produced and reduce system cost and complexity, although with a fixed modulation bandwidth and function set. Because user-side optical network units often require a low cost, integrated waveguide devices are attractive for cost reduction.[113,114] In this section, we present a cost effective fractional OFDM receiver using a PLC, in combination with a flexible WSS based transmitter.

4.2.2 Implementation of all-optical fractional Fourier transform using planar lightwave circuit

Implementation of the FrFT by an PLC—by modifying the second slab coupler from a conventional DFT PLC, as shown in Fig. 4.7—has also been already proposed.[115] The

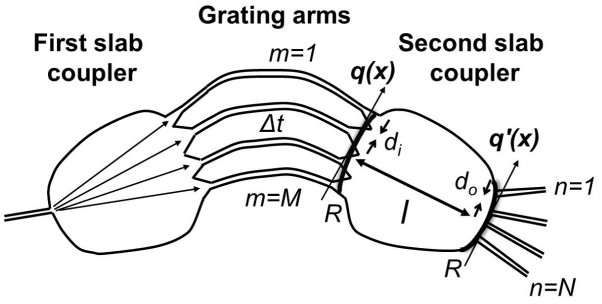

Figure 4.7: Configuration of the FrFT PLC.

first slab coupler splits the input pulse and the grating arms work as delay line. The second slab coupler gives the appropriate phase shift. The relation between the input $q(x)$ and output $q'(x)$ fields in the second slab coupler is dictated by Fresnel diffraction.

$$q(x) = \frac{e^{j2\pi l/\lambda}}{\sqrt{j\lambda l}} \int q'(x') e^{j\frac{\pi}{\lambda}\left[\left(x^2+x'^2\right)\left(\frac{1}{l}-\frac{1}{R}\right)-\frac{2xx'}{l}\right]} dx', \tag{4.1}$$

where l is the distance between the two surfaces and R their curvature radius. When the PLC parameters satisfy the relations $l = R$, $M = N$, $N = \lambda\bar{d}/d_i d_o$, and $\Delta t = 1/FSR$, where $\bar{d}$ is a real-valued scale parameter with dimensions of length, d_i the input waveguide pitch, d_o the output waveguide pitch, M the number of grating arms, N the number of output ports, and FSR the free spectral range, the discretized output field is

$$q'\left(\frac{nd_o}{\sqrt{\lambda\bar{d}}}\right) = B_1 \sum_{m=1}^{M} q\left(\frac{md_i}{\sqrt{\lambda\bar{d}}}\right) \cdot e^{j\pi\frac{2mn}{N}} \tag{4.2}$$

$$B_1 = e^{j\left(\frac{2nl}{\lambda}-\frac{\pi}{4}\right)}. \tag{4.3}$$

This PLC performs the DFT operation for comventional OFDM. The FrFT PLC parameters satisfy the relations $l = \bar{d}sin(p\pi/2)$, $R = \bar{d}cot(p\pi/4)$, $M = N$, $\Delta t = 1/FSR$, $d_i = \sqrt{\lambda\bar{d}}/N$, and $d_o = \sqrt{\lambda\bar{d}}sin(p\pi/2)$. The discretized output field is

$$q'\left(\frac{nd_o}{\sqrt{\lambda\bar{d}}}\right) = B_p \sum_{m=1}^{M} q\left(\frac{md_i}{\sqrt{\lambda\bar{d}}}\right) \cdot e^{j\pi\left\{\left[n^2 sin^2\left(p\frac{\pi}{2}\right)+\frac{m^2}{N^2}\right]\cot\left(p\frac{\pi}{2}\right)-\frac{2mn}{N}\right\}} \tag{4.4}$$

$$B_p = e^{j\frac{2nl}{\lambda}} \left|sin\left(p\frac{\pi}{2}\right)\right|^{-\frac{1}{2}} e^{-j\frac{\pi}{4}sign[sin(p\pi/2)]}. \tag{4.5}$$

The channel spacing is FSR/N as in conventional OFDM.

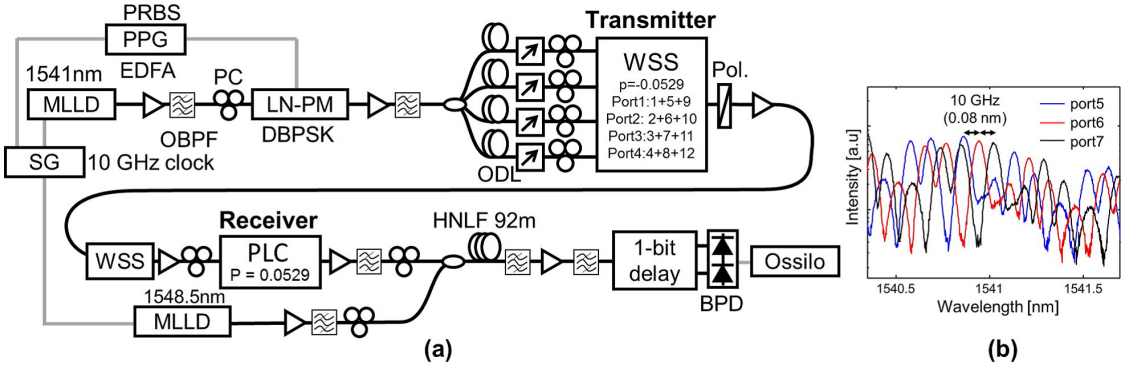

Figure 4.8: (a) Experimental setup. (b) Transfer functions of the fabricated FrFT PLC at ports 5, 6, and 7.

Figure 4.9: Fabricated FrFT PLC.

4.2.3 Experimental demonstration

Figure 4.8(a) shows the experimental setup for a combined WSS-PLC fractional OFDM system. We used $p = -0.0529$ at the transmitter (where the FrFT is implemented using a WSS) and $p = 0.0529$ at the receiver (where the FrFT is implemented using an PLC). The fabricated FrFT PLC parameters were: $N = 12$ ports, $FSR = 120$ GHz, $l = 10.1$ mm, $R = 2.92$ m, $d_i = 30.0$ μ m and $d_o = 29.8$ μ m. Figure 4.8(b) shows transmission spectra at ports 5, 6, and 7. Even though the spectra of individual subcarriers in the fractional OFDM signal are broader than the corresponding conventional OFDM signal spectra, the interval of each subcarrier is equal to that of conventional OFDM. Figure 4.9 shows the appearance of the fabricated FrFT PLC. Given that the used WSS (Finisar 4000S) has only four ports, SC1-5-9, SC2-6-10, SC3-7-11, and SC4-8-12 transmitted the same data. A 10 GHz MLLD emitted 1.5 ps pulses at 1541 nm. The

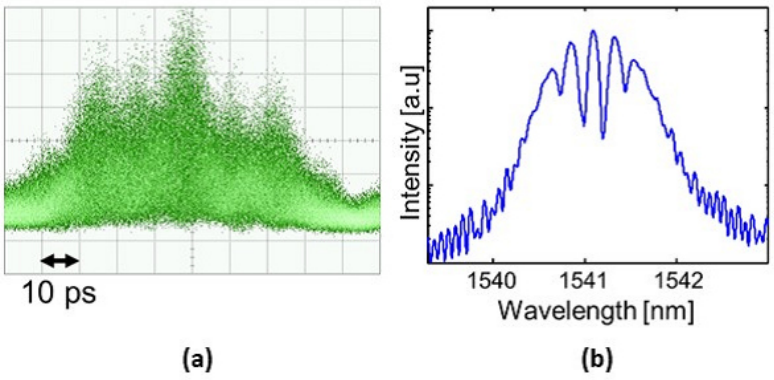

Figure 4.10: (a) Multiplexed signal waveform. (b) Multiplexed signal spectrum.

pulse train was modulated by a 10 Gbit/s PRBS with DBPSK. The modulated signal was split into four signals, and different delays were applied—by optical delay lines—to synchronize them with the decorrelation pattern. The four signals were then fed to the input ports of the 4 × 1 WSS at the transmitter, which generates a 120 Gbit/s fractional OFDM signal. The polarizations of the individual ports were aligned with a polarizer and polarization controllers. The multiplexed signal appears random in shape, as shown in Fig. 4.10(a); its spectrum is shown in Fig. 4.10(b). An additional WSS was used as a compensation filter, because the MLLD output had some chirping behavior. In general, the system does not require the additional WSS. Figure 4.11(a, b) shows the output signals of the FrFT PLC at ports 5 and 6. It was confirmed that open eyes were obtained for the signals. A 1.5 ps four-wave mixing based optical time gate using another MLLD, a highly nonlinear fiber (HNLF), and an optical bandpass filter (OBPF) were used to sample the output signals. In this experiment, we used the same clock at both transmitter and receiver. In practical situations, clock recovery should be used for synchronization. Figure 4.12 shows the four-wave mixing results. The conversion efficiency was -24 dB. A 1-bit delay line and a balanced photodetector demodulated the sampled signal. The detected waveform was averaged, because of the oscilloscope large timing jitter. The eye diagrams at port 5 and port 6 were clearly open, as shown in Figs. 4.13(a, b).

4.2.4 Discussion

Although we tried to measure the bit error rate to evaluate the system performance, the signal to noise ratio of the recovered signal was not enough. The degradation of

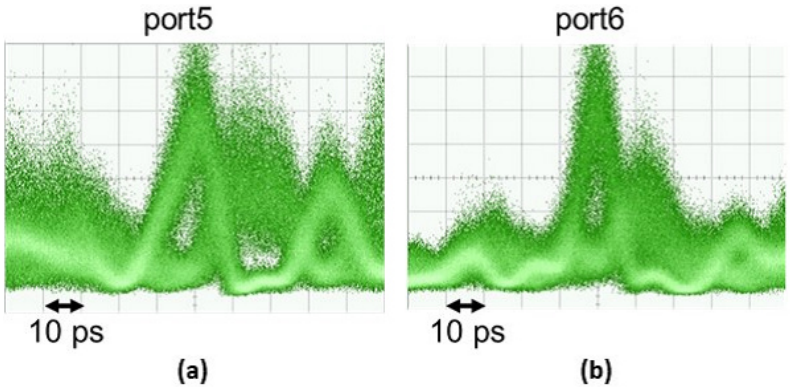

Figure 4.11: Output signals of the FrFT PLC at (a) port 5 and (b) port 6.

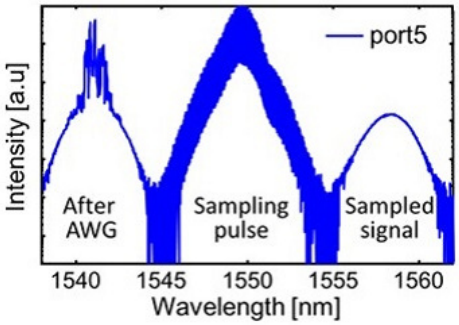

Figure 4.12: Four wave mixing result.

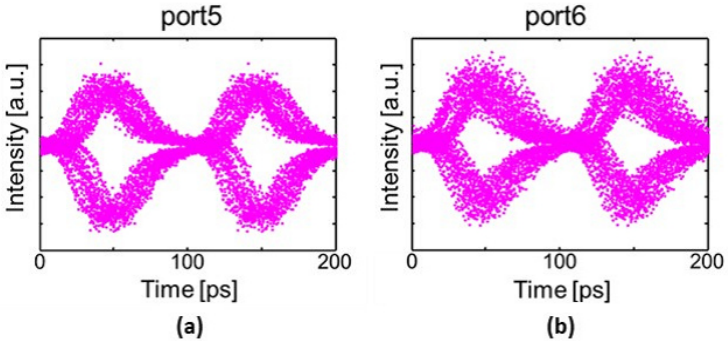

Figure 4.13: Eye diagrams of the demodulated signals at (a) port 5, and (b) port 6.

the signal quality may be caused by a p parameter mismatch between transmitter and receiver. In our experiment, we obtained the value of p of the fabricated FrFT PLC by the relationship between the p parameter and dispersion value for the pulsing of the FrFT signal. However, it is difficult to obtain the accurate value of p because the pulsed shapes with correct dispersion and slight difference dispersion are very similar. In a practical situation, a p parameter mismatch might be occurred by some errors of

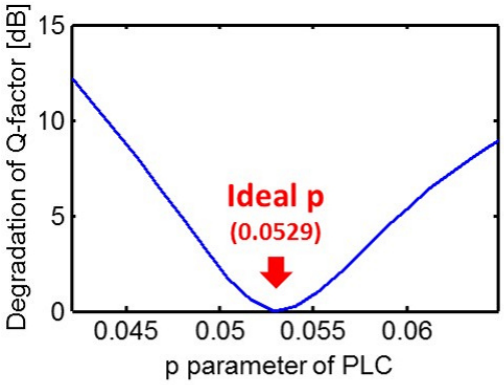

Figure 4.14: Relationship between the value of p of FrFT PLC and the degradation of Q-factor from the ideal value (p=0.0529).

system conditions or device fabrication. Therefore, we investigated the performance degradation by p parameter mismatch in a simulation. The system condition was the same as the experiment. We used $p = -0.0529$ at the transmitter and changed the value of p of FrFT PLC at the receiver. The quality of the recovered signal was evaluated by the Q-factor. Figure 4.14 shows the relationship between the value of p of FrFT PLC and the degradation of Q-factor from the ideal value ($p = 0.0529$). When the p parameter mismatch was 0.005 ($p = 0.0479$), the Q-factor was significantly degraded and the penalty was 5 dB. To keep the degradation of Q-factor under 1 dB, the p parameter mismatch should be suppressed under 0.0017.

4.3 Demultiplexing of optical fractional OFDM signal by time-lens effect

4.3.1 Introduction

In the receiver side, the optical fractional OFDM signal is demultiplexed by fractional Fourier transform with inverse p parameter. On the other hand, we discussed that the optical fractional OFDM signal is converted to Nyquist pulse train through the time-lens by the chromatic dispersion, as shown in Fig. 4.15. Thus, it is indicated that the converted signal could be treated like a N-OTDM signal. Since the N-OTDM signal could be demultiplexed using ultra-fast time gate, the demultiplexing of the converted signal is achieved without the fractional Fourier transform.

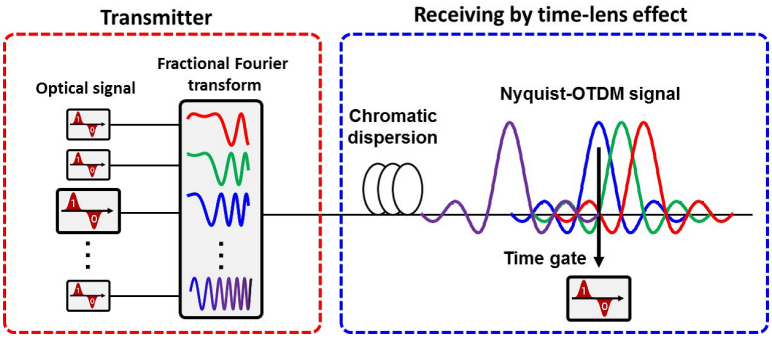

Figure 4.15: Receiving by time-lens effect.

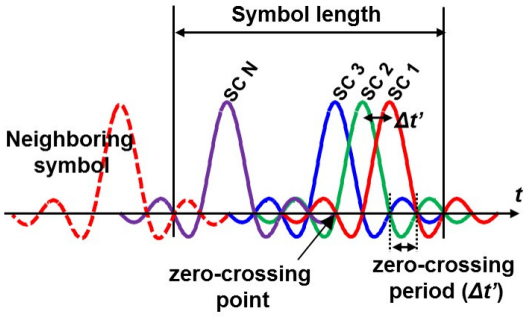

Figure 4.16: Generated sinc pulses.

4.3.2 N-OTDM conversion by time-lens effect

The dispersion for time-lens effect is discribed by

$$D = -cT^2 tan\left(p\pi/2\right)/\lambda^2, \tag{4.6}$$

where c is the speed of light and λ is the central wavelength. Sinc pulses are generated, as discribed by

$$\begin{aligned} \phi_n^p(t) \otimes e^{j\frac{\pi c}{\lambda^2 D}t^2} &= C \cdot e^{-j\pi\frac{cot\left(p\frac{\pi}{2}\right)}{T^2}\cdot t^2} \cdot \mathcal{F}\left\{\phi_n^1(\tau)\right\} \\ &= C \cdot e^{-j\pi\frac{cot\left(p\frac{\pi}{2}\right)}{T^2}\cdot t^2} \cdot sinc\left(\frac{t}{\Delta t'} + n\Delta t'\right), \end{aligned} \tag{4.7}$$

where

$$\Delta t' = Ttan(p\pi/2) \tag{4.8}$$

is the interval of each subcarrier. The interval is set equal to the zero-crossing period in the oscillating tail. Even if neighboring pulses overlap, no ICI occurs at any symbol point, as shown in Fig. 4.16. When the number of subcarrier is N, the Nth subcarrier delays $N\Delta t'$ compared with the 1st subcarrier. If the timewidth exceeds the symbol

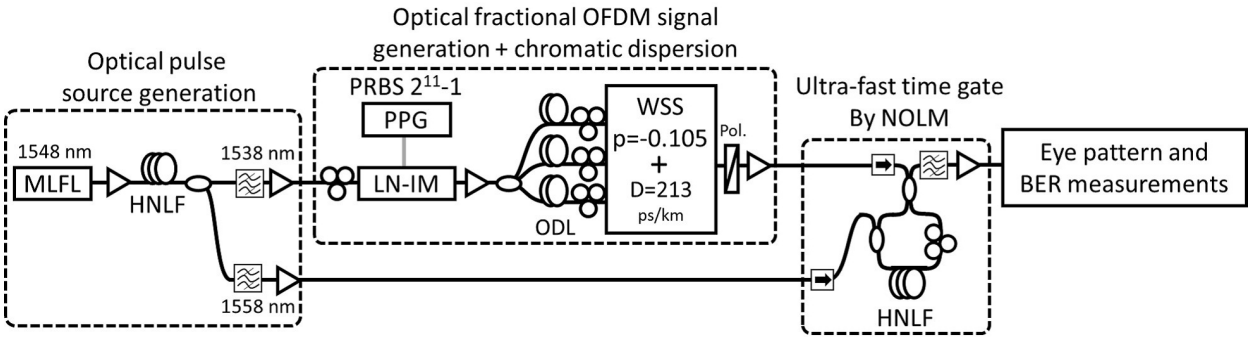

Figure 4.17: Experimental setup of the demultiplexing of the optical fractional OFDM signal by time-lens effect.

length, the signal is interferenced to neighboring symbols of other subcarriers. Thus, p is required to be

$$p = \frac{2}{\pi} tan^{-1}(1/N) \tag{4.9}$$

or lower. Moreover the zero-crossing period in the oscillating tail is required to be fit into the symbol length because the peak point of each sinc pulse should be set at the zero-crossing points of neighboring symbols. Therefore, p is required to be

$$p = \frac{2}{\pi} tan^{-1}(1/M) \tag{4.10}$$

where M is a positive integer of N or smaller. In this case, all subcarrier could be demultiplexed without ICI and ISI.

4.3.3 Experimental demonstration

Figure 4.17 shows the experimental setup. The optical pulse emitted by a 10 GHz mode locked fiber laser (MLFL) propagates a 400 m HNLF for self-phase modulation because two optical pulse sources were required for the experiment, as shown in Fig. 4.18. The signal pulse filtered at 1538 nm was modulated by 10 Gbit/s OOK signal. The number of subcarrier is 3. The fractional Fourier transform was implemented by WSS. The p parameter was -0.105. The waveform of each subcarrier is spread in the symbol length as shown in Fig. 4.19. The eye diagram of the multiplexed signal appears random in shape. The dispersion corresponding to the p is 213 nm/km. In this experiment, the dispersion was implemented in WSS. Figure 4.20 shows the eye diagram of each subcarrier with the dispersion. The signal was converted to sinc pulse

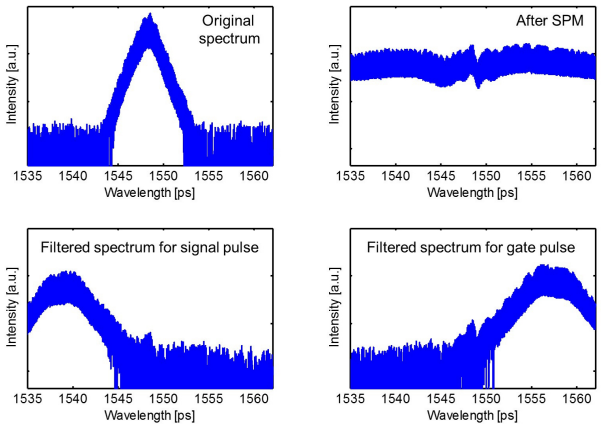

Figure 4.18: Spectra of optical pulse source generation.

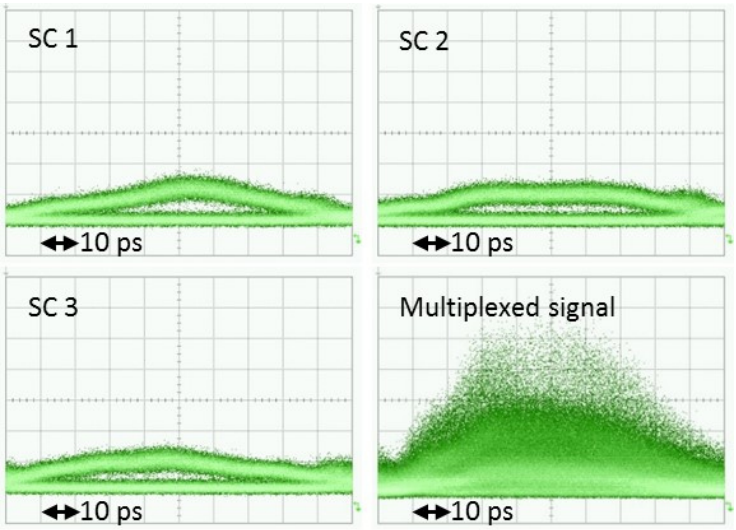

Figure 4.19: Waveform of each subcarrier before chromatic dispersion.

and delayed 16 ps from the neighboring subcarrier. This result agrees the eq. (4.6). There were three open eyes in the multiplexed signal because no ICI and ISI occured at each peak point. A ultra-fast time gate by nonlinear loop mirror (NOLM) performed the demultiplexing of the optical fractional OFDM signal. A 1 ps optical pulse filtered at 1558 nm was used as the gate pulse. Figure 4.21 shows the open eye of the eye diagram of each demultiplexed subcarrier. Figure 4.22 shows the BER measured as a function of the recived power, wicth is largely below the FEC limit.

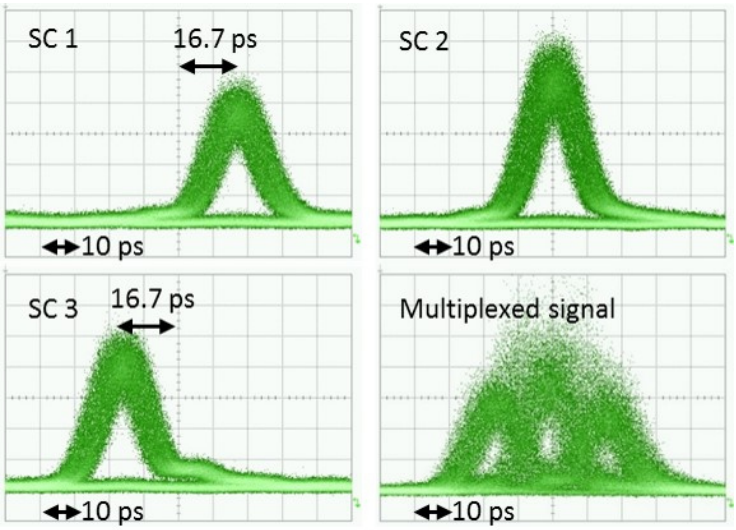

Figure 4.20: Waveform of each subcarrier after chromatic dispersion.

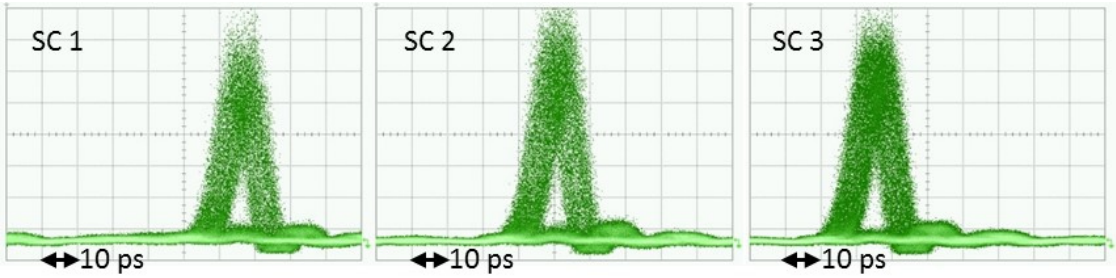

Figure 4.21: Waveform of each subcarrier before ultra-fast time gating.

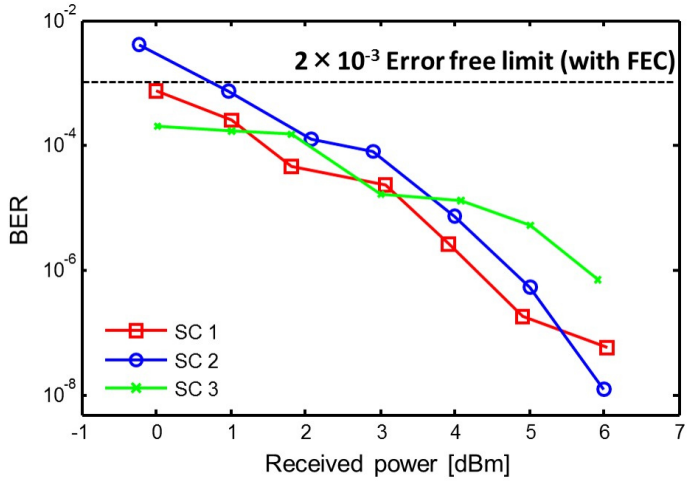

Figure 4.22: Experimental results for the BER performance as a function of the received power.

4.4 Conclusion

In this chapter, we experimentally demonstrated the feasibility of the all-optical fractional OFDM system in a practical network system. Firstly, to guarantee the operation

in an actual network, the field trial in JGN-X was successfully demonstrated. The 40 Gbit/s optical fractional OFDM signal could be demultiplexed after the 89.2-km transmission. If there are ICI due to residual dispersion or insufficient timegates, the cyclic prefix insertion mitigates the degradation of the signal quality. Secondly, the WSS-based multiplexing and PLC-based demultiplexing of a 12×10 Gbit/s DBPSK optical fractional OFDM signal were experimentally demonstrated. This combination has advantages both in terms of network architecture flexibility, and in the reduction of system cost and complexity. Thirdly, the demultiplexing of optical fractional OFDM signal by time-lens effect was demonstrated. Treating the optical fractional OFDM signal like a N-OTDM signal, the signal is demultiplexed by an ultra-fast time gate without the fractional Fourier transform. From these experiments, the feasibility of the all-optical fractional OFDM system was demonstrated. These demonstrations in an optical communication field could ensure a reliability of the optical signal multiplexing based on FrFT in wide fields.

Chapter 5

Experimental demonstration of feasibility of all-optical analog-to-digital conversion for optical fractional OFDM signal

In this chapter, the necessity and issue on all-optical ADC are experimentally examined to cope with an optical fractional OFDM. Firstly, the motivation of an optical approach for ADC and principle of all-optical ADC are stated. To demonstrate the feasibility of all-optical ADC for a received optical fractional OFDM signal, the experimental demonstration of a demodulation of 4-ASK optical fractional OFDM signal using 2 bit all-optical ADC is presented.

5.1 Introduction

In Chapter 2 and 3, it is indicated that all-optical fractional OFDM mitigates the degradation of the signal quality due to nonlinear and linear impairments by optimizing the fractional parameter p in accordance with the characteristic of fibers and the performance of system components. If the signal quality is improved, a multilevel modulation with high multiplicity is available. The optical signal in the fiber is an analog signal. Generally, to demultiplex a multilevel signal including many binary signals, a signal level is distinguished after converting it to a digital signal. To treat a high multiplicity multilevel modulation at high symbol rate, high resolution and high sampling rate ADC is required. However, a performance of the conventional electrical ADC is limited by the jitter of the sampling aperture.[42] Since the jitter of the sampling aper-

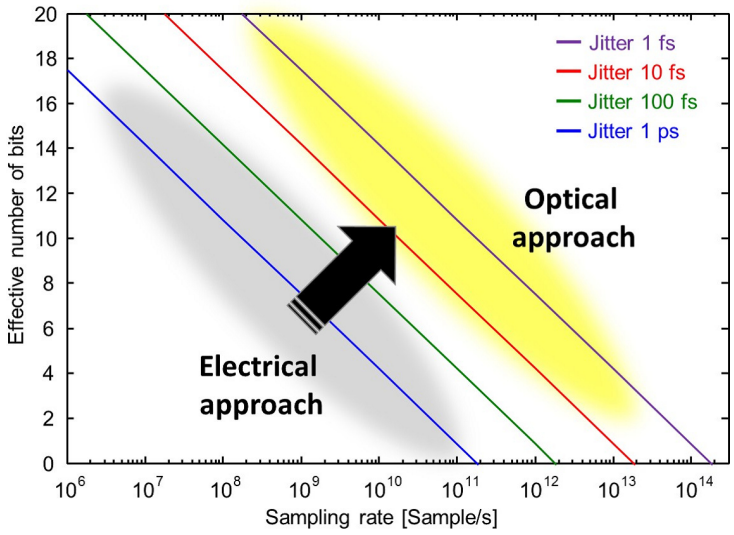

Figure 5.1: Trade off between sampling rate and resolution due to jitter.

ture affects the accuracy of high frequency input signals, there is a trade off between sampling rate and resolution, as shown in Fig. 5.1. The relationship between the jitter and the achievable maximum effective number of bits (ENOB) is calculated as,

$$ENOB_{jitter} = log_2\left(\frac{2}{\sqrt{3}\pi f_{samp}\tau}\right) - 1, \tag{5.1}$$

where τ is jitter and f_{samp} is sampling rate. In general, the lower limit of electrical jitter is estimated to 100 fs.[43] To overcome this limitation, optical approaches have recently attracted considerable attention. The mode locked laser, which provides an ultra-stable optical pulse stream, can offer a sampling aperture with ultra-low jitter, as low as a few femtoseconds.[44–49] An ADC consists of three parts: sampling, quantization, and coding. Optical sampling using optical pulse streams is a mature technique and has been used in high-performance ADCs using electrical quantization and coding processes. Because the optical approach is used for serial-to-parallel conversion in this type of photonic-assisted ADC, multiple electrical ADCs are used for bandwidth matching.[50–53] However, many electrical ADCs are required to support a high sampling rate, and therefore, increased energy consumption is unavoidable. Using optical technology for the entire process, including the subsequent quantization and coding, should reduce energy consumption. Several optical quantization and coding techniques have been proposed to achieve all-optical ADC designs.[54] In these proposals, the use of the nonlinear effects in a fiber is one promising approach because it has an ultrafast response speed and introduces various power-dependent phenomena

such as self-phase modulation, cross-phase modulation, and soliton self-frequency shift (SSFS).[55–58] Previously, our research group proposed an optical quantization method using intensity-to-wavelength conversion based on SSFS and various coding schemes to support the proposed optical quantization.[59–66,116] SSFS is energy-efficient compared with other nonlinear effects because it is self-acting, without the assistance of a pump pulse.

Since the proposed all-optical ADC performs a whole process from sampling to coding in a optical domain, a output is a optical signal. Although the converted signal could be performed the digital signal processing by electrical circuits after optical-electronic conversion, the converted signal could be directly processed in the optical domain. Recently, optical routing techniques have attracted much attention to reduce power consumption of the network routing system. Using the proposed all-optical ADC for demultiplexing of multilevel modulation, the multilevel signal could be routed without optical-electronic-optical conversion.

In this chapter, the receiving of optical fractional OFDM signal with multilevel modulation using all-optical ADC is presented and experimentally demonstrated.

5.2 Principle of all-optical analog-to-digital conversion

Figure 5.2 shows a conceptual diagram of our proposed all-optical ADC. An analog input signal is sampled by an optical pulse train using an established optical sampling process. The sampled pulses with different intensities are fed to an optical fiber and propagate as solitons with no pulse broadening owing to the balance between fiber dispersion and nonlinearity. At this point, the Raman effect moves the spectral energy of each sampled pulse to the longer or shorter wavelength side depending on its intensity. This phenomenon is called SSFS, the amount of wavelength shift is theoretically determined by the equation developed by the nonlinear Schrodinger equation,

$$\kappa(z) = -\frac{8}{15}\delta_R \eta^4 z, \tag{5.2}$$

where κ is the center frequency of a soliton pulse, z is the propagation distance in a HNLF, δ_R is the coefficient of the self-induced Raman effect, and η is the amplitude of an input pulse. Eq. (5.2) indicates that the center wavelength of an input pulse shifts

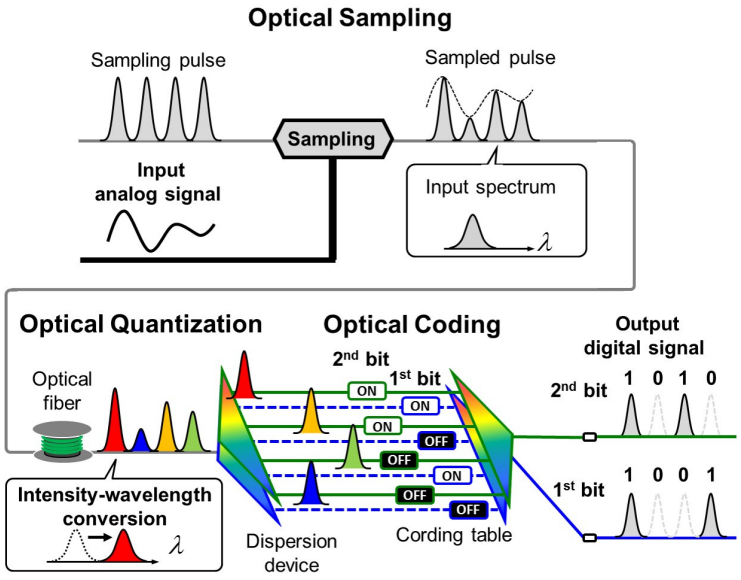

Figure 5.2: Schematic diagram of all-optical ADC.

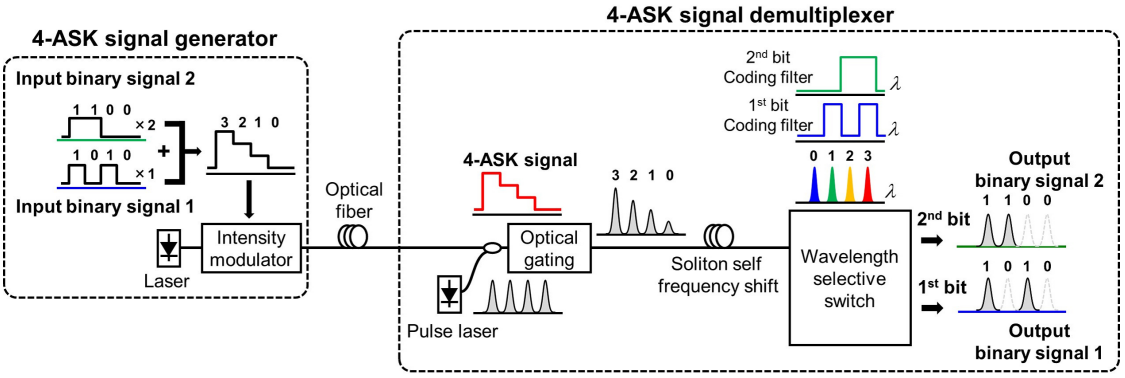

Figure 5.3: Schematic diagram of the demultiplexing multilevel ASK signal using all-optical ADC.

to longer wavelength side in proportion to the fourth power of the peak power of the input pulse. Because the intensity difference is converted into wavelength information, optical quantization is achieved by separating the wavelength using an appropriate dispersion device. For optical coding, each different wavelength port of the dispersion device is connected to each output port in accordance with an arbitrary coding table.

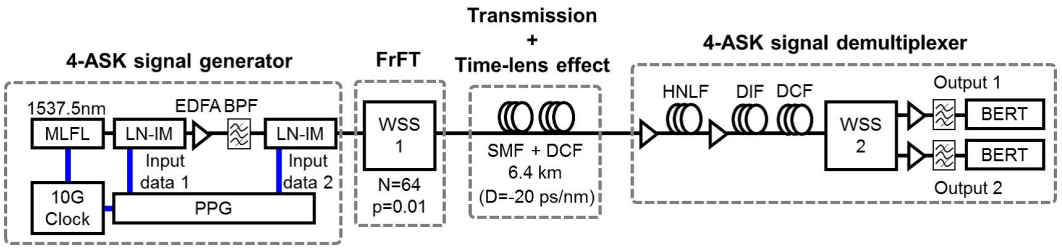

Figure 5.4: Experimental setup.

5.3 Demultiplexing of multilevel ASK signal using all-optical analog-to-digital conversion

Figure 5.3 shows the schematic diagram of the demultiplexing multilevel ASK signal using all-optical ADC[116] in the case of 4-ASK. A multilevel ASK signal is generated by combining N input binary signals. Each input binary signal di_k is applied a different weighting factor w_k and all of them are summed.

$$s = \sum_{k=1}^{N} w_k di_k, w_k = 2^{k-1}. \tag{5.3}$$

The generated multilevel signal s has 2^N levels. A multilevel ASK signal is sampled by an optical pulse train. The sampled pulses with different intensities are fed to an optical fiber for intensity-wavelength conversion by SSFS. Each pulse has the different wavelength depending on its intensity. For optical coding, each different wavelength pulse is connected to N bit output ports in accordance with a binary conversion table.

$$do_k = floor(s/w_k)\ mod\ 2, w_k = 2^{k-1}. \tag{5.4}$$

Since each output binary signal do_k is corresponding to the input binary signal di_k, the multilevel ASK signal could be demodulated by all-optical ADC without optical-electronic conversion.

5.4 Experimental demonstration of receiving of optical fractional OFDM signal using all-optical analog-to-digital conversion

Figure 5.4 shows the experimental setup for the all-optical demultiplexing of 4-ASK optical fractional OFDM signal using all-optical ADC. We used a MLFL as the optical

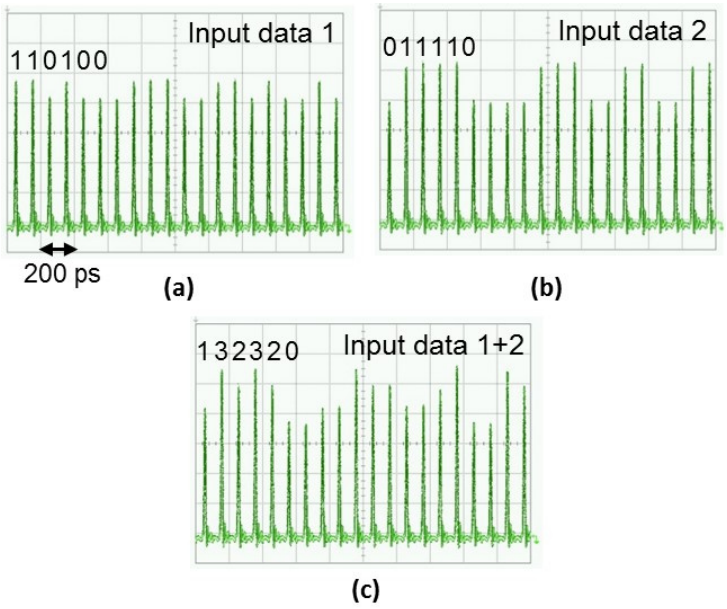

Figure 5.5: Waveform with only input data1, only input data2, and both input data1 and 2.

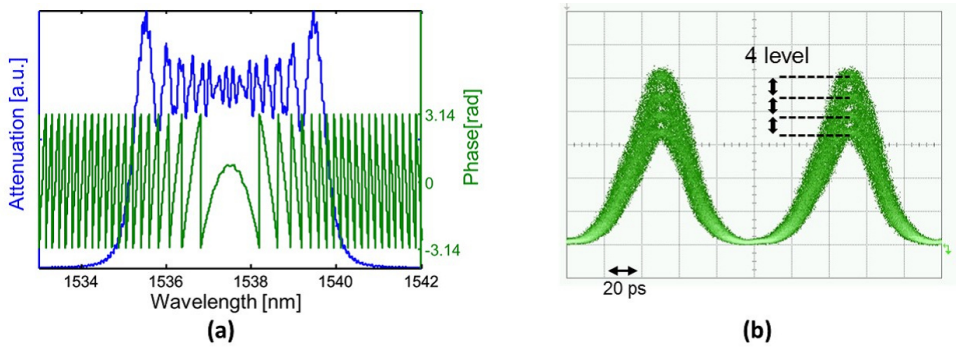

Figure 5.6: Filter function of FrFT.

pulse source. The center wavelength, repetition rate, and pulse width were 1537.5 nm, 10 GHz, and 1.3 ps, respectively. To generate a 4-ASK signal, the pulse train was modulated by two LN-IM with PRBS. Figure 5.5(a, b) shows the waveform with only input data 1 and only input data 2, respectively. The voltage of the input data 2 was twice than that of the input data 1. Figure 5.5(c) shows the waveform with both data 1 and data 2. The WSS 1 installed $p = 0.01$ FrFT filter which allows to pack 64 subcarriers within a symbol duration after Nyquist pulse conversion. Figure 5.6 shows the filter function and the eye diagram of the optical fractional OFDM signal. The optical fractional OFDM signal was transmitted through 6.4 km single mode fiber and dispersion compensation fiber link which has 20 ps/nm dispersion for

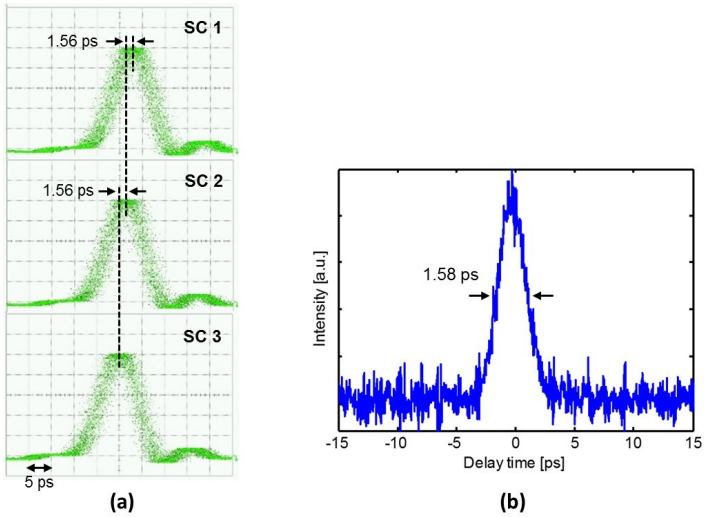

Figure 5.7: Temporal delay of each subcarrier.

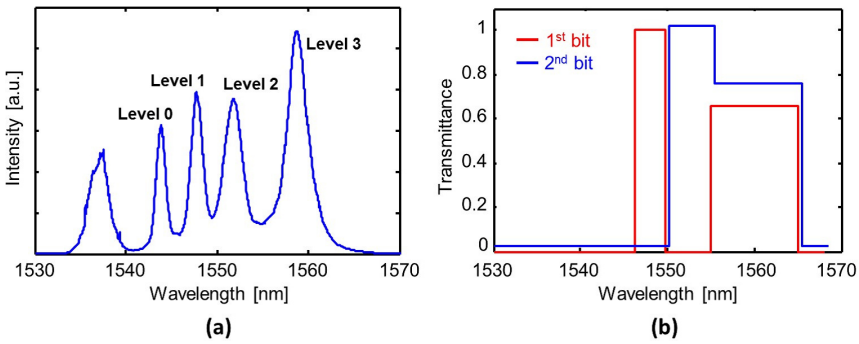

Figure 5.8: Output spectrum after intensity-to-wavelength conversion.

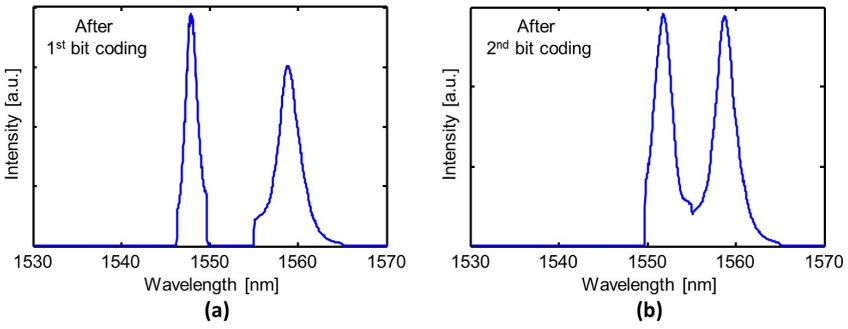

Figure 5.9: Installed 2-bit coding filter.

the time-lens effect. In this experiment, a time-gating module was not used because we transmitted only one subcarrier and changed the FrFT filter to separately transmit the other subcarriers. Figure 5.7 shows the temporal delay of each subcarrier measured

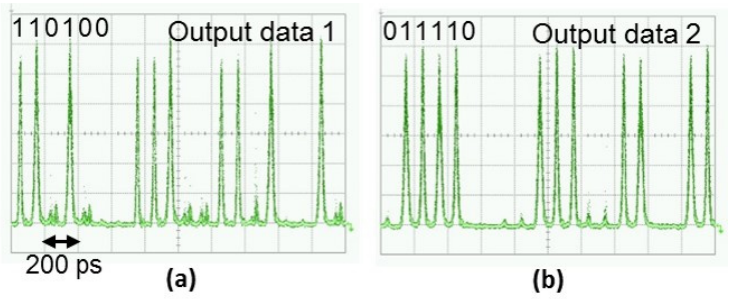

Figure 5.10: Temporal waveform of each output.

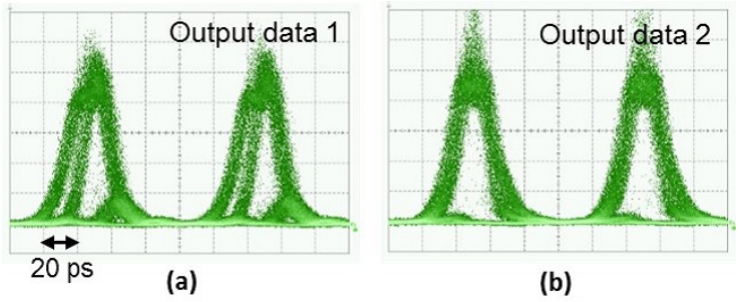

Figure 5.11: Eye diagram of each output.

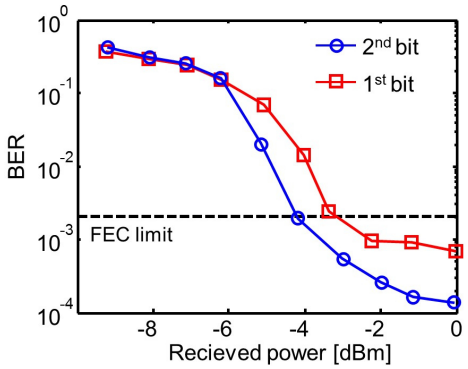

Figure 5.12: BER performance as a function of the received power.

by 50 GHz optical oscilloscope and the autocorrelation trace. Since the temporal delay and pulse width were 1.56 ps and 1.58 ps, the optical fractional OFDM signal was converted to the Nyquist pulse. The converted pulse was propagated in a 1 km HNLF (dispersion: D=7 ps/nm/km, dispersion slope: S=0.03 ps/nm2/km, nonlinearity: γ =15 /W/km) to induce SSFS, a 1 km dispersion increasing fiber (DIF) (D =0.0 to 15.0 ps/nm/km) to compress spectrum, and a 90 m DCF to adjust the group velocity walk-off effect by chromatic dispersion. Figure 5.8 shows the output spectrum after intensity-to-wavelength conversion. There were four peak spectra corresponding to

modulated four levels. Wavelength separation and coding processes were obtained by a 1×2 WSS 2. Figure 5.9 shows the installed 2-bit coding filters. To compensate for the output power, the attenuation on the longer wavelength side was higher than on the shorter wavelength side. Figure 5.10 shows the temporal waveform of each output signal from the WSS 2. The 4-ASK signal could be demodulated into two binary signals. The eye diagrams were clearly opened as shown in Fig. 5.11. To evaluate the system performance, we demonstrated the BER test as shown in figure 5.12. Both output binary signals below the FEC limit.

5.5 Conclusion

In this chapter, the necessity and issue on all-optical ADC were experimentally examined to cope with an optical fractional OFDM signal. All-optical ADC is expected to afford ultrawide broadband signals in the next generation of optical communication. To demonstrate the compatibility of all-optical ADC for a received optical fractional OFDM signal, the experimental demonstration of a demodulation of 4-ASK optical fractional OFDM signal using 2 bit all-optical ADC was presented. The demonstration was performed in low bit resolution to confirm a compatibility of all-optical ADC with a received optical fractional OFDM signal. Once the number of levels is upgraded, a high resolution all-optical ADC is required.

Chapter 6

Resolution improvement techniques of all-optical analog-to-digital conversion in practical limitations

In this chapter, resolution improvement techniques of all-optical ADC are proposed to treat the received signal with higher performance in practical limitations. Firstly, to cope with a imperfection of components in the all-optical ADC, a quantization error improvement technique is presented and experimentally demonstrated. Secondly, to overcome a limitation of a trade off between sampling rate and resolution, the sampling rate independent resolution upgrade is presented. Finally, the demonstration of 40 GS/s 4 bit all-optical ADC is presented.

6.1 Introduction

In optical communication, a high resolution and high sampling rate ADC is indispensable to improve spectral efficiency. The higher the resolution is, the higher multiplicity of multilevel modulation can be handled. ADC is a very important technology in all kinds of fields such as advanced radar systems, remote sensing, and realtime signal monitoring. Previously, our research group has proposed all-optical ADC based on intensity-to-wavelength conversion by soliton self frequency shift. Since the resolution of optical quantization strongly depends on the spectral width after SSFS, we tried to upgrade the resolution using a spectral compression technique and have demonstrated a 6 bit optical quantization.[117] Furthermore, a simulation result shows that the 7 bit resolution can be realized by using a phase modulator.[118] However, a further resolution upgrade is suppressed due to stagnations of wavelength shift at specific input peak

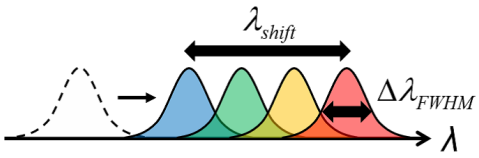

Figure 6.1: The resolution of optical quantization.

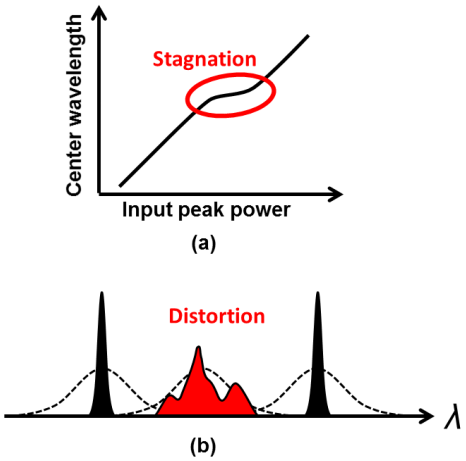

Figure 6.2: Stagnations of wavelength shift and distortions of spectral compression.

power regions and the pulse broadening by the spectral compression. In this chapter, the resolution improvement techniques of all-optical ADC are proposed. Firstly, the quantization error improvement is presented and experimentally demonstrated. Secondly, the sampling rate independent resolution upgrade is presented. Finally, the demonstration of 40 GS/s 4 bit all-optical ADC is presented.

6.2 Quantization error improvement for optical quantization using dual rail configuration

In this section, we propose a quantization error improvement technique using a dual rail configuration for high accuracy optical quantization and experimentally demonstrate an improvement of the evaluation figures of quantization error; differential nonlinearity (DNL), integral nonlinearity (INL), and ENOB. In addition, we examine the XPM influence between counter-propagating pulses at high sampling rate.

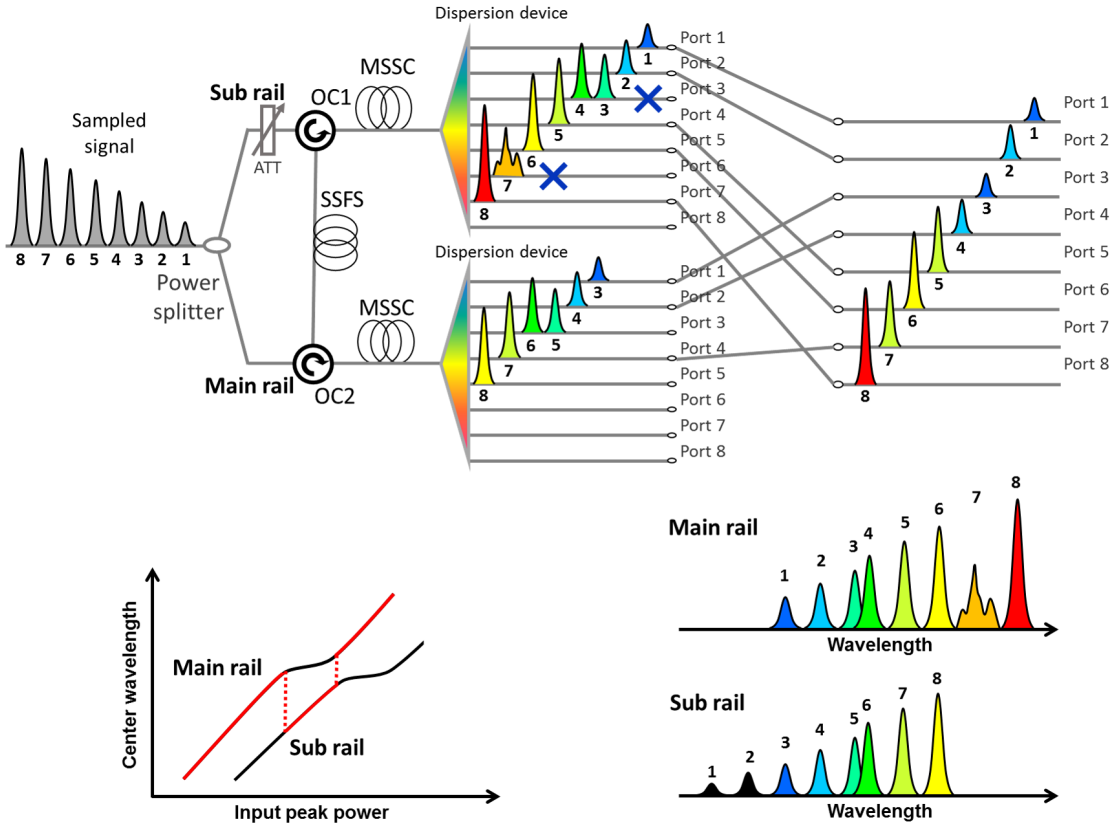

Figure 6.3: Schematic diagram of Principle of quantization error improvement for optical quantization.

6.2.1 Principle of quantization error improvement for optical quantization

The resolution of quantization is restricted by the fineness of spectrum width after SSFS. Therefore, spectral compression is effective for resolution upgrade. Spectral compression is achieved by making a suitable balance between wavelength dispersion and phase modulation to the pulse. We have achieved a compression of spectral width to a few nm using a multi-stage SPM-based spectral compression (MSSC). Figure 6.1 shows the number of bit (NOB) corresponds to the resolution given by,

$$NOB = log_2 \left(\frac{\lambda_{shift} \Delta\lambda_{FWHM}}{\Delta\lambda_{FWHM}} \right), \tag{6.1}$$

where λ_{shift} and $\Delta\lambda_{FWHM}$ are the amount of center wavelength shift and the spectral width of a signal after SSFS, respectively. Increase of λ_{shift} in eq. (6.1) upgrades the resolution. This is achieved by increasing input peak power as much as possible. However, with the input peak power increasing, the shape of an amplified pulse is

distorted as a result of unnecessary nonlinear optical effects such as SPM or self-steeping in an amplifier before SSFS. A distorted pulse induces a stagnation of the amount of center wavelength shift of SSFS at some specific input peak power regions as shown in Fig. 6.2 (a). This phenomenon could induce serious quantization error. Decrease of $\Delta\lambda_{FWHM}$ in eq. (6.1) can upgrade the resolution too. In proposed quantization, SPM-based spectral compression is used for different wavelength shifted pulses after SSFS. Since the balance in spectral compression fluctuates depending on the wavelength, the distortions of spectra occur at some specific input peak power regions as shown in Fig. 6.2 (b). Then, these phenomena could induce a serious quantization error because the discrimination of each input intensity is difficult at the regions. The quantization error causes degradation of the ENOB.

To avoid the degradation of the ENOB by the quantization error, we propose a dual rail configuration of optical quantization. The schematic diagram is shown in Fig. 6.3. Each sampled signal is divided into two pulses before SSFS and these two pulses propagate different routes; main rail and sub rail. The main rail consists of three parts: intensity-to-wavelength conversion, spectral compression, and wavelength separation as is the case in a single rail. In the main rail, a sampled signal propagates upwardly through a HNLF for SSFS by an optical circulator (OC1) and through SMFs and HNLFs for MSSC. Some specific input peak power regions are unavailable due to the stagnations of wavelength shift and the distortions of spectra. On the other hand, the sub rail consists of an optical attenuator (ATT) in addition to the three parts. In the sub rail, a sampled signal propagates downwardly through the same HNLF in the main rail for SSFS by an optical circulator (OC2) and through SMFs and HNLFs for MSSC. The variance of center wavelength shift of SSFS as a function of an input peak power in the sub rail can be changed to the different variance in the main rail by use of the ATT. The sub rail have different unavailable input peak power regions where the stagnations and the distortions are induced. Therefore, combining the both rails, the discrimination of each input intensity could be achieved in whole input peak power region.

6.2.2 Experiment

We experimentally verified the quantization error improvement effect by the proposed technique in 6 bit optical quantization. Although the proposed technique requires

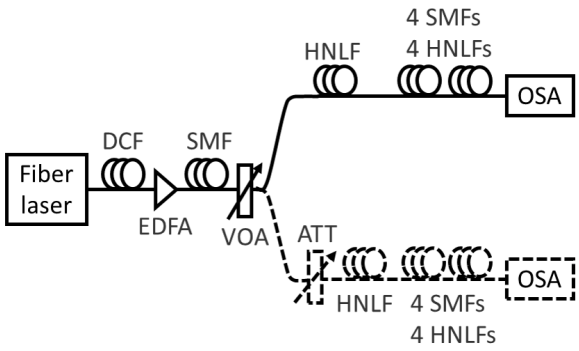

Figure 6.4: Experimental setup.

optical circulators that are available over the entire region of wavelength shift by SSFS, a usable band of a commercial available optical circulator is mostly the C-BAND and L-BAND. Since, previous 6 bit optical quantization system uses a wide range from the L-BAND to U-BAND, we used two HNLFs without optical circulators. If a short wavelength pulse laser could be prepared, the proposed configuration using optical circulators and a single HNLF is possible. Figure 6.4 shows the experimental setup. We used optical pulses from a fiber laser (IMRA America Inc.) as a light source. The pulse width, the center wavelength, and the repetition rate were 0.5 ps, 1559 nm, and 50 MHz, respectively. Here, we used a relatively low repetitive frequency laser to provide a sufficient peak power for generation of SSFS because this scheme has the inherent feature of sampling rate transparency. To generate high peak power pulses, we used an EDFA with chirped pulse amplification (CPA). We prepared sampled pulses with pseudo-continuously varied peak power as a substitute of an input analog signal. To prepare sampled pulses, we adjusted power of optical pulses using a variable optical attenuator (VOA). We varied the peak power of optical pulses from 22.0 W to 66.0 W. Input sampled analog pulses were propagated in a 1 km HNLF (D=7 ps/nm/km, S=0.03 ps/nm2/km, nonlinearity: γ =15 /W/km) for the generation of SSFS. The wavelength shifted pulses were propagated through 4 SMFs and 4 HNLFs for MSSC and they were connected in the following order; 2 m SMF (D=17 ps/nm/km, S=0.06 ps/nm2/km, γ =1.5 /W/km), 92 m HNLF (D=-0.0185 ps/nm/km, S=0.0029 ps/nm2/km, γ =15 /W/km), 10 m SMF, 110 m HNLF (D=-0.266 ps/nm/km, S=0.0268 ps/nm2/km, γ =9.3 /W/km), 30 m SMF, 400 m HNLF (D=0.044 ps/nm/km, S=0.029 ps/nm2/km, γ =20 /W/km), 100 m SMF, 521 m HNLF (D=0.055 ps/nm/km, S=0.029 ps/nm2/km, γ =16 /W/km). The output spectra was

measured by an optical spectrum analyzer (OSA). Unfortunately, since we couldn't prepare only one set of 5 HNLFs and 4 SMFs for SSFS and MSSC, first we connected these fibers to the main rail and measured the output spectra, then the sub rail. To change the variance of center wavelength shift of SSFS as a function of input peak power in the sub rail to the different variance in the main rail, we inserted an ATT before SSFS. The ATT was set at 1.0 dB attenuation.

Figure 6.5 (a, b) indicates 64 output spectra with input peak power set at equal interval in the main rail and the sub rail, respectively. In the main rail, there are some spectra overlapping the next spectrum and some distorted spectra which doesn't satisfy the required condition for our optical quantization. On the other hand, although there are similarly some overlapping and distorted spectra in the sub rail, signal levels of these spectra are different from that of the main rail. Figure 6.6 shows the amount of center wavelength shift of the main rail, the sub rail, and the dual rail as a function of an input peak power. The dual rail is a combination of the available regions of the main rail and the sub rail. In order to idealize the quantization function with the number of switching as few as possible, we optimized the selection of the main rail and sub rail. From Fig. 6.6, we can confirm that whole input peak power region almost satisfies the required condition. Figure 6.7 shows the obtained quantization function from the main rail and the dual rail. Although there are missing codes in the main rail, there is no missing code in the dual rail.

Concerning the quantization error improvement effect of the proposed technique, we estimate the DNL, the INL, and the ENOB. DNL is the error of each quantization step size compared with the ideal quantization function and INL is the distance of the center of each quantization step from the ideal center line. The DNL, the INL, and the ENOB are derived from the quantization function. The calculated result of the DNL and the INL are shown in Fig. 6.8 and 6.9. The maximum DNL is improved from 1.31 least significant bit (LSB) in the main rail to 0.74 LSB in the dual rail. The maximum INL is improved from 0.42 LSB to 0.37 LSB. In the estimation of the ENOB, we use the following calculation to derive ENOB from signal to noise and distortion ratio (SINAD),

$$ENOB = 0.5log_2(SINAD) - 0.5log_2(1.5). \tag{6.2}$$

We assume a sine wave input and create a FFT plot from a reconstructed wave

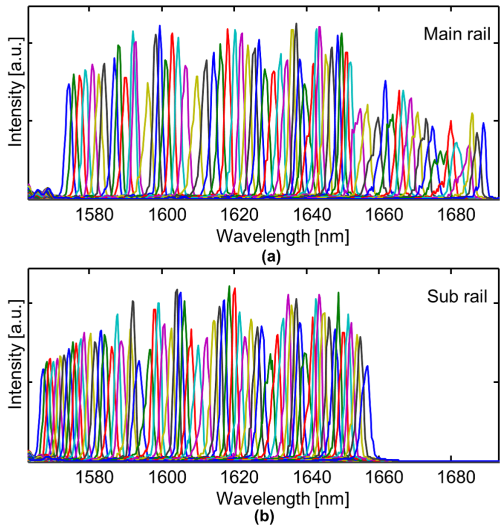

Figure 6.5: Experimental results of 64 output spectra of the main rail and the sub rail.

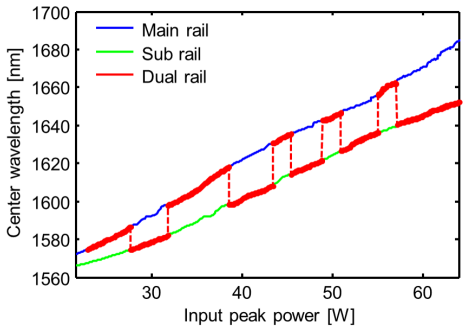

Figure 6.6: Experimental results of the amount of center wavelength shift of the main rail, the sub rail, and the dual rail.

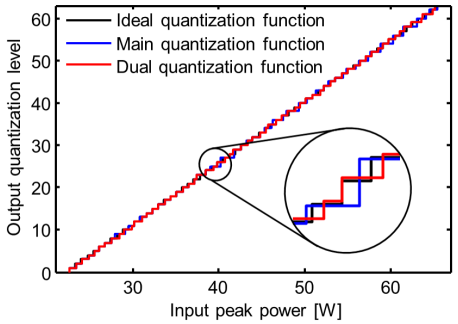

Figure 6.7: Experimentally obtained the transfer functions.

using quantized output data. The quantized output data in a FFT plot shows the fundamental input signal along with quantization noise and distortion. SINAD is the

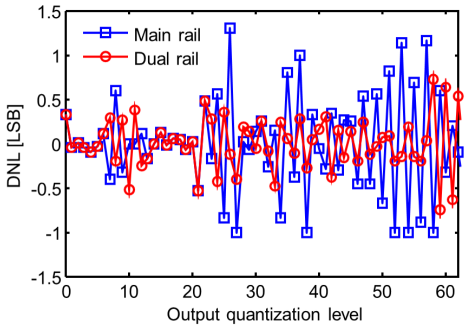

Figure 6.8: Differential nonlinearity.

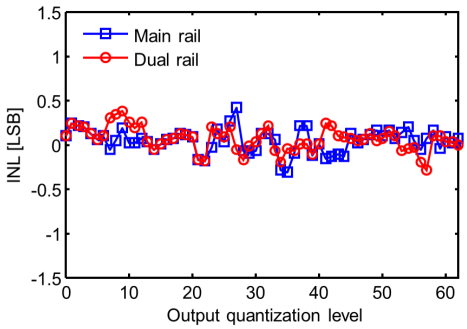

Figure 6.9: Integral nonlinearity.

ratio of the power of the fundamental to the power of all the other spectral components, including noise and distortion, but excluding DC. The ENOB is improved from 5.35 bit to 5.66 bit. These results show that our proposed method is very efficient for quantization error improvement. On the other hand, the improvement effect was limited to only 0.31 bit. When the unavailable input peak power regions of the sub rail overlap with that of the main rail, the proposed method corrects not all quantization errors. Using fibers of other properties, a large improvement effect could be expected. Moreover, although the system complexity increases, a large improvement effect could be also expected using even more sub rails.

6.2.3 Discussion

In HNLF for SSFS, the bidirectional pulses could go by each other and coexist in the proposed configuration using optical circulators and a single HNLF. Opposite directional pulses induce XPM influence. The XPM interaction between two counter-propagating pulses is generally quite weak and can be neglected in the case of ultra-short pulses because it would be very short time for interaction between the two

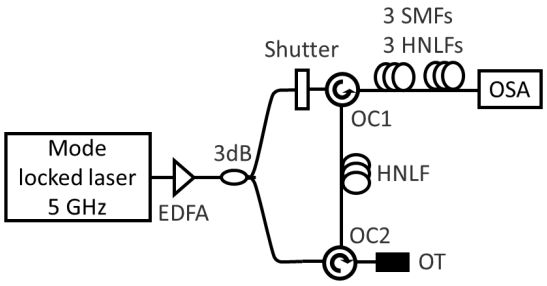

Figure 6.10: Experimental setup of 5 GS/s optical quantization system.

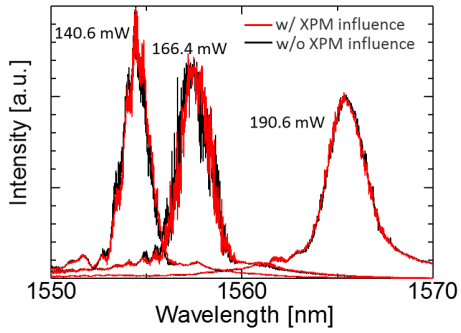

Figure 6.11: Experimental results of output spectra.

pulses.[71] However, at high sampling rate such as 10∼100 GS/s, a pulse encounters enormous number of pulses along a 1 km fiber. For example at 10 GS/s, XPM are caused nearly 100000 times in 1 km HNLF. Since the XPM influence may not be negligible under such a condition, we examined the XPM influence between counter-propagating pulses at high sampling rate. First, we experimentally examined the XPM influence in 5 GS/s optical quantization system. Figure 6.10 shows the experimental setup. Each optical pulse was divided into two pulses by a 3 dB coupler and these two pulses propagated different routes by optical circulators. The output of OC2 was connected to an optical terminator (OT). To compare the difference by the XPM influence, we switched an existence of opposite directional pulses by controlling the shutter in the sub rail. The output spectra of the main rail for average power of 140.6 mW, 166.4 mW, and 190.6 mW are shown in Fig. 6.11. Black line is the spectra with the XPM influence, and red line is the spectra without the XPM influence. The XPM couldn't affect the output spectra. Finally, we examine the XPM influence at much higher sampling rate in a simulation. Generally, the fiber propagation is analyzed by

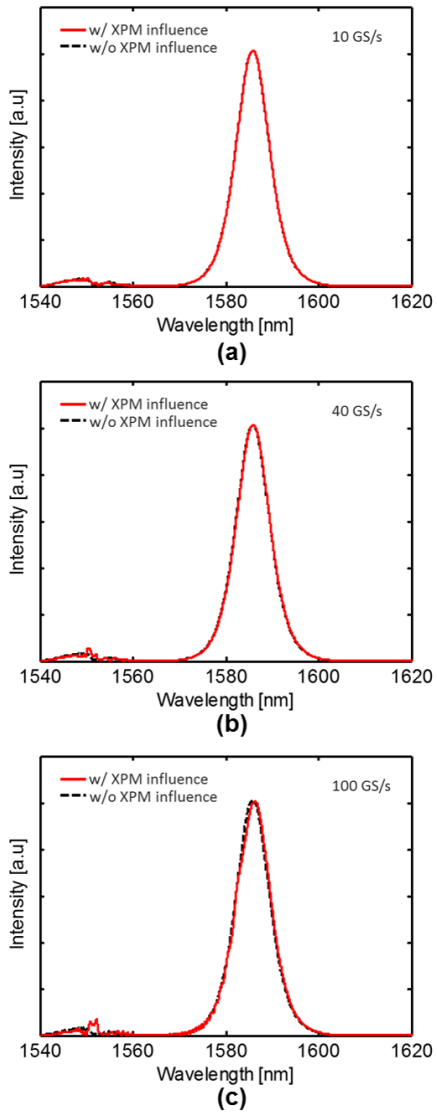

Figure 6.12: Simulation results of the spectra after SSFS at 10 GS/s, 40 GS/s, and 100 GS/s.

solving the generalized nonlinear Schrodinger equation which is represented by,[71]

$$\frac{\partial A_i}{\partial z} + \frac{\alpha}{2}A_i + \frac{j\beta_2}{2}\frac{\partial^2 A_i}{\partial T^2} - \frac{\beta_3}{6}\frac{\partial^3 A_i}{\partial T^3} = j\gamma\left(B \mid A_c \mid^2 A_i + \mid A_i \mid^2 A_c + \frac{2j}{\omega_0}\frac{\partial}{\partial T}(\mid A_i \mid^2 A_i) - T_R A_i \frac{\partial \mid A_i \mid^2}{\partial T}\right), \quad (6.3)$$

where α is the attenuation, z is the propagation distance, β_2 and β_3 is dispersion coefficients, γ is the nonlinear coefficient, T_R is the Raman coefficient, and B is the XPM coefficient. Although B is 2 in the case of same polarization, B is 2/3 in the case of vertical polarization. Numerical calculation is solved by the split-step Fourier

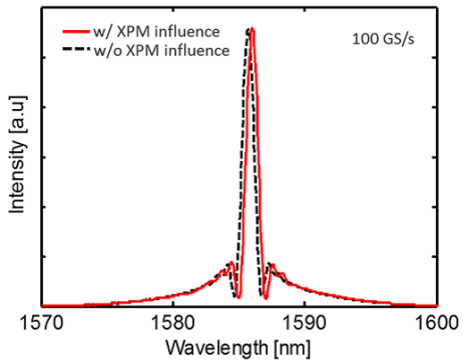

Figure 6.13: Simulation results of the spectra after spectral compression at 100 GS/s.

method (SSFM), which obtains an approximate solution by assuming that in propagating the optical field over a small distance step h, the dispersion and nonlinear effects can be assumed to behave independently. In one directional propagation, since a relatively long step size such as several cm has high accuracy, SSFM could be performed at high speed even for long fibers. Since, however, the interaction distance between two counter-propagating pulses is only several hundred um, further short step size is required for high accuracy calculation. To reduce the calculation time, we change the step size along the propagation depending on an existence of opposite directional pulses. In addition, we assume that the polarization of each pulse is same and the intensity waveform of the opposite directional pulse doesn't change. Figure 6.12 (a)-(c) shows the calculation results of 10 GS/s, 40 GS/s, and 100 GS/s optical quantization systems without spectral compression. Under 10 GS/s and 40 GS/s conditions, the XPM influence couldn't be found. On the other hand, under 100 GS/s condition, we can find a little difference between spectra by the XPM influence. Figure 6.13 shows the spectra of 100 GS/s after spectral compression. A distortion by the XPM influence couldn't be found. However, with the XPM influence, the center wavelength after spectral compression changes to a little bit higher wavelength. The difference of the wavelength shift between with and without the XPM influence is 0.23 nm. This difference is equivalent to DNL of 0.13 LSB. From these results, it may be concluded that the XPM influence can be negligible under 40 GS/s conditions. Moreover, if the polarizations of counter-propagating pulses are vertical, the XPM influence could be suppressed. This is achieved by using a polarization maintaining fiber.

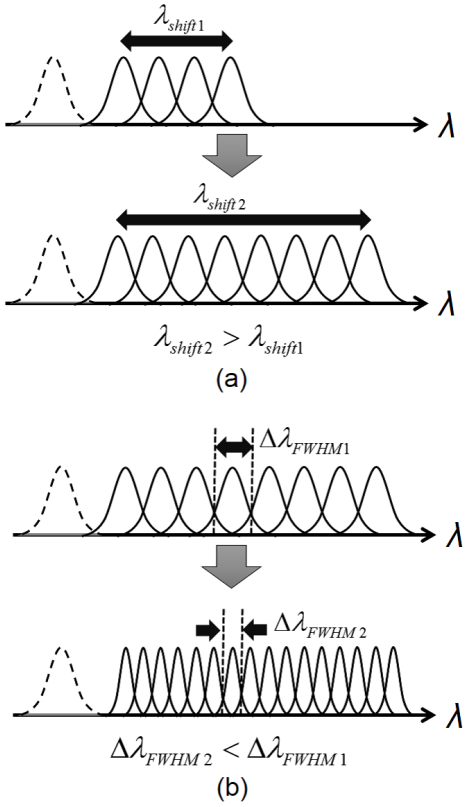

Figure 6.14: Conventional approaches for proposed optical quantization.

6.3 Parallel use of dispersion devices for resolution improvement of optical quantization at high sampling rate

Spectral compression induces stretching of the pulse width. Then, it restricts the sampling rate because the sampling rate is inversely proportional to the pulse width. As a result, a new tradeoff arises between the sampling rate and the resolution. To achieve a furthermore high performance all-optical ADC, it requires a different approach for resolution improvement of optical quantization without affecting the sampling rate. In this section, we focus on the linear function part in our proposed optical quantization and propose parallel use of dispersion devices for resolution improvement with keeping high sampling rate.

6.3.1 Principle of parallel use of dispersion devices for resolution improvement of optical quantization

In our previous work, we tried two approaches for resolution improvement. One approach is extension of wavelength shift as shown in Fig. 6.14 (a). Increase of λ_{shift} in eq.(6.1) upgrades the resolution. This is achieved by increasing input peak power as strong as possible. However, with the input peak power increasing, the shape of an amplified pulse is distorted as a result of unnecessary nonlinear optical effects in an amplifier before SSFS. A distorted pulse induces a stagnation of the amount of center wavelength shift of SSFS at some specific input peak power regions. This phenomenon could induce serious quantization error. To suppress unnecessary nonlinear optical effect in an amplifier, we employed CPA and demonstrated the wide range shift to 1670 nm from 1560 nm for our quantization system. However, a large wavelength difference between subsequent pulses causes an overlapping problem due to a group-velocity walk-off effect in a fiber. A delayed pulse threatens to overlap with a next pulse. This could lead to unnecessary nonlinear optical effects such as XPM. Therefore, the walk-off effect limits the amount of extension of wavelength shift. Another approach is compression of spectral width as shown in Fig. 6.14 (b). This is achieved by applying a suitable wavelength dispersion and phase modulation to the pulse. Decrease of $\Delta\lambda_{FWHM}$ in eq.(6.1) can upgrade the resolution. We have achieved compression of spectral width to a few nm. On the other hand, an uncertainty relationship exists between pulse width and spectral width of optical pulse and is represented by the following equation,

$$\Delta t \cdot \Delta\nu \geq \kappa, \tag{6.4}$$

where Δt and $\Delta\nu$ are the pulse width and the spectral width of an optical pulse, respectively, and κ is the constant value depending on the shape of an optical pulse. Eq.(6.4) suggests that pulse width and spectral width is an inverse relationship. Sampling rate of optical ADC is determined by pulse width of sampled pulse. A few nm spectral width is corresponding to the sampling rate over several 100s GS/s. Therefore, the spectral compression approach also restricts sampling rate.

To overcome the above mentioned limitation in a nonlinear function part, we shift our attention to a linear function part of optical quantization. In a new approach, additional use of different dispersion devices can assist wavelength separation by an original dispersion device. Using a dispersion device of which the center wavelength of

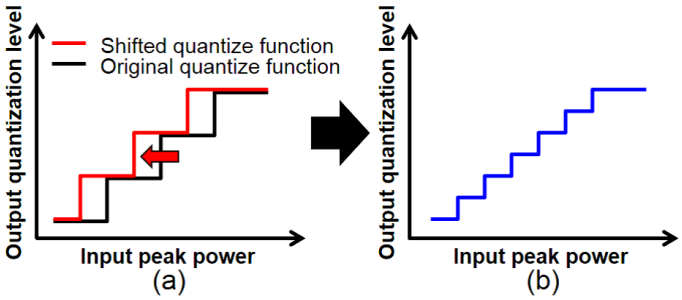

Figure 6.15: Concept of proposed resolution improvement technique.

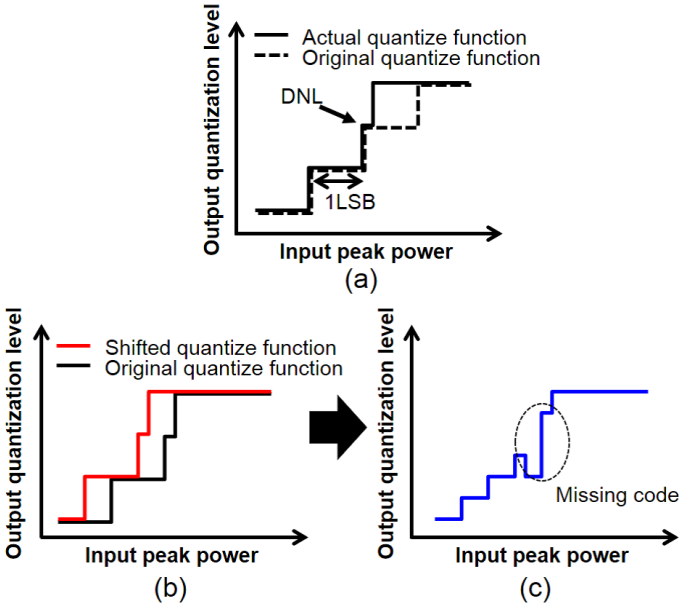

Figure 6.16: Influence of a quantization error.

each port is shifted from that of the original dispersion device, the obtained quantization function shifts from the original one as shown in Fig. 6.15. Here, quantization function means a relationship between input peak power and output quantization level. Input peak power range corresponding to one output level of the original quantization function could be separated to two by using half level shift of a quantization function. The intensity difference of half level can be distinguished because outputs for higher and lower levels in the range are different. As a result, a double resolved quantization function can be achieved. The effect of resolution improvement is in proportion to the number of different dispersion devices. An ideal quantization function has no limitation regarding resolution improvement by this method. However, an actual quantization function has some quantization errors as shown in Fig. 6.16 (a). Since shifted

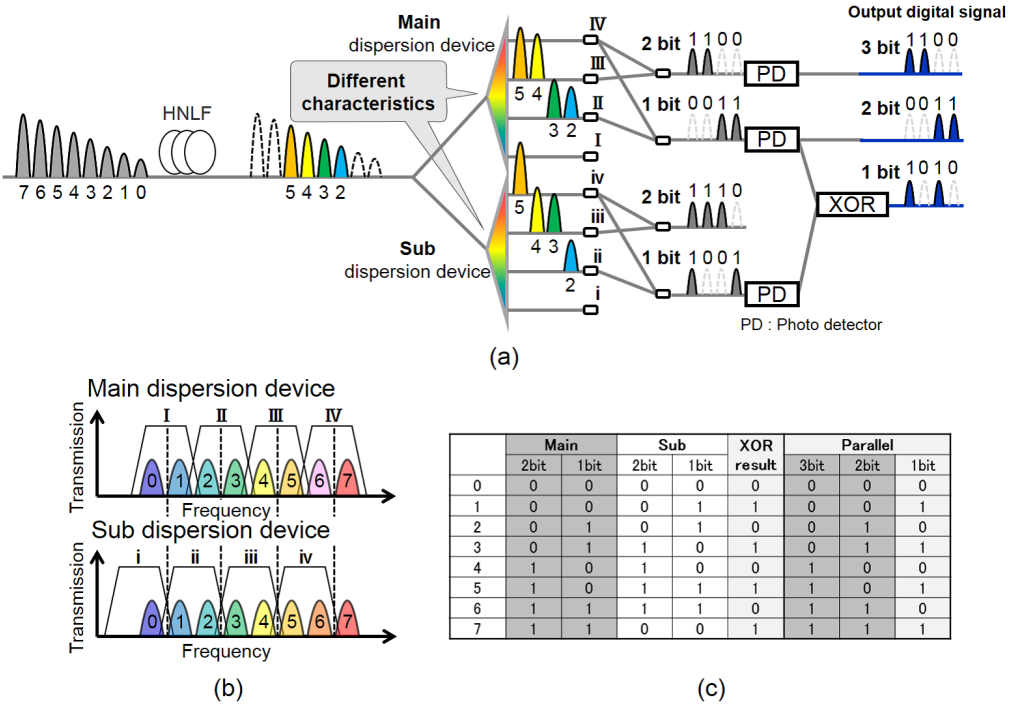

	Main		Sub		XOR	Parallel		
	2bit	1bit	2bit	1bit	result	3bit	2bit	1bit
0	0	0	0	0	0	0	0	0
1	0	0	0	1	1	0	0	1
2	0	1	0	1	0	0	1	0
3	0	1	1	0	1	0	1	1
4	1	0	1	0	0	1	0	0
5	1	0	1	1	1	1	0	1
6	1	1	1	1	0	1	1	0
7	1	1	0	0	1	1	1	1

Figure 6.17: Schematic diagram of principle of parallel use of dispersion devices for resolution improvement of optical quantization.

quantization functions have the same quantization errors of the original quantization function, the quantization errors are accumulated as shown in Fig. 6.16 (b). For example, DNL greater than 1 LSB may lead to occur a fatal defect called missing code as shown in Fig. 6.16 (c). Here, DNL is the error of each quantization step size compared with the ideal quantization function and LSB is the quantization step size of the ideal quantization function. There is the following equation of the relationship between the available maximum number of different dispersion devices and the value of the maximum DNL necessary for no missing code,

$$DNL_{max} \leq \frac{1}{N}, \tag{6.5}$$

where DNL_{max} is the value of the maximum DNL of the original quantization function and N is the available maximum number of different dispersion devices. Moreover, parallel use of dispersion devices complicates a coding process. However, if the number of different dispersion devices is two, it demands only a single exclusive OR (XOR) circuit. In this section, we discuss only in the case of two different dispersion devices. Figure 6.17 (a) shows a schematic diagram of the proposed parallel use of dispersion devices in optical quantization. Each wavelength shifted pulse is divided into two pulses

and they are fed to main and sub dispersion devices. As shown in Fig. 6.17 (b), the wavelength interval between each adjacent port of the sub dispersion device is the same as that of the main dispersion device. On the other hand, the center wavelength of each port of the sub dispersion device is set between the center wavelengths of each adjacent port of the main dispersion device. As a result, the timing at which the output port is switched in the sub dispersion device shifts from the case of the main dispersion device. In this system, optical coding is performed by optical interconnection technique by connecting braided waveguide, output pulse from each port of a dispersion device is converted to parallel digital bit train. We assume two pulses whose intensities are different each other. A single dispersion device system cannot recognize the slight difference of the wavelength of the pulses after SSFS. For example, No.2 and No.3 pulses in Fig. 6.17 (b) are emitted from the same port of a main dispersion device and converted to same digital signals. On the other hand, they are separated to the different ports of a sub dispersion device and converted to different digital signals. No.3 and No.4 pulses are in the opposite situation. We can use the difference of outputs from two dispersion devices to improve resolution twice of the single use of dispersion device. To finalize distinguishing the difference of outputs, XOR decision is necessary for the 1st bits of the main and sub output digital signals. As shown in Fig. 6.17 (c), by combining the main output and the XOR result as the least significant bit, we can get the double resolution.

6.3.2 Experiment

We verified the principle of resolution improvement by the proposed method in 3 bit optical quantization. Figure 6.18 (a) shows an experimental setup. We used optical pulses from a fiber laser. The pulse width, the center wavelength, and the repetition rate were 0.9 ps, 1559 nm, and 50 MHz, respectively. Here, we used a relatively low repetitive frequency laser to provide a sufficient peak power for generation of SSFS because this scheme has the inherent feature of sampling rate transparency. To generate high peak power pulse, a 330 m SMF1 (D=17 ps/nm/km, S=0.06 ps/nm2/km, γ =1.5 [/W/km]) , an EDFA, and a 40 m DCF1 (D=-160.0 ps/nm/km, S=0.06 ps/nm2/km, γ =1.5 /W/km) were used for CPA. We prepared input pulses with pseudo-continuously varied peak power as a substitute of an input analog signal. To prepare sampled analog pulses, we adjusted power of an optical pulse using a VOA. Input sampled

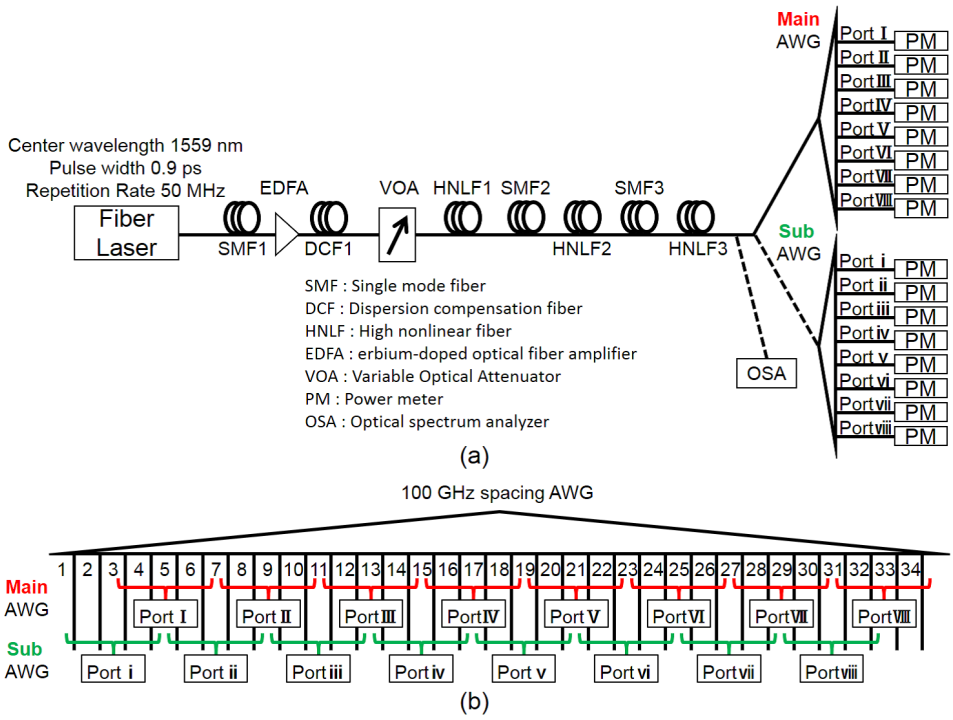

Figure 6.18: Experimental setup.

analog pulses were propagated through a 1 km HNLF1 (D=7.0 ps/nm/km, S=0.03 ps/nm2/km, γ =16 /W/km) for the generation of SSFS. The wavelength shifted pulses were propagated through two SMFs and two HNLFs for spectral compression and they were connected in the following order; 2 m SMF2, 92 m HNLF2 (D=-0.0185 ps/nm/km, S=0.0029 ps/nm2/km, γ =15 /W/km), 10 m SMF3, 110 m HNLF3 (D=-0.266 ps/nm/km, S=0.0268 ps/nm2/km, γ =9.3 /W/km). After spectral compression, the output spectra were measured by an OSA, and the average spectral width was 3.2 nm. Each pulse is fed to the arrayed waveguide grating (AWG). The free spectral range, the diffraction order and the passband shape of AWG are 10 THz, 19, and a Gaussian-type, respectively. Unfortunately, since we couldn't prepare 400 GHz spacing AWG which is suitable to 3.2 nm spectral width, we used continuous 4 ports of 100 GHz spacing AWG as 1 port of 400 GHz spacing AWG as shown in Fig. 6.18 (b).

Figure 6.19 shows the relationships between the center wavelengths and input peak powers after the spectral compression. Output center wavelength is almost linearly shifted from 1575 nm to 1600 nm according to the input peak power from 16 W to 25 W. Figure 6.20 indicates 8 output spectra of which input peak powers are set at equal interval. After spectral compression, the average spectral width was 3.2 nm. Figure

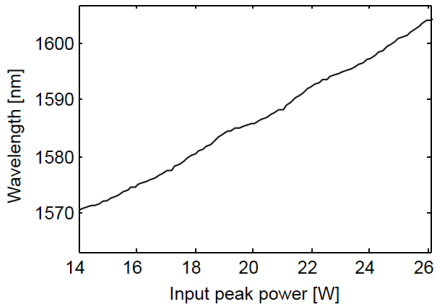

Figure 6.19: Experimental result of the relationships between the center wavelengths and input peak powers after the spectral compression.

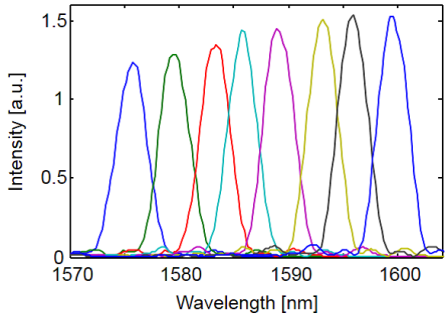

Figure 6.20: Experimental result of 8 output spectra of which input peak power are set at equal interval.

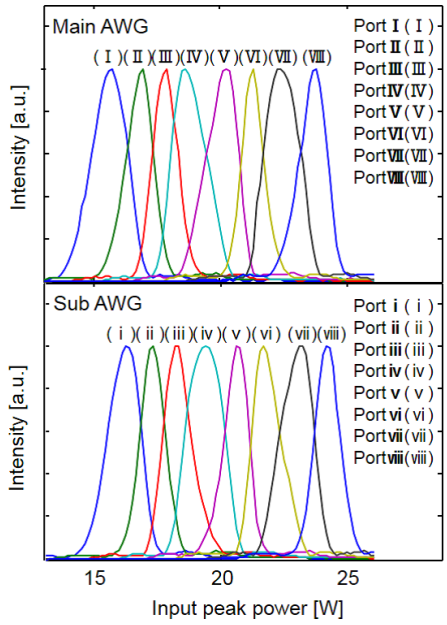

Figure 6.21: Experimental results of the measured output power of each output port.

6.21 shows the measured output power of each output port of main AWG and sub AWG as a function of an input peak power. We can find that the timing at which the

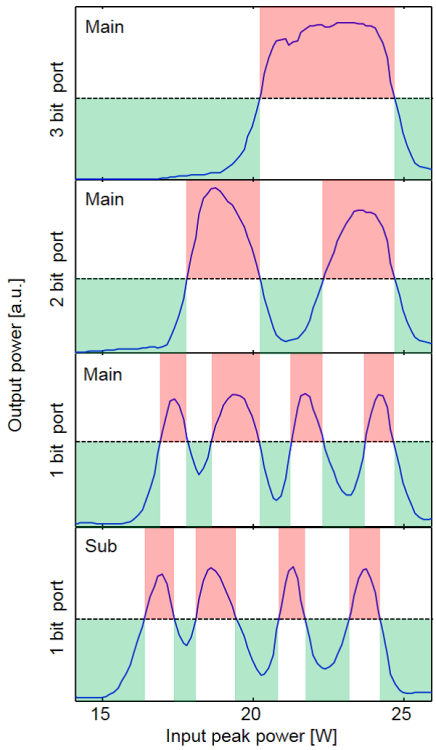

Figure 6.22: Simulation results of the transfer functions of main 1 3 bit ports and sub 1 bit port.

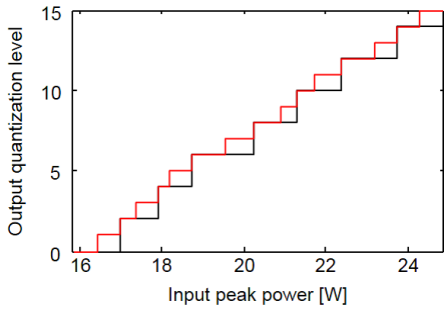

Figure 6.23: Simulation results of the quantization function of 3 bit optical quantization and 4 bit optical quantization.

output port is switched in the sub AWG shifted as compared with the case of the main AWG.

We performed a coding to the output signal after AWG by assuming connecting the coupler in a simulation. Here, we used the experimental data of optical quantization as input data of optical coding. Figure 6.22 shows the transfer functions of main 1∼3 bit ports and sub 1 bit port. From Fig. 6.22, we can obtain the quantization function using thresholding to each output port and XOR decision between main and sub 1st

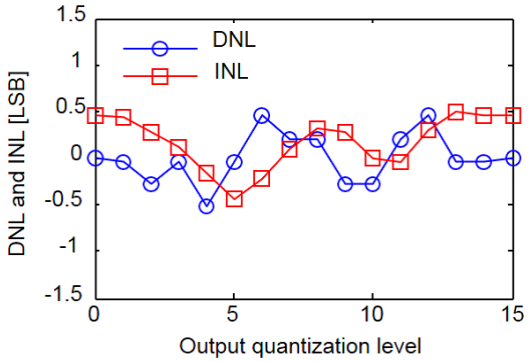

Figure 6.24: Simulation results of differential nonlinearity error and integral nonlinearity error.

bit. Figure 6.23 shows the quantization functions from main AWG and parallel AWGs. As a result, we successfully confirmed that 4 bit optical quantization was achieved with 3 bit optical quantization system. Concerning the resolution performance of proposed method, we estimate the DNL, the INL, and the ENOB which is associated with SINAD. The DNL, the INL, and the ENOB are derived from the experimentally obtained quantization function. The calculated result of the DNL and the INL are shown in Fig. 6.24. The maximum DNL and INL are 0.49 LSB and 0.50 LSB, respectively. The ENOB estimated to 3.62 bit.

6.4 Experimental demonstration of 40 GS/s 4 bit all-optical analog-to-digital conversion

Previously, the whole operation from sampling to coding has been experimentally demonstrated at only low sampling rates.[66] In this section, we experimentally demonstrate a 40 GS/s all-optical ADC system using sampling rate independent resolution improvement approach to prevent resolution degrading due to high sampling rates.

6.4.1 Experimental demonstration

The experimental setup is shown in Fig. 6.25. We used a MLFL as the optical pulse source. The center wavelength, repetition rate, and pulse width were 1545 nm, 10 GHz, and 1.2 ps, respectively. To create a 40 GHz sampling rate pulse train, the 10 GHz optical pulse source was fed to a quadruple multiplexer based on delay-line bit interleaver. Figures 6.26(a) and (b) show the waveform and spectra of the obtained

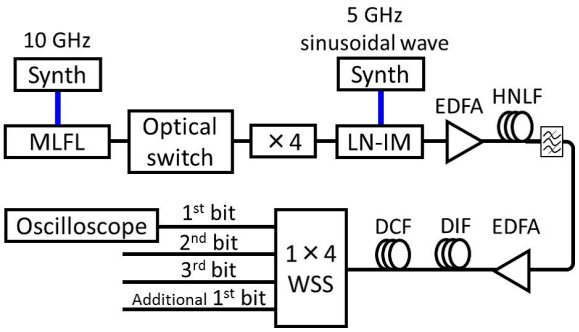

Figure 6.25: Experimental setup of 40 GS/s 4 bit all-optical ADC.

sampling pulse train. The 5 GHz sinusoidal wave is superimposed onto the 40 GHz sampling pulse train using a lithium niobate intensity modulator as the input analog radio frequency signal. After sampling, the pulse train is amplified using an EDFA and propagated in a 1 km HNLF (D=7.0 ps/nm/km, S=0.03 ps/nm2/km, γ =16 /W/km) to induce SSFS. Figure 6.26(c) shows the spectra after the HNLF at 196 mW input average power without the 5 GHz sinusoidal wave. For spectral compression, the wavelength-shifted pulse train is fed to a 1 km DIF (D = 0.0 to 15.0 ps/nm/km). The DIF can effectively compress the spectral width in an adiabatic process. Figure 6.26(d) shows the spectra after HNLF at 196 mW input average power without the 5 GHz sinusoidal wave. The spectral width after the DIF was 1.5 nm. A 90 m DCF was used to adjust the group velocity walk-off effect by chromatic dispersion. Because SSFS and spectral compression are nonlinear processes, a high input peak power is required. An optical switch after the MLFL controls the emission time of the optical pulse train to reduce saturation of the EDFA. The ratio between the ON and OFF times is set to 1:3. Higher nonlinearity devices such as photonics crystal fibers, chalcogenide waveguides, or silicon waveguides allow continuous operation.[119]

Figures 6.27(a) and (b) show the sampled signal with the 5 GHz sinusoidal wave and the output spectrum of the sampled signal after the DIF with the 5 GHz sinusoidal wave, respectively. The spectrum is the integration of several different power pulses. Wavelength separation and coding process are obtained by a 1×4 WSS, whose available wavelength range is from 1550 nm to 1565 nm. This range can contain 3-bit 8-level spectra. Used together with one additional coding filter for the parallel dispersion device approach, 40 GS/s 4 bit ADC was demonstrated. Figure 6.28 shows the installed 3-bit coding filters and additional 1-bit coding filter with the coding ta-

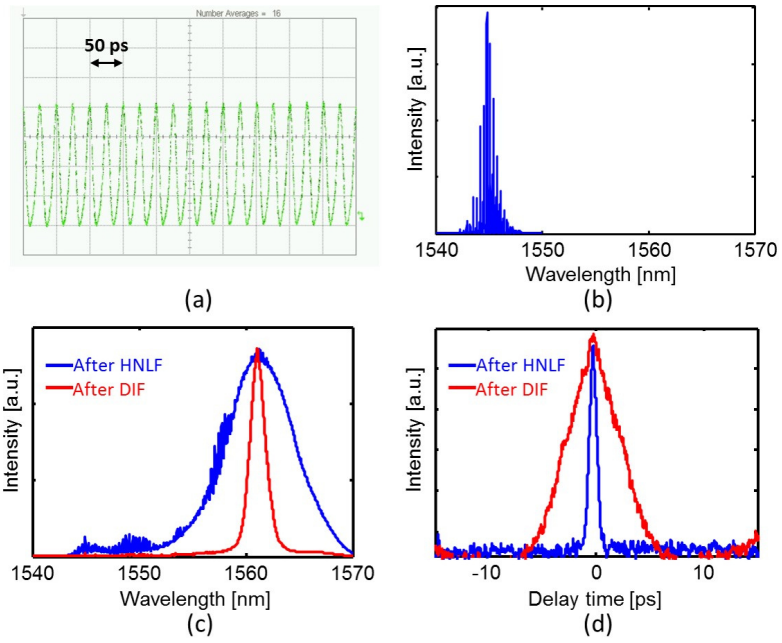

Figure 6.26: (a) Sampling pulse train. (b) Spectra of the sampling pulse train. (c) Spectra after HNLF and DIF at 196 mW input average power without an analog input signal. (d) Auto correlation traces after HNLF and DIF at 196 mW input average power without an analog input signal.

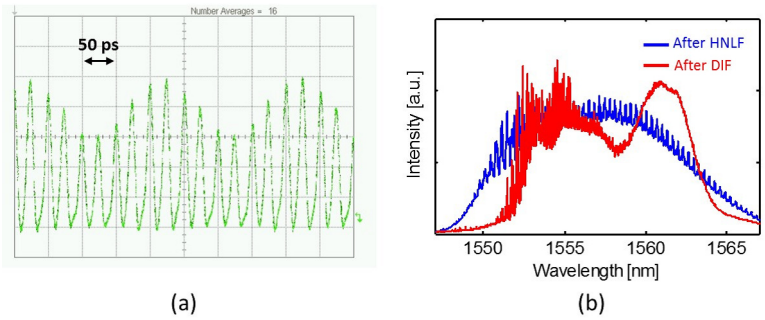

Figure 6.27: (a) Sampled signal with the 5 GHz sinusoidal wave. (b) Output spectra of the sampled signal after HNLF and DIF with the 5 GHz sinusoidal wave.

ble. The wavelength interval at the longer wavelength side is slightly larger than at the shorter wavelength side because the amounts of wavelength shift differ depending on wavelength. To compensate for the output power, the attenuation at the longer wavelength side is higher than at the shorter wavelength side. Figure 6.29 shows the temporal waveforms of each output signal from the WSS. These signals are compared with the appropriate threshold voltages to obtain binary signals. Figure 6.30 shows a plot of reconstructed waveform overlaid with the 5 GHz sinusoidal wave. As a result, we successfully confirmed that the input analog signal is converted to a digital signal.

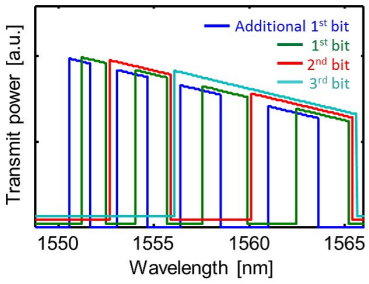

Decimal	3rd bit	2nd bit	1st bit	Additional 1st bit
0	0	0	0	0
1	0	0	0	1
2	0	0	1	1
3	0	0	1	0
4	0	1	0	0
5	0	1	0	1
6	0	1	1	1
7	0	1	1	0
8	1	0	0	0
9	1	0	0	1
10	1	0	1	1
11	1	0	1	0
12	1	1	0	0
13	1	1	0	1
14	1	1	1	1
15	1	1	1	0

Figure 6.28: Installed 3-bit coding filters and additional 1-bit coding filter.

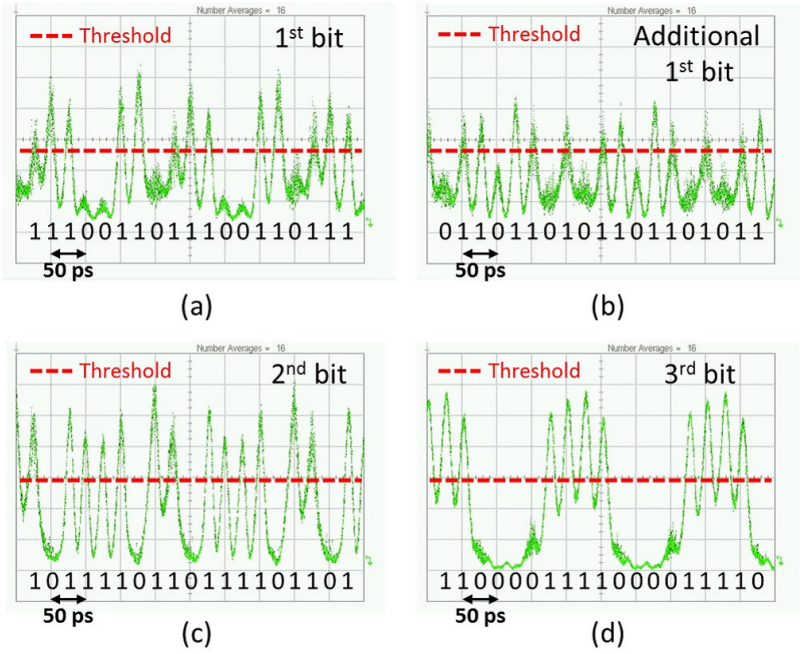

Figure 6.29: Measured temporal waveform of each output signal from the WSS.

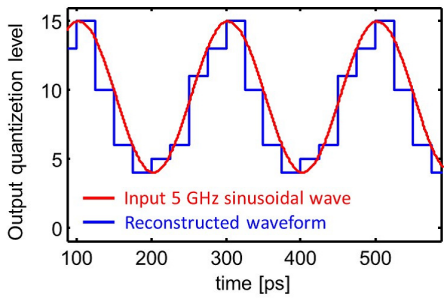

Figure 6.30: Overlaid plot of the input 5 GHz sinusoidal wave and reconstructed waveform.

6.4.2 Discussion

To evaluate the performance of 40 GS/s 4 bit ADC system, it is useful to estimate the ENOB. However, the estimation of ENOB requires a lower frequency sinusoidal wave

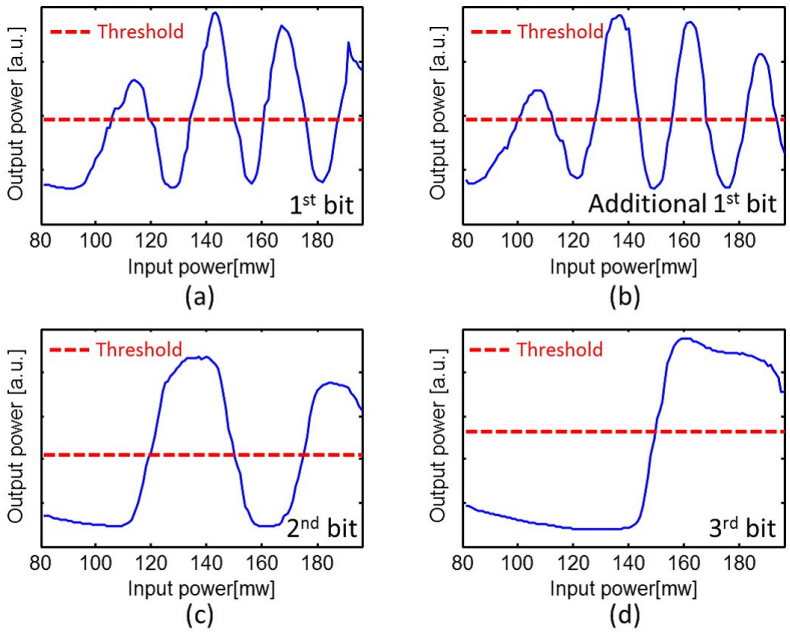

Figure 6.31: Transfer functions of the original 1- to 3-bit ports and additional 1-bit port.

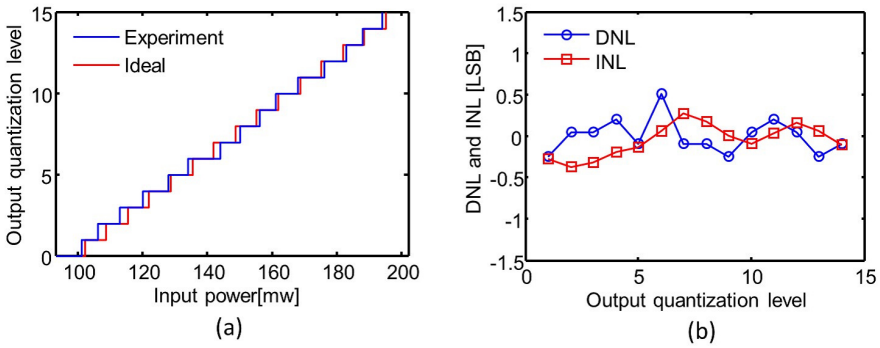

Figure 6.32: (a) Relationship between input power and output quantization level. (b) DNL and INL

input than our experimental setup supports. Instead, we estimated the ENOB from the experimentally obtained relationship between input power and output quantization level. Figure 6.31 shows the transfer functions of the 1- to 3-bit coding ports and additional 1-bit cording port. Using threshold lines and XOR decisions, we were able to obtain the relationship shown in Fig. 6.32(a). Figure 6.32(b) shows the calculated results of the DNL and the INL. The maximum DNL and INL are 0.5 LSB and 0.4 LSB, respectively. The ENOB was hence estimated to be 3.79 bits.

6.5 Conclusion

In this chapter, resolution improvement techniques of all-optical ADC were proposed to treat the received signal with higher performance in practical limitations. Firstly, to cope with a imperfection of components in the all-optical ADC, a quantization error improvement technique was presented and experimentally demonstrated. The ENOB was improved from 5.35 bit to 5.66 bit, even if the 6 bit optical quantization has a defective component. Secondly, to overcome a limitation of a trade off between sampling rate and resolution, a sampling rate independent resolution upgrade technique was presented. The experimental results show that the high resolution could be realized in high sampling rate condition. Using this technique, 40 GS/s 4 bit all-optical ADC was experimentally demonstrated. The demonstrated all-optical ADC has a better ENOB than the other 40 GS/s all-optical ADC.[58] Furthermore, applying the proposed technique to 6 bit or 7 bit optical quantizations, higher resolution is expected. In high sampling rate condition, a more high nonlinear optical device is required to induce the nonlinear effect because a power of each pulse becomes low. Since silicon waveguides has high nonlinearity, it is expected that it is useful for improving future performance.[120,121]

Conclusions

In this thesis, I focused on optical signal multiplexing using fractional Fourier transform and all-optical analog-to-digital conversion to realize the optimized signal processing for the limiting factor of large capacity communications. Performances of any communication systems could be maximized by optimizing transfer functions of their system. In optical communication, the increase of the transmission capacity has been limited due to signal impairments during a propagation. It is predicted that optical OFDM based on fractional Fourier transform in place of Fourier transform increases the system flexibility and suppresses signal impairments in the propagation. If the signal degradation is mitigated, the transmission capacity is expected to be further increased by a high-performance ADC. To get the best performance of a transmission system by optimizing its transfer function, the behavior of a transmission signal in actual optical fiber links was clarified. Additionally, a feasibility demonstration of devices and subsystems such as implementation of fractional Fourier transform and ADC in various environments was presented toward practical applications. Followings are the summaries presented in the sequence of chapters:

In Chapter 1, introduction of optical signal multiplexing in optical communication was presented as an essential procedure. Overviews of current situation in optical signal multiplexing for large capacity optical communications and phenomena induced in optical fibers during transmission were described. To get the best performance of a transmission system for further large capacity optical communications, an optimization of transfer function including an optical signal multiplexing is required.

In Chapter 2, an optical OFDM based on fractional Fourier transform in place of conventional Fourier transform was presented. It is expected that the fractional Fourier transform can handle signals in a new domain for more frexible applications than the conventinal Fourier transform. The theoretical backgrounds of fractional Fourier transform and the method of all-optical implementation for an optical signal

was described. The behavior of optical fractional OFDM signal in a dispersive fiber focusing on the reduction of peak to average power ratio was examined. The numerical simulation results show that the PAPR of fractional OFDM signal is decreased at a point where the Nyquist pulse train is formed by the time-lens effect. Moreover, the fiber nonlinearity mitigation technique was proposed and demonstrated by evaluating the transmission performance of the optical fractional OFDM signal in the dispersion compensated fiber link in simulation. The signal quality after the 1100 km propagation of a dispersion compensated fiber link was successfully improved by 1.0 dB as compared with the conventional OFDM. It is expected that this new fractional Fourier transform based optimization approach for a control of a PAPR of a optical signal is useful to increase usable information.

In Chapter 3, to confirm that the fractional Fourier transform can generalize the Fourier transform with keeping original useful functions in the Fourier transform, a verification of CP insertion for all-optical fractional OFDM was presented. We experimentally demonstrated the insertion of a CP in a four-channel 40 Gbit/s all-optical fractional OFDM signal. The measured BER showed that the CP improves the signal quality even if the performance of the time gate is insufficient. The relationship between the fractional parameter and the effect of CP insertion was investigated in simulation. In conjunction with nonlinearity mitigation presented in Chapter 2, all-optical fractional OFDM could mitigate the degradation of the signal quality due to nonlinear and linear impairments by optimizing the fractional parameter in accordance with the characteristic of fibers and the performance of system components.

In Chapter 4, we experimentally demonstrated the feasibility of the all-optical fractional OFDM system in a practical network system. Firstly, to guarantee the operation in an actual network, the field trial in JGN-X was successfully demonstrated. The 40 Gbit/s optical fractional OFDM signal could be demultiplexed after the 89.2-km transmission. If there are ICI due to residual dispersion or insufficient timegates, the cyclic prefix insertion mitigates the degradation of the signal quality. Secondly, the WSS-based multiplexing and PLC-based demultiplexing of a 12×10 Gbit/s DBPSK optical fractional OFDM signal were experimentally demonstrated. This combination has advantages both in terms of network architecture flexibility, and in the reduction of system cost and complexity. Thirdly, the demultiplexing of optical fractional OFDM signal by time-lens effect was demonstrated. Treating the optical fractional OFDM

signal like a N-OTDM signal, the signal is demultiplexed by an ultra-fast time gate without the fractional Fourier transform. From these experiments, the feasibility of the all-optical fractional OFDM system was demonstrated. These demonstrations in an optical communication field ensures a reliability of the optical signal multiplexing based on fractional Fourier transform in wide fields.

In Chapter 5, the necessity and issue on all-optical ADC were experimentally examined to cope with an optical fractional OFDM signal. All-optical ADC is expected to afford the high multiplicity of multilevel modulation for a received optical fractional OFDM signal. To demonstrate the feasibility of all-optical ADC for a received optical fractional OFDM signal, the experimental demonstration of a demodulation of 4-ASK optical fractional OFDM signal using 2 bit all-optical ADC was presented. The demonstration was performed in low bit resolution to confirm a compatibility of all-optical ADC with a received optical fractional OFDM signal. Once the number of levels is upgraded, a high resolution all-optical ADC is required.

In Chapter 6, to treat the received signal with higher performance in practical limitations, resolution improvement techniques of all-optical ADC were proposed. Firstly, to cope a imperfection of components in the all-optical ADC, a quantization error improvement technique was presented and experimentally demonstrated. The ENOB was improved from 5.35 bit to 5.66 bit, even if the 6 bit optical quantization has a defective component. Secondly, to overcome a limitation of a trade off between sampling rate and resolution, a sampling rate independent resolution upgrade technique was presented. The experimental results show that the high resolution could be realized in high sampling rate condition. Using this technique, 40 GS/s 4 bit all-optical ADC was experimentally demonstrated. The demonstrated all-optical ADC has a better ENOB than the other 40 GS/s all-optical ADC.[58] Furthermore, applying the proposed technique to 6 bit or 7 bit optical quantizations, higher resolution is expected. In high sampling rate condition, a more high nonlinear optical device is required to induce the nonlinear effect because a power of each pulse becomes low. Since silicon waveguides has high nonlinearity, it is expected that it is useful for improving future performance.[120,121]

As is summarizes above, an optical signal multiplexing using fractional Fourier transform and all-optical analog-to-digital conversion can realize a maximization of a performance of a transmission system by optimizing its transfer function. The feasi-

bility demonstrations of the proposed approach in an optical communication system could ensure a reliability of the proposed approach in any other systems such as measurement systems. Since optical circuits for fractional Fourier transform and all-optical ADC can greatly benefit from silicon photonics that has developed rapidly in recent years,[120–122] it is expected that a further performance improvement and popularization promote applications of the proposed approach in a wide field.

Abbreviations

ADC	Analog to digital conversion
ASE	Amplified spontaneous emission
ASK	Amplitude shift keying
ATT	Optical attenuator
AWG	Arrayed waveguide grating
BER	Bit error rate
BPD	Balanced photo detector
CCDF	Complementary cumulative distribution function
CP	Cyclic prefix
DBP	Digital back-propagation
DBPSK	Differential binary phase shift keying
DCF	Dispersion compensation fiber
DFT	Discrete Fourier transform
DIF	Dispersion increasing fiber
DNL	Differential nonlinearity
EDFA	Erbium doped optical Fiber amplifier
ENOB	Effective number of bit
FEC	Forward error correction
FFT	Fast Fourier transform
FrFT	Fractional Fourier transform
FWHM	Full width at half maximum
FWM	Four wave mixing
HNLF	High nonlinear fiber
IDFT	Inverse discrete Fourier transform
ICI	Inter channel interference
INL	Integral nonlinearity

ISI	Inter symbol interference
JGN-X	Japan Gigabit Network eXtreme
LN-IM	Lithium niobate intensity modulator
LSB	Least significant bit
MLFL	Mode locked fiber laser
MLLD	Mode locked laser diode
MSSC	Multi stage SPM based spectral compression
N-OTDM	Nyquist-optical time division multiplexing
NOLM	Nonlinear loop mirror
NLSE	Nonlinear Schrodinger equation
ODL	Optical delay line
OFDM	Orthogonal frequency division multiplexing
OOK	On off keying
OSA	Optical spectrum analyzer
PAPR	Peak to average power ratio
PC	Polarization controller
PLC	Planar lightwave circuit
PRBS	Pseudo random bit sequence
PSK	Phase shift keying
QAM	Quadrature amplitude modulated
SINAD	Signal to noise and distortion ratio
SMF	Single mode fiber
SNR	Signal to noise ratio
SPM	Self phase modulation
SSFM	Split step Fourier method
SSFS	Soliton self frequency shift
VOA	Variable optical attenuator
WDM	Wavelength division multiplexing
WSS	Wavelength selective switch
XPM	Cross phase modulation

Acknowledgments

I would like to express my gratitude to the people who have helped me with this thesis. First and foremost, I am grateful to Associate Professor Tsuyoshi Konishi at Graduate School of Engineering, Osaka University for his invaluable guidance, helpful suggestion, continuous encouragement, and constructive discussion throughout this study. He provided an ideal environment for me to carry out my study. I would like to express my sincere appreciations to Professor Yoshizo Takai, Professor Heiji Watanabe, and Professor Yasuo Kanematsu for their valuable suggestions and comments on this thesis. I make grateful acknowledgment to Professor Gabriella Cincotti at University Roma Tre for her invaluable guidance and fruitful discussion. Grateful acknowledgments are given to Dr. Naoya Wada, Dr. Satoshi Shimizu, Mr. Ken Makino, Mr. Hiroyuki Sumimoto, Mr. Takahiro Hashimoto, and Dr. Hideaki Furukawa, who are member of National Institute of Information and Communications Technology, for their helpful advice and support in the experiments. My sincere appreciation is extended to Dr. Kunihiro Hattori, Dr. Masanori Okuno, Dr. Shinji Mino, and Dr. Akira Himeno at NTT Electronics for their support in the fabrication of the planar lightwave circuit throughout this study. I would like to thank Professor Hiroyuki Uenohara at Tokyo Institute of Technology for his helpful suggestion and support of the experimental equipment. I would like to thank Dr. Takahiro Kodama for his support in the experiments. I would also like to thank Dr. Julian Hoxha for many constructive discussion. I am deeply grateful to Professor Kazuyoshi Itoh at Osaka University for helpful advices and encouragement. I am thankful to Mr. Kentaro Kawanishi, Mr. Kouji Takahashi, Mr. Hideki Matsui, and Mr. Takema Sato for their helpful and supportive advices in my dairy study. My hearty thanks are extended to my colleagues, Mr. Ryosuke Nagao, Mr. Takuya Murakawa, and, Mr. Makoto Hasegawa for their helpful discussion and friendship. Further, my hearty thanks are also given to all members of the research group for their kind support; Mrs. Mihoko Mizoguchi, Mr. Wataru Akiba, Mr. Motoki

Hiraoka, Mr. Yu Yamasaki, etc.

Finally, I am grateful to my family for their understanding, encouragement and support on this study.

This work was supported by JSPS KAKENHI, Grant-in-Aid for JSPS Research Fellow, 261585. This work was supported by STARBOARD project of MIC Strategic Harmonized International R&D Promotion Programme SHIP.

References

[1] C. V. N. Index, "The zettabyte era," http://www.cisco.com/c/en/us/solutions/collateral/service-provider/visual-networking-index-vni/vni-hyperconnectivity-wp.pdf (2016).

[2] W. Shieh, H. Bao, and Y. Tang, "Coherent optical ofdm: theory and design," Optics Express **16**, 841–859 (2008).

[3] I. B. Djordjevic and B. Vasic, "Orthogonal frequency division multiplexing for high-speed optical transmission," Optics Express **14**, 3767–3775 (2006).

[4] A. Lowery and J. Armstrong, "Orthogonal-frequency-division multiplexing for dispersion compensation of long-haul optical systems," Optics Express **14**, 2079–2084 (2006).

[5] J. Armstrong and A. Lowery, "Power efficient optical ofdm," Electronics Letters **42**, 370–372 (2006).

[6] A. J. Lowery, L. B. Du, and J. Armstrong, "Performance of optical ofdm in ultralong-haul wdm lightwave systems," Journal of Lightwave Technology **25**, 131–138 (2007).

[7] J. Armstrong and B. J. Schmidt, "Comparison of asymmetrically clipped optical ofdm and dc-biased optical ofdm in awgn," IEEE Communications Letters **12**, 343–345 (2008).

[8] B. J. Schmidt, A. J. Lowery, and J. Armstrong, "Experimental demonstrations of electronic dispersion compensation for long-haul transmission using direct-detection optical ofdm," Journal of Lightwave Technology **26**, 196–203 (2008).

[9] J. Armstrong, "Ofdm for optical communications," Journal of Lightwave Technology **27**, 189–204 (2009).

[10] K. Lee, C. T. Thai, and J.-K. K. Rhee, "All optical discrete fourier transform processor for 100 gbps ofdm transmission," Optics Express **16**, 4023–4028 (2008).

[11] W. Li, X. Liang, W. Ma, T. Zhou, B. Huang, and D. Liu, "A planar waveguide optical discrete fourier transformer design for 160gb/s all-optical ofdm systems," Optical Fiber Technology **16**, 5–11 (2010).

[12] D. Hillerkuss, R. Schmogrow, T. Schellinger, M. Jordan, M. Winter, G. Huber, T. Vallaitis, R. Bonk, P. Kleinow, F. Frey *et al.*, "26 tbit s-1 line-rate super-channel transmission utilizing all-optical fast fourier transform processing," Nature Photonics **5**, 364–371 (2011).

[13] H. Chen, M. Chen, and S. Xie, "All-optical sampling orthogonal frequency-division multiplexing scheme for high-speed transmission system," Journal of Lightwave Technology **27**, 4848–4854 (2009).

[14] Z. Wang, K. S. Kravtsov, Y.-K. Huang, and P. R. Prucnal, "Optical fft/ifft circuit realization using arrayed waveguide gratings and the applications in all-optical ofdm system," Optics Express **19**, 4501–4512 (2011).

[15] A. J. Lowery, "Design of arrayed-waveguide grating routers for use as optical ofdm demultiplexers," Optics Express **18**, 14129–14143 (2010).

[16] S. Shimizu, G. Cincotti, and N. Wada, "Demonstration and performance investigation of all-optical ofdm systems based on arrayed waveguide gratings," Optics Express **20**, B525–B534 (2012).

[17] L. B. Du, J. Schroeder, J. Carpenter, B. Eggleton, and A. J. Lowery, "Flexible all-optical ofdm using wsss," in "Optical Fiber Communication Conference," (Optical Society of America, 2013), pp. PDP5B–9.

[18] J. Schröder, M. A. Roelens, L. B. Du, A. J. Lowery, S. Frisken, and B. J. Eggleton, "An optical fpga: Reconfigurable simultaneous multi-output spectral pulse-shaping for linear optical processing," Optics Express **21**, 690–697 (2013).

[19] K.-P. Ho, *Phase-modulated optical communication systems* (Springer Science & Business Media, 2005).

[20] D.-S. Ly-Gagnon, S. Tsukamoto, K. Katoh, and K. Kikuchi, "Coherent detection of optical quadrature phase-shift keying signals with carrier phase estimation," Journal of Lightwave Technology **24**, 12 (2006).

[21] P. J. Winzer and R.-J. Essiambre, "Advanced modulation formats for high-capacity optical transport networks," Journal of Lightwave Technology **24**, 4711–4728 (2006).

[22] M. G. Taylor, "Coherent detection method using dsp for demodulation of signal and subsequent equalization of propagation impairments," IEEE Photonics Technology Letters **16**, 674–676 (2004).

[23] S. J. Savory, G. Gavioli, R. I. Killey, and P. Bayvel, "Electronic compensation of chromatic dispersion using a digital coherent receiver," Optics Express **15**, 2120–2126 (2007).

[24] G. Goldfarb and G. Li, "Chromatic dispersion compensation using digital iir filtering with coherent detection," IEEE Photonics Technology Letters **19**, 969–971 (2007).

[25] E. Ip and J. M. Kahn, "Compensation of dispersion and nonlinear impairments using digital backpropagation," Journal of Lightwave Technology **26**, 3416–3425 (2008).

[26] E. Mateo, L. Zhu, and G. Li, "Impact of xpm and fwm on the digital implementation of impairment compensation for wdm transmission using backward propagation," Optics Express **16**, 16124–16137 (2008).

[27] E. Ip, "Nonlinear compensation using backpropagation for polarization-multiplexed transmission," Journal of Lightwave Technology **28**, 939–951 (2010).

[28] D. Rafique, M. Mussolin, M. Forzati, J. Mårtensson, M. N. Chugtai, and A. D. Ellis, "Compensation of intra-channel nonlinear fibre impairments using simplified digital back-propagation algorithm," Optics Express **19**, 9453–9460 (2011).

[29] J. Pan and C.-H. Cheng, "Nonlinear electrical compensation for the coherent optical ofdm system," Journal of Lightwave Technology **29**, 215–221 (2011).

[30] E. Yamazaki, S. Yamanaka, Y. Kisaka, T. Nakagawa, K. Murata, E. Yoshida, T. Sakano, M. Tomizawa, Y. Miyamoto, S. Matsuoka *et al.*, "Fast optical channel recovery in field demonstration of 100-gbit/s ethernet over otn using real-time dsp," Optics Express **19**, 13179–13184 (2011).

[31] L. B. Du and A. J. Lowery, "Improved single channel backpropagation for intra-channel fiber nonlinearity compensation in long-haul optical communication systems," Optics Express **18**, 17075–17088 (2010).

[32] S. J. Savory, G. Gavioli, E. Torrengo, and P. Poggiolini, "Impact of interchannel nonlinearities on a split-step intrachannel nonlinear equalizer," IEEE Photonics Technology Letters **22**, 673–675 (2010).

[33] X. Li, X. Chen, G. Goldfarb, E. Mateo, I. Kim, F. Yaman, and G. Li, "Electronic post-compensation of wdm transmission impairments using coherent detection and digital signal processing," Optics Express **16**, 880–888 (2008).

[34] A. Yariv, D. Fekete, and D. M. Pepper, "Compensation for channel dispersion by nonlinear optical phase conjugation," Optics Letters **4**, 52–54 (1979).

[35] S. Watanabe, T. Naito, and T. Chikama, "Compensation of chromatic dispersion in a single-mode fiber by optical phase conjugation," IEEE Photonics Technology Letters **5**, 92–95 (1993).

[36] C. Lorattanasane and K. Kikuchi, "Design theory of long-distance optical transmission systems using midway optical phase conjugation," Journal of Lightwave Technology **15**, 948–955 (1997).

[37] A. Chowdhury, G. Raybon, R.-J. Essiambre, J. H. Sinsky, A. Adamiecki, J. Leuthold, C. R. Doerr, and S. Chandrasekhar, "Compensation of intrachannel nonlinearities in 40-gb/s pseudolinear systems using optical-phase conjugation," Journal of Lightwave Technology **23**, 172 (2005).

[38] S. Jansen, D. Van den Borne, B. Spinnler, S. Calabro, H. Suche, P. Krummrich, W. Sohler, G.-D. Khoe, and H. De Waardt, "Optical phase conjugation for ultra long-haul phase-shift-keyed transmission," Journal of Lightwave Technology **24**, 54–64 (2006).

[39] L. B. Du, M. M. Morshed, and A. J. Lowery, "Fiber nonlinearity compensation for ofdm super-channels using optical phase conjugation," Optics Express **20**, 19921–19927 (2012).

[40] G. Cincotti, "Optical ofdm based on the fractional fourier transform," in "SPIE OPTO," (International Society for Optics and Photonics, 2012), pp. 828409–828409.

[41] C. Laperle and M. O ' Sullivan, "Advances in high-speed dacs, adcs, and dsp for optical coherent transceivers," Journal of Lightwave Technology **32**, 629–643 (2014).

[42] R. H. Walden, "Analog-to-digital converter survey and analysis," IEEE Journal on Selected Areas in communications **17**, 539–550 (1999).

[43] P. W. Juodawlkis, J. C. Twichell, G. E. Betts, J. J. Hargreaves, R. D. Younger, J. L. Wasserman, F. J. O'Donnell, K. G. Ray, and R. C. Williamson, "Optically sampled analog-to-digital converters," IEEE Transactions on Microwave Theory and Techniques **49**, 1840–1853 (2001).

[44] E. Yoshida and M. Nakazawa, "Measurement of the timing jitter and pulse energy fluctuation of a pll regeneratively mode-locked fiber laser," IEEE Photonics Technology Letters **11**, 548–550 (1999).

[45] P. W. Juodawlkis, J. C. Twichell, J. L. Wasserman, G. E. Betts, and R. C. Williamson, "Measurement of mode-locked laser timing jitter by use of phase-encoded optical sampling," Optics Letters **26**, 289–291 (2001).

[46] R. K. Shelton, S. M. Foreman, L.-S. Ma, J. L. Hall, H. C. Kapteyn, M. M. Murnane, M. Notcutt, and J. Ye, "Subfemtosecond timing jitter between two independent, actively synchronized, mode-locked lasers," Optics Letters **27**, 312–314 (2002).

[47] K. Yvind, D. Larsson, L. J. Christiansen, C. S. Angelo, L. K. Oxenløwe, J. Mørk, D. Birkedal, J. M. Hvam, and J. Hanberg, "Low-jitter and high-power 40 ghz all-active mode-locked lasers," IEEE Photonics Technology Letters **16**, 975–977 (2004).

[48] J. Kim, J. Chen, J. Cox, and F. X. Kärtner, "Attosecond-resolution timing jitter characterization of free-running mode-locked lasers," Optics Letters **32**, 3519–3521 (2007).

[49] Y. Song, C. Kim, K. Jung, H. Kim, and J. Kim, "Timing jitter optimization of mode-locked yb-fiber lasers toward the attosecond regime," Optics Express **19**, 14518–14525 (2011).

[50] W. Ng, R. Stephens, D. Persechini, and K. Reddy, "Ultra-low jitter modelocking of er-fibre laser at 10ghz and its application in photonic sampling for analogue-to-digital conversion," Electronics Letters **37**, 1 (2001).

[51] G. C. Valley, "Photonic analog-to-digital converters," Optics Express **15**, 1955–1982 (2007).

[52] A. Khilo, S. J. Spector, M. E. Grein, A. H. Nejadmalayeri, C. W. Holzwarth, M. Y. Sander, M. S. Dahlem, M. Y. Peng, M. W. Geis, N. A. DiLello *et al.*, "Photonic adc: overcoming the bottleneck of electronic jitter," Optics Express **20**, 4454–4469 (2012).

[53] B. L. Shoop, *Photonic analog-to-digital conversion*, vol. 81 (Springer, 2012).

[54] J.-M. Jeong and M. Marhic, "All-optical analog-to-digital and digital-to-analog conversion implemented by a nonlinear fiber interferometer," Optics Communications **91**, 115–122 (1992).

[55] P. Ho, Q. Wang, J. Chen, Q. Liu, and R. Alfano, "Ultrafast optical pulse digitization with unary spectrally encoded cross-phase modulation," Applied Optics **36**, 3425–3429 (1997).

[56] S.-i. Oda, S.-i. Okamoto, and A. Maruta, "A novel quantization scheme by slicing supercontinuum spectrum for all-optical analog-to-digital conversion," in "Nonlinear Guided Waves and Their Applications," (Optical Society of America, 2004), p. TuB3.

[57] S. Oda and A. Maruta, "Two-bit all-optical analog-to-digital conversion by filtering broadened and split spectrum induced by soliton effect or self-phase mod-

ulation in fiber," IEEE Journal of Selected Topics in Quantum Electronics **12**, 307 (2006).

[58] J. Stigwall and S. Galt, "Demonstration and analysis of a 40-gigasample/s interferometric analog-to-digital converter," Journal of Lightwave Technology **24**, 1247 (2006).

[59] T. Konishi, K. Tanimura, K. Asano, Y. Oshita, and Y. Ichioka, "All-optical analog-to-digital converter by use of self-frequency shifting in fiber and a pulse-shaping technique," JOSA B **19**, 2817–2823 (2002).

[60] T. Nishitani and T. Konishi, "All-optical analog-to-digital conversion using optical delay line encoders," IEICE Transactions on Electronics **90**, 479–480 (2007).

[61] T. Nishitani, T. Konishi, and K. Itoh, "Optical coding scheme using optical interconnection for high sampling rate and high resolution photonic analog-to-digital conversion," Optics Express **15**, 15812–15817 (2007).

[62] T. Konishi, K. Takahashi, H. Matsui, T. Satoh, and K. Itoh, "Five-bit parallel operation of optical quantization and coding for photonic analog-to-digital conversion," Optics Express **19**, 16106–16114 (2011).

[63] T. Nishitani, T. Konishi, and K. Itoh, "Resolution improvement of all-optical analog-to-digital conversion employing self-frequency shift and self-phase-modulation-induced spectral compression," IEEE Journal of Selected Topics in Quantum Electronics **14**, 724–732 (2008).

[64] T. Kato, T. Konishi, T. Nishitani, and K. Itoh, "All-optical analog-to-digital conversion system with a spatial coding method using designed filter," Optical Review **16**, 184–187 (2009).

[65] T. Satoh, K. Takahashi, H. Matsui, K. Itoh, and T. Konishi, "10-gs/s 5-bit real-time optical quantization for photonic analog-to-digital conversion," IEEE Photonics Technology Letters **24**, 830–832 (2012).

[66] M. Hasegawa, T. Satoh, T. Nagashima, M. Mendez, and T. Konishi, "Below 100-fs timing jitter seamless operations in 10-gsample/s 3-bit photonic analog-to-digital conversion," IEEE Photonics Journal **7**, 1–7 (2015).

[67] K. Kao and G. A. Hockham, "Dielectric-fibre surface waveguides for optical frequencies," Electrical Engineers, Proceedings of the Institution of **113**, 1151–1158 (1966).

[68] A. Sano, T. Kobayashi, S. Yamanaka, A. Matsuura, H. Kawakami, Y. Miyamoto, K. Ishihara, and H. Masuda, "102.3-tb/s (224 x 548-gb/s) c-and extended l-band all-raman transmission over 240 km using pdm-64qam single carrier fdm with digital pilot tone," in "National Fiber Optic Engineers Conference," (Optical Society of America, 2012), pp. PDP5C–3.

[69] D. Qian, M.-F. Huang, E. Ip, Y.-K. Huang, Y. Shao, J. Hu, and T. Wang, "101.7-tb/s (370× 294-gb/s) pdm-128qam-ofdm transmission over 3× 55-km ssmf using pilot-based phase noise mitigation," in "National Fiber Optic Engineers Conference," (Optical Society of America, 2011), p. PDPB5.

[70] Y. Emori, K. Tanaka, and S. Namiki, "100 nm bandwidth flat-gain raman amplifiers pumped and gain-equalised by 12-wavelength-channel wdm laser diode unit," Electronics Letters **35**, 1355–1356 (1999).

[71] G. P. Agrawal, *Nonlinear fiber optics* (Academic press, 2007).

[72] U. Gliese, S. Norskov, and T. Nielsen, "Chromatic dispersion in fiber-optic microwave and millimeter-wave links," IEEE Transactions on Microwave Theory and Techniques **44**, 1716–1724 (1996).

[73] G. H. Smith, D. Novak, and Z. Ahmed, "Overcoming chromatic-dispersion effects in fiber-wireless systems incorporating external modulators," IEEE Transactions on Microwave Theory and Techniques **45**, 1410–1415 (1997).

[74] R. W. Boyd, *Nonlinear optics* (Academic press, 2003).

[75] J. W. Goodman, *Introduction to Fourier optics* (Roberts and Company Publishers, 2005).

[76] H. M. Ozaktas and D. Mendlovic, "Fourier transforms of fractional order and their optical interpretation," Optics Communications **101**, 163–169 (1993).

[77] H. M. Ozaktas and D. Mendlovic, "Fractional fourier transforms and their optical implementation. ii," JOSA A **10**, 2522–2531 (1993).

[78] D. Mendlovic and H. M. Ozaktas, "Fractional fourier transforms and their optical implementation: I," JOSA A **10**, 1875–1881 (1993).

[79] P. Pellat-Finet, "Fresnel diffraction and the fractional-order fourier transform," Optics Letters **19**, 1388–1390 (1994).

[80] L. B. Almeida, "The fractional fourier transform and time-frequency representations," IEEE Transactions on Signal Processing **42**, 3084–3091 (1994).

[81] H. M. Ozaktas, O. Arikan, M. A. Kutay, and G. Bozdagi, "Digital computation of the fractional fourier transform," IEEE Transactions on Signal Processing **44**, 2141–2150 (1996).

[82] S.-C. Pei, M.-H. Yeh, and C.-C. Tseng, "Discrete fractional fourier transform based on orthogonal projections," IEEE Transactions on Signal Processing **47**, 1335–1348 (1999).

[83] S.-C. Pei, M.-H. Yeh, and T.-L. Luo, "Fractional fourier series expansion for finite signals and dual extension to discrete-time fractional fourier transform," IEEE Transactions on Signal Processing **47**, 2883–2888 (1999).

[84] Ç. Candan, M. A. Kutay, and H. M. Ozaktas, "The discrete fractional fourier transform," IEEE Transactions on Signal Processing **48**, 1329–1337 (2000).

[85] A. Bultheel and H. E. M. Sulbaran, "Computation of the fractional fourier transform," Applied and Computational Harmonic Analysis **16**, 182–202 (2004).

[86] R. Tao, B. Deng, and Y. Wang, "Research progress of the fractional fourier transform in signal processing," Science in China Series F **49**, 1–25 (2006).

[87] M. Martone, "A multicarrier system based on the fractional fourier transform for time-frequency-selective channels," IEEE Transactions on Communications **49**, 1011–1020 (2001).

[88] Y. Ju, B. Barkat, and S. Attallah, "Analysis of peak-to-average power ratio of a multicarrier system based on the fractional fourier transform," in "2004 9th IEEE Singapore International Conference on Communication Systems, New York: IEEE," (2004), pp. 165–168.

[89] G. Cincotti, "Generalized fiber fourier optics," Optics Letters **36**, 2321–2323 (2011).

[90] T. Murakawa, G. Cincotti, T. Nagashima, M. Hasegawa, K. Hattori, M. Okuno, S. Mino, A. Himeno, N. Wada, H. Uenohara *et al.*, "Fractional ofdm based transmitter and receiver for time/frequency multiplexing in gridless, elastic networks," in "Optical Fiber Communication Conference," (Optical Society of America, 2015), pp. W3C–1.

[91] T. Konishi, T. Murakawa, T. Nagashima, M. Hasegawa, S. Shimizu, K. Hattori, M. Okuno, S. Mino, A. Himeno, H. Uenohara *et al.*, "Flexible ofdm-based access systems with intrinsic function of chromatic dispersion compensation," Optical Fiber Technology **26**, 94–99 (2015).

[92] G. Cincotti, T. Murakawa, T. Kodama, K. Hattori, M. Okuno, S. Mino, A. Himeno, T. Nagashima, M. Hasegawa, N. Wada *et al.*, "Flexible power-efficient nyquist-otdm transmitter, using a wss and time-lens effect," in "Optical Fiber Communication Conference," (Optical Society of America, 2015), pp. W3C–5.

[93] M. Nakazawa, T. Hirooka, P. Ruan, and P. Guan, "Ultrahigh-speed "orthogonal" tdm transmission with an optical nyquist pulse train," Optics Express **20**, 1129–1140 (2012).

[94] T. Hirooka, P. Ruan, P. Guan, and M. Nakazawa, "Highly dispersion-tolerant 160 gbaud optical nyquist pulse tdm transmission over 525 km," Optics Express **20**, 15001–15007 (2012).

[95] T. Hirooka and M. Nakazawa, "Linear and nonlinear propagation of optical nyquist pulses in fibers," Optics Express **20**, 19836–19849 (2012).

[96] K. Harako, D. Seya, T. Hirooka, and M. Nakazawa, "640 gbaud (1.28 tbit/s/ch) optical nyquist pulse transmission over 525 km with substantial pmd tolerance," Optics Express **21**, 21062–21075 (2013).

[97] M. A. Soto, M. Alem, M. A. Shoaie, A. Vedadi, C.-S. Brès, L. Thévenaz, and T. Schneider, "Optical sinc-shaped nyquist pulses of exceptional quality," Nature Communications **4** (2013).

[98] H. N. Tan, T. Inoue, T. Kurosu, and S. Namiki, "Transmission and pass-drop operations of mixed baudrate nyquist otdm-wdm signals for all-optical elastic network," Optics Express **21**, 20313–20321 (2013).

[99] H. Hu, D. Kong, E. Palushani, M. Galili, H. C. H. Mulvad, and L. K. Oxenløwe, "320 gb/s nyquist otdm received by polarization-insensitive time-domain oft," Optics Express **22**, 110–118 (2014).

[100] D. Wang, L. Huo, Y. Xing, X. Jiang, and C. Lou, "Optical nyquist pulse generation using a time lens with spectral slicing," Optics Express **23**, 4329–4339 (2015).

[101] B. Costa, D. Mazzoni, M. Puleo, and E. Vezzoni, "Phase shift technique for the measurement of chromatic dispersion in optical fibers using led's," IEEE Journal of Quantum electronics **18**, 1509–1515 (1982).

[102] L. Cohen, "Comparison of single-mode fiber dispersion measurement techniques," Journal of Lightwave Technology **3**, 958–966 (1985).

[103] G. Ghosh, M. Endo, and T. Iwasaki, "Temperature-dependent sellmeier coefficients and chromatic dispersions for some optical fiber glasses," Journal of Lightwave Technology **12**, 1338–1342 (1994).

[104] T. Kato, Y. Koyano, and M. Nishimura, "Temperature dependence of chromatic dispersion in various types of optical fiber," Optics Letters **25**, 1156–1158 (2000).

[105] T. Yamamoto and M. Nakazawa, "Third-and fourth-order active dispersion compensation with a phase modulator in a terabit-per-second optical time-division multiplexed transmission," Optics Letters **26**, 647–649 (2001).

[106] M. J. Hamp, J. Wright, M. Hubbard, and B. Brimacombe, "Investigation into the temperature dependence of chromatic dispersion in optical fiber," IEEE Photonics Technology Letters **14**, 1524–1526 (2002).

[107] D. J. Barros and J. M. Kahn, "Optimized dispersion compensation using orthogonal frequency-division multiplexing," Journal of Lightwave Technology **26**, 2889–2898 (2008).

[108] H. Chen, X. Gu, F. Yin, M. Chen, and S. Xie, "5× 200gbit/s all-optical ofdm transmission using a single optical source and optical fourier transform real-time detection," Optics Express **19**, 21199–21204 (2011).

[109] A. J. Lowery, "Inserting a cyclic prefix using arrayed-waveguide grating routers in all-optical ofdm transmitters," Optics Express **20**, 9742–9754 (2012).

[110] J. Schröder, L. B. Du, J. Carpenter, B. J. Eggleton, and A. J. Lowery, "All-optical ofdm with cyclic prefix insertion using flexible wavelength selective switch optical processing," Journal of Lightwave Technology **32**, 752–759 (2014).

[111] X. Wang, N. Wada, T. Miyazaki, G. Cincotti, and K.-i. Kitayama, "Field trial of 3-wdm× 10-ocdma× 10.71-gb/s asynchronous wdm/dpsk-ocdma using hybrid e/d without fec and optical thresholding," Journal of Lightwave Technology **25**, 207–215 (2007).

[112] M. Jinno, H. Takara, B. Kozicki, Y. Tsukishima, Y. Sone, and S. Matsuoka, "Spectrum-efficient and scalable elastic optical path network: architecture, benefits, and enabling technologies," IEEE Communications Magazine **47**, 66–73 (2009).

[113] J. Hoxha, J. Morosi, S. Shimizu, P. Martelli, P. Boffi, N. Wada, and G. Cincotti, "Spectrally-efficient all-optical ofdm by wss and awg," Optics Express **23**, 10986–10996 (2015).

[114] J. Morosi, J. Hoxha, P. Martelli, P. Parolari, G. Cincotti, S. Shimizu, N. Wada, and P. Boffi, "25 gbit/s per user coherent all-optical ofdm for tbit/s-capable pons," Journal of Optical Communications and Networking **8**, 190–195 (2016).

[115] G. Cincotti, "Enhanced functionalities for awgs," Journal of Lightwave Technology **33**, 998–1006 (2015).

[116] T. Nishitani, T. Konishi, and K. Itoh, "All-optical m-ary ask signal demultiplexer based on a photonic analog-to-digital conversion," Optics Express **15**, 17025–17031 (2007).

[117] K. Takahashi, H. Matsui, T. Nagashima, and T. Konishi, "Resolution upgrade toward 6-bit optical quantization using power-to-wavelength conversion for photonic analog-to-digital conversion," Optics Letters **38**, 4864–4867 (2013).

[118] T. Satoh, T. Nagashima, K. Itoh, and T. Konishi, "Power-saving approach toward 7-bit optical quantization for photonic analog-to-digital conversion," in "Conference on Lasers and Electro-Optics/Pacific Rim," (Optical Society of America, 2013), p. TuO1_2.

[119] R. Pant, C. Xiong, S. Madden, B. L. Davies, and B. J. Eggleton, "Investigation of all-optical analog-to-digital quantization using a chalcogenide waveguide: A step towards on-chip analog-to-digital conversion," Optics Communications **283**, 2258–2262 (2010).

[120] Q. Lin, O. J. Painter, and G. P. Agrawal, "Nonlinear optical phenomena in silicon waveguides: modeling and applications," Optics Express **15**, 16604–16644 (2007).

[121] J. Leuthold, C. Koos, and W. Freude, "Nonlinear silicon photonics." Nature Photonics **4** (2010).

[122] T. Fukazawa, F. Ohno, and T. Baba, "Very compact arrayed-waveguide-grating demultiplexer using si photonic wire waveguides," Japanese Journal of Applied Physics **43**, L673 (2004).

List of Publications

[1] T. Nagashima, T. Satoh, P. Catalin, K. Itoh, and T. Konishi, “Parallel Use of Dispersion Devices for Resolution Improvement of Optical Quantization at High Sampling Rate,” IEICE Transactions on Electronics, vol.E97-C, no.7, 787-794 (2014).

[2] T. Nagashima, M. Hasegawa, T. Murakawa, and T. Konishi, “Quantization Error Improvement for Optical Quantization Using Dual Rail Configuration,” IEICE Transactions on Electronics, vol.E98-C, no.8, 808-815 (2015).

[3] T. Nagashima, G. Cincotti, T. Murakawa, S. Shimizu, M. Hasegawa, K. Hattori, M. Okuno, S. Mino, A. Himeno, N. Wada, H. Uenohara, and T. Konishi, “Cost effective all-optical fractional OFDM receiver using an arrayed waveguide grating,” Optical Fiber Technology, vol.32, 119122 (2016).

[4] T. Nagashima, M. Hasegawa, and T. Konishi, “40 GSample/s All-Optical Analog to Digital Conversion with Resolution Degradation Prevention,” IEEE Photonics Technology Letters, vol.29, no.1, 74-77 (2017).

[5] T. Nagashima, G. Cincotti, T. Murakawa, S. Shimizu, M. Hasegawa, K. Hattori, M. Okuno, S. Mino, A. Himeno, N. Wada, H. Uenohara, and T. Konishi, “Experimental demonstration of cyclic prefix insertion for all-optical fractional OFDM,” Submitted to Optics Communications.

[6] T. Nagashima, G. Cincotti, T. Murakawa, S. Shimizu, M. Hasegawa, K. Hattori, M. Okuno, S. Mino, A. Himeno, N. Wada, H. Uenohara, and T. Konishi, “Peak-to-Average Power Ratio Reduction of Transmission Signal of All-optical Orthogonal Time/Frequency Domain Multiplexing using Fractional Fourier Transform,” in preparation.

[7] M. Hasegawa, T. Satoh, T. Nagashima, M. Mendez and T. Konishi, "Below 100 fs Timing Jitter Seamless Operations in 10-GSamples/s 3-bit Photonic Analog-to-Digital Conversion," IEEE Photonics Journal, vol.7, no.3, 7201007 (2015).

[8] T. Konishi, T. Murakawa, T. Nagashima, M. Hasegawa, S. Shimizu, K. Hattori, M. Okuno, S. Mino, A. Himeno, H. Uenohara, N. Wada, and G. Cincotti, "Flexible OFDM-based access systems with intrinsic function of chromatic dispersion compensation," Optical Fiber Technology, vol.26, 9499 (2015).

List of Proceedings of International Conferences

[1] T. Nagashima, T. Satoh, and T. Konishi, “Quantization error improvement in 6-bit optical quantization for photonic A/D conversion,” International Workshop on OPS & OCDMA, Pt3, Hong Kong, China (2012).

[2] T. Nagashima, T. Satoh, P. Catalin, K. Itoh, and T. Konishi, “Parallel Use of Dispersion Devices for Resolution Improvement of Optical Quantization At High Sampling Rate,” Conference on Lasers and Electro-Optics Pacific Rim, and OptoElectronics and Communications Conference / Photonics in Switching, TuO1-5, Kyoto, Japan (2013).

[3] T. Nagashima, M. Hasegawa, T. Murakawa and T. Konishi, “Effect Maximization of Quantization Step Slicing Approach for Resolution Improvement in Optical Quantization,” International Topical Meeting on Microwave Photonics / Asia-Pacific Microwave Photonics Conference, TuD-4, Hokkaido, Japan (2014).

[4] T. Nagashima, G. Cincotti, T. Murakawa, S. Shimizu, M. Hasegawa, K. Hattori, M. Okuno, S. Mino, A. Himeno, N. Wada, H. Uenohara, T. Konishi, “Cyclic Prefix Insertion for All-optical Fractional OFDM,” Optical Fiber Technology, Photonics in Switching Conference 2015, We II 2-3, Florence, Italy (2015).

[5] T. Nagashima, G. Cincotti, T. Murakawa, S. Shimizu, M. Hasegawa, K. Hattori, M. Okuno, S. Mino, A. Himeno, N. Wada, H. Uenohara, T. Konishi, “PAPR Management of All-Optical OFDM Signal using Fractional Fourier Transform for Fibre Nonlinearity Mitigation,” 41st European Conference on Optical Communication, P.5.11, Valencia, Spain (2015).

[6] T. Nagashima, M. Hasegawa, T. Murakawa and T. Konishi, “Sampling Rate

Independent Resolution Upgrade for All-Optical Analog-to-Digital Conversion," Asia Communications and Photonics Conference, AM1B.6, Hong Kong, China (2015).

[7] T. Nagashima, G. Cincotti, T. Murakawa, S. Shimizu, M. Hasegawa, K. Hattori, M. Okuno, S. Mino, A. Himeno, N. Wada, H. Uenohara, T. Konishi, "Cost Effective Fractional OFDM Receiver using Arrayed Waveguide Grating," Optoelectronics and Communications Conference / International Conference on Photonics in Switching, TuE1-2, Niigata, Japan (2016)